博士論文

Upper Ocean Variability in the North Pacific Subtropical Gyre: Viewpoint of Kuroshio and Water Masses

（北太平洋亜熱帯循環の表層海洋変動 ―黒潮と水塊の観点で－）

川　上　雄　真

令和 4 年

博士論文

Upper Ocean Variability in the North Pacific Subtropical Gyre: Viewpoint of Kuroshio and Water Masses

（北太平洋亜熱帯循環の表層海洋変動 ― 黒潮と水塊の観点で －）

川　上　雄　真

論文審査委員

杉本　周作　　准教授　（主査）
須賀　利雄　　教授
早坂　忠裕　　教授
安中　さやか　教授
木津　昭一　　准教授
境田　太樹　　准教授

令和 4 年

Abstract

Climate changes including global warming are getting much attention from people around the world. Recent disasters such as severe storms, heatwaves, droughts, and wild fires are often attributable to anomalously warm atmospheric and oceanic conditions. Scientists alarm that natural hazards will increase in the future as long as global warming continues. To adapt to the coming climate changes, understandings of the present climate are needed. Insights into daily or weekly variability in the air-sea coupled system are also important to reduce damages from severe events. Since the ocean has substantial influences on the overlying atmosphere on a wide range of timescales from daily to decadal or longer timescales, we need to understand ocean variabilities on various timescales.

In the North Pacific, a large-scale anti-cyclonic circulation called “subtropical gyre” is in the mid-latitude. The subtropical gyre plays an important role for meridional heat and salt distribution, and contributes to the formation of large-scale oceanic fields. In the North Pacific subtropical gyre, a strong jet called “Kuroshio” flows poleward at its western edge and thick surface water masses such as North Pacific subtropical mode water (STMW), North Pacific central mode water (CMW), and North Pacific tropical water (NPTW) are widely distributed. Because the Kuroshio transports large amounts of seawater with heat and the water masses occupy huge volume in the upper ocean, these have been considered as keys to understand the 3-dimensional structure and its variability in the North Pacific subtropical gyre. In this dissertation, I revealed upper ocean variability in the North Pacific subtropical gyre, especially focusing on the Kuroshio and water masses.

Previously, many authors have examined temporal variations of the Kuroshio, STMW, CMW, and NPTW. These deepened our knowledge on upper ocean variability in the North Pacific subtropical gyre. However, it is also true that these studies were limited spatially and temporally due to a lack of observations. For example, a length of time series used in past studies was mostly too short to explore long-term changes and low-frequency fluctuations like decadal variations. In the central North Pacific far from the coast, observational data were especially insufficient. The Japan Meteorological Agency (JMA) has conducted repeat hydrographic observations along 137ºE across the Kuroshio since 1967 and along 165ºE near the central North Pacific since 1996. A number of profiling floats have been deployed over the North Pacific since the Argo project started at 2000. Accumulation of the observational data allows us to explore long-term variability in the whole North Pacific subtropical gyre. Taking advantage of long timeseries from the two repeated hydrographic

sections and basin-wide temperature/salinity (*T*/*S*) profiles from the Argo floats, I explored inter-annual and/or decadal variations of water masses and *T*/*S* structure in the North Pacific subtropical gyre (Chapters 2 and 3) and volume transport of the Kuroshio south of Japan (Chapter 4). Previously, upper ocean variability on timescales longer than inter-annual in the North Pacific subtropical gyre has been considered to be mostly attributable to atmospheric forcing in a cold season. However, this idea has not been evaluated yet. I conducted numerical experiments by using an eddy-resolving ocean general circulation model to reveal this unclear point (Chapter 5). Typhoons that cause serious damage to Japan decrease sea surface temperature (SST) along their wakes, and the decreased SST regions work to weaken subsequent typhoons. However, SST changes during typhoon passages in the Kuroshio region have not been understood yet because the width of the Kuroshio is as narrow as about 100 km and it is difficult to observe it directly under typhoons. I investigated oceanic responses and feedbacks to typhoons in the Kuroshio region by using outputs from atmosphere-ocean coupled model simulations (Chapter 6).

In Chapter 2, I investigated inter-annual variations of CMW formation using *T*/*S* profiles obtained by Argo floats for 2003–2013. I especially focused on a lighter variety of CMW (L-CMW), characterized by potential temperature (θ) of 10–16 ℃ and *S* of 34.2–34.6 and formed in deep winter mixed layer in a zonal band between 140ºE–160ºW centered at around 36ºN. It was found that temporal variations of L-CMW formation are different among the western, central, and eastern part of the formation region. In the central part, L-CMW forms stably in every winter. In the eastern part, L-CMW formation is increased in winter of 2003–2005 and 2010 in association with an intense atmospheric cooling due to an intensification of the Aleutian Low. In the western part, L-CMW formation is enhanced in winter of 2006–2009 and 2011–2013 because of weak ocean surface stratification attributable to anti-cyclonic eddies detached northward from the Kuroshio Extension. I revealed that large parts of L-CMW formed in the eastern formation region subduct into subsurface layers and spread widely over the North Pacific subtropical gyre, whereas L-CMW formed in the western formation region tends to be lost during its advection and hardly detected in subsurface layers.

In Chapter 3, I explored long-term thermohaline changes and variations in the central part of the North Pacific subtropical gyre based on a repeated hydrographic section along 165ºE by the JMA. From the 165ºE sections, I detected significant warming, salinification, and inter-annual thermohaline variations in NPTW and cooling, freshening, and decadal variations in the main thermocline/halocline. The θ and *S* of NPTW originate from mixed layer temperature (MLT) and

salinity (MLS) in the winter isopycnal outcrop region. I revealed that, in the NPTW formation region, MLS determines sea surface density and controls the meridional position of the isopycnal outcrop region, resulting in θ/S changes in NPTW: high MLS and its-associated southward migration of the outcrop region increase θ and S in NPTW, and *vice versa* for low MLS. The θ and S in the main thermocline/halocline are related respectively to MLT and MLS in the winter isopycnal outcrop region, through subduction of both STMW and CMW. It is shown that, in the central North Pacific including the eastern part of the formation region of STMW and CMW, MLT dominantly controls sea surface density and the meridional position of the outcrop region. The MLT-driven meridional migration of the outcrop region causes θ/S changes in STMW and CMW: during high MLT years, the outcrop region migrates northward and then cold-fresh STMW and CMW are formed, and *vice versa* during low MLT years. Such θ-S signals are then passed into the main thermocline/halocline through subduction of STMW and CMW.

In Chapter 4, I focused on net Kuroshio transport south of Japan. Firstly, using JMA repeat hydrographic sections along 137ºE, I produced a net Kuroshio transport timeseries for 1972–2018 which is more than 10 years longer than that used in the previous studies. The net Kuroshio transport has significant two timescales: an inter-annual variation is detectable before 1990 and after 2000, and a decadal variation is clearly observed before 2000. I found that the net Kuroshio transport responds to winter wind stress curl (WSC) in the central part of the North Pacific subtropical gyre through a westward propagation of oceanic Rossby waves with a lag of 2 years. The WSC variations on an inter-annual timescale reflect meridional movements of the Aleutian Low and intensity fluctuations of the North Pacific subtropical high, and those on a decadal timescale result from intensity fluctuations of the Aleutian Low. In addition to inter-annual and decadal variations, I further pointed out a bi-decadal-scale variation of the net Kuroshio transport and its possible link to the Aleutian Low intensity fluctuation. Moreover, influences of net Kuroshio transport on SST and air-sea heat exchanges were examined using atmospheric reanalysis datasets. The result indicated that, during large net Kuroshio transport, SST around the Kuroshio and Kuroshio Extension tends to increase, resulting in vigorous upward sensible and latent heat release.

In Chapter 5, I investigated relative impacts between atmospheric forcing in cold and warm seasons on Kuroshio transport and STMW distribution/temperature in order to understand the responsible season for upper ocean variability in the North Pacific subtropical gyre. I performed three sets of numerical experiments for 1978–2013 with an eddy-resolving ocean general circulation model

(about 10 km resolution) by imposing different atmospheric conditions: (1) CTRL run using 3-hourly atmospheric forcing; (2) COLD run driven by 3-hourly atmospheric forcing in a cold season (October–March) and 3-hourly climatological forcing in a warm season (April–September); and (3) WARM run using 3-hourly forcing in a warm season and climatological forcing in a cold season. These simulations demonstrated that all of net Kuroshio transport and STMW distribution/temperature are mostly controlled by the atmospheric forcing in a cold season, and influences of the warm season atmospheric forcing are not crucial for them.

In Chapter 6, I performed a case study based on three successive typhoons in summer 2018 on SST decreases around the Kuroshio region during passages of typhoons using high-resolution atmosphere-ocean coupled model simulations (about 10 km resolution for both atmosphere and ocean models). Typhoons generally cause SST decrease along their wakes, but I found that the Kuroshio stays warm even after typhoon passages. The Kuroshio's response to typhoons comes from its upper temperature structure: relatively deep mixed layer (~ 50 m) compared with its surrounding region and small vertical temperature gradient around the mixed layer base in the Kuroshio region, which are unfavorable conditions for cooling by vertical mixing, limiting the cooling effect of typhoons. Moreover, I revealed that the high SST sustained in the Kuroshio region results in vigorous upward heat and moisture release to subsequent typhoons.

In the dissertation, focusing on the Kuroshio and water masses, I explored upper ocean variability in the North Pacific subtropical gyre. Based on observational data, I revealed inter-annual and/or longer timescale variations of Kuroshio transport, L-CMW formation, and θ/S in both the main thermocline/halocline and NPTW. I also demonstrated that atmospheric forcing in a cold season is responsible for Kuroshio transport, STMW distribution, and STMW temperature by conducting season-sensitivity experiments using an eddy-resolving ocean general circulation model. In addition, I revealed that SST in the Kuroshio region does not decrease during typhoon passages as SST in its surrounding region does and the high SST sustained over the Kuroshio can influence heat and moisture exchanges between atmosphere and ocean around subsequent typhoons from atmosphere-ocean coupled model simulations. The series of results are meaningful pieces to obtain a complete picture of upper ocean variability in the North Pacific subtropical gyre. In future, impacts of upper ocean variability on the atmosphere should be investigated to improve our knowledges on atmosphere-ocean coupled phenomena and regional- and basin-scale climate variability. This study would be a basis of future works, and can facilitate further understandings of climate variability in the North Pacific.

Acknowledgements

This study was carried out during 2013–2022 in Physical Oceanography Laboratory at Tohoku University, Atmosphere and Ocean Department (formerly known as Global Environment and Marine Department) of the Japan Meteorological Agency, and Department of Atmosphere, Ocean, and Earth System Modeling Research of the Meteorological Research Institute. During this period, I was supported by many people. In this part, I would like to show my gratitude to them.

First of all, I would like to express my deep gratitude to Professor Shusaku Sugimoto at Tohoku University for giving me great guidance and encouragement for 10 years including 8 years after my graduation from a master course of Tohoku University. Without his guidance and supports, I could not continue my research activity and this study would not be accomplished. He constantly told me to take a larger view and to conduct research with objectivity. He also taught me how to make a research presentation on papers and at meetings interesting and easy-to-understand. Everything I have learned from him is a basis of me today as a scientist.

I greatly appreciate Professor Toshio Suga at Tohoku University, who was my supervisor when I was a student in a master course at Tohoku university. He taught me basic theories of physical oceanography as well as the interest, profoundness, and importance of the ocean science. A discussion with him about 10 years ago is the starting point of my research activity. I am also grateful to Dr. Kimio Hanawa, Dr. Shoichi Kizu, and Dr. Futoki Sakaida for giving me great guidance during my time at Tohoku University.

I am deeply grateful to Dr. Goro Yamanaka, Dr. Hideyuki Nakano, Dr. Takahiro Toyoda, Dr. Kei Sakamoto, and Dr. Shogo Urakawa at the Meteorological Research Institute. They taught me how to use an ocean model and gave me technical supports to analyze results from model simulations. Their supports and encouragement on writing this dissertation are also appreciated. Dr. Norihisa Usui gave me advice on studies of the Kuroshio. Dr. Yosuke Fujii and Mr. Nariaki Hirose kindly supported me in various ways since I moved to the Meteorological Research Institute. Thanks are extended to Dr. Toshiya Nakano, Dr. Yoshiteru Kitamura, and Mr. Atsushi Kojima. I learned from them a lot during my time at the Japan Meteorological Agency.

Up to today, I have had many opportunities to participate in research meetings and cruises, and to communicate with researchers outside of my laboratories. I appreciate Dr. Eitarou Oka at the University of Tokyo, Dr. Masanori Konda at Kyoto University, Dr. Fumiaki Kobashi at Tokyo

University of Marine Science and Technology, Dr. Shigeki Hosoda and Dr. Shinya Kouketsu at Japan Agency for Marine-Earth Science and Technology, Dr. Sayaka Yasunaka at Tohoku University, Dr. Shota Katsura at Scripps Institution of Oceanography, and Dr. Shun Ohishi at RIKEN for lively discussions.

In this study, I used a wide variety of observational data. I also used atmosphere and ocean models developed in the Japan Meteorological Agency/Meteorological Research Institute. I would like to show my gratitude to past and present scientists and technical staffs in the field of ocean observation, data management, and model development. I was supported by the Japan Society for the Promotion of Science (grant 21K20384) for studies on the Kuroshio (Chapters 4, 5, and 6).

Finally, I would like to express the deepest gratitude to my family and friends for their warm supports.

Yuma Kawakami

Contents

Chapter 1
General introduction

1.1 Background

1.1.1 Physical features in the North Pacific subtropical gyre

In the world's oceans, there are five large-scale anti-cyclonic circulations, and those are in low- to mid-latitudes in each ocean basin and called "subtropical gyre": the North Atlantic subtropical gyre, the South Atlantic subtropical gyre, the North Pacific subtropical gyre, the South Pacific subtropical gyre, and the Indian Ocean subtropical gyre. These subtropical gyres are generated by cyclonic wind stress curl between westerlies and trade winds. Subtropical gyres play an important role for meridional distribution of heat, salt, and substances between low- and mid-latitude regions, and largely contribute to formation and maintenance of large-scale oceanic fields. In the subtropical gyres, a poleward jet called "western boundary current" flows in their western edge and water masses characterized as a thick layer (~300 m) over the main thermocline/halocline with specific properties and vertical homogeneity are widely distributed. Because the western boundary currents transport large amounts of seawater and water masses occupy huge volume in the subsurface, these are considered to be keys to understand 3-dimensional temperature/salinity (*T*/*S*) distributions in the subtropical gyres.

The Kuroshio is the western boundary current in the North Pacific subtropical gyre (Figure 1.1). With an origin in tropics east of Philippine near 12ºN, it flows northward along the island of Luzon, the island of Taiwan, and the steep continental slope in the East China Sea with an increase of its volume transport from about 15 Sv (1 Sv = 10^6 m^3 s^{-1}) to 25 Sv (e.g., Andres et al., 2008). Through the Tokara strait south of Kyushu, the Kuroshio enters the North Pacific from the East China Sea, and strengthens to about 40 Sv (Imawaki et al., 2001). After flowing northeastward along the south coast of Japan from 130ºE to 140ºE, the Kuroshio separates from the coast of Japan and becomes an eastward jet called Kuroshio Extension (KE). Since the Kuroshio transports large amounts of heat, it has substantial influences on sea surface temperature (SST) in the western boundary region (e.g., Qiu, 2000; Wu et al., 2012), resulting in vigorous release of latent and sensible heat from the sea surface. Many authors have demonstrated strong air-sea coupling in the Kuroshio and KE regions on various timescales from daily to decadal or longer timescales (e.g., Nonaka and Xie, 2003; Tanimoto et al., 2011: Nakamura et al., 2012; Kuwano-Yoshida and Minobe, 2017; Sugimoto et al., 2017a, 2020, 2021).

North Pacific subtropical mode water (STMW; Masuzawa, 1969) is a huge water mass located over the northwestern corner of the North Pacific subtropical gyre (red shaded area in Figure 1.1), characterized by vertically uniform property with T of 15–19 ℃ and S of 34.7–34.9. The STMW is formed in the deep winter mixed layer developed in a region south of the KE (Hanawa and Talley, 2001; Oka and Qiu, 2012). The deep winter mixed layer is caused by intense sea surface cooling due to a cold outbreak from the continent (e.g., Suga and Hanawa, 1990). Because STMW is formed by the atmospheric forcing, its properties, e.g., temperature and thickness, reflect winter atmospheric conditions such as air temperature and wind speed: the stronger the winter atmospheric forcing is, the colder and thicker STMW forms (e.g., Suga and Hanawa, 1995a; Yasuda and Hanawa, 1999). As radiative heating becomes strong in spring, STMW is capped by a seasonal thermocline and advected southwestward by the anti-cyclonic circulation of the North Pacific subtropical gyre (e.g., Bingham, 1992; Suga and Hanawa, 1995b). North Pacific central mode water (CMW) is characterized by a pycnostad (i.e., vertical homogeneity) with T of 8.5–16 ℃ and S of 33.9–34.6 in the western part of the North Pacific subtropical gyre (Nakamura, 1996; Suga et al., 1997). Its formation and distribution processes are similar to those of STMW: CMW is formed in the deep winter mixed layer north of the KE, and spreads into subsurface layers along the anti-cyclonic circulation of the North Pacific subtropical gyre (e.g., Oka et al., 2011). CMW is classified into two types by the Kuroshio bifurcation front (KBF) north of the KE (e.g., Mecking and Warner, 2001; Tsujino and Yasuda, 2004; Oka and Suga, 2005): the lighter variety of CMW (L-CMW; T of 10–16 ℃ and S of 34.2–34.6) formed in the south of the KBF and the denser variety (D-CMW; T of 8.5–10.0 ℃ and S of 33.9–34.2) formed in the north of the KBF (light and dark blue shaded areas in Figure 1.1). STMW and CMW, which supply large amounts of seawater into the ocean interior, play an important role in determining upper ocean stratification, maintenance of the main thermocline/halocline (Toyama and Suga, 2012), and generation of eastward counter currents accompanied by subtropical fronts (Kobashi et al., 2006). Since both STMW and CMW are isolated from the atmosphere after their subduction in spring, their properties are preserved in the ocean interior. Both STMW and CMW are regarded as an indicator of large-scale climate. North Pacific tropical water (NPTW; Cannon, 1966) is characterized by salinity maximum layer. NPTW is originated from surface mixed layer in the central part of the North Pacific subtropical gyre with high sea surface salinity (Cannon, 1966) where evaporation exceeds precipitation, and then is distributed in the North Pacific subtropical gyre (yellow shaded area in Figure 1.1). Since salinity and area size of NPTW reflect evaporation and precipitation in the subtropical

North Pacific, those are often used as an indicator of the large-scale fresh water circulation (e.g., Suga et al., 2000; Nakano et al., 2015). Near the east coast of Philippine around 12ºN, NPTW separates into two parts. One is transported northward by the Kuroshio and affects salinity distributions in the mid-latitude western North Pacific. The other veers southward with the Mindanao Current. NPTW in the southern branch influences SST in the western tropical Pacific through formation of barrier layer (Lukas and Lindstrom, 1991).

1.1.2 Upper ocean variability in the North Pacific subtropical gyre

Recently, concerns for climate changes including global warming have been growing. Understandings of the climate system and insights into the coming climate changes have been increasingly important. Since the ocean is an essential element of the climate system, it is important to monitor and investigate ocean variability to improve our knowledge on climate variability, predict the future climate reliably, and adapt to the coming climate changes successfully. In the North Pacific subtropical gyre, many authors have revealed upper ocean variability focusing on the Kuroshio (e.g., Qiu and Joyce, 1992; Sugimoto et al., 2010), STMW (e.g., Qiu and Chen, 2006; Sugimoto et al., 2017b; Oka et al., 2019), CMW (Kouketsu et al., 2012; Oka et al., 2012), and NPTW (Suga et al., 2000; Nakano et al., 2015) using observational data in the western North Pacific near Japan. However, there are some points not treated or not fully discussed in the past studies. For example, temporal variations of CMW and NPTW formation have not been fully understood yet because of a lack of observational data far from the coast, i.e., in the central North Pacific where CMW and NPTW are formed. Significant freshening since 1996 and decadal thermohaline variations were observed in the main thermocline/halocline at the western edge of the North Pacific subtropical gyre (Oka et al., 2017), but their mechanisms have not been demonstrated yet and it has been unclear whether or not the freshening and decadal variation in the main thermocline/halocline occur on a basin scale. Additional investigation is needed to obtain comprehensive understandings on variability of water masses and *T*/*S* structure in the North Pacific subtropical gyre.

Temporal variations of Kuroshio transport should also be investigated. It is known that the Kuroshio transport responds to winter wind stress fields over the North Pacific and has various timescales of inter-annual to bi-decadal timescales (e.g., Qiu and Joyce, 1992; Sugimoto et al., 2010). Past works pointed out that the Aleutian Low (AL) in the northern North Pacific has significant impacts on the Kuroshio transport (e.g., Sugimoto and Hanawa, 2009). The North Pacific subtropical

high (NPSH) is distributed in the eastern North Pacific throughout a year at the latitude of which is consistent with the Kuroshio region. The NPSH would play an important role in determining wind stress fields over the North Pacific. However, influences of NPSH variations on the Kuroshio have not been discussed. Revisit of the Kuroshio transport variations with focuses on relationships to the AL and NPSH would give us further understandings on variability of the Kuroshio and the large-scale circulation in the North Pacific subtropical gyre.

Upper ocean variability in the North Pacific subtropical gyre on inter-annual or longer timescale has been attributed to atmospheric forcing in a cold season because sea surface winds in the North Pacific are stronger in a cold season than a warm season (Sandwell and Agreen, 1984). Past works have investigated variability in Kuroshio transport and STMW distribution/temperature with a relationship to winter atmospheric conditions (e.g., Suga and Hanawa, 1995a; Sugimoto et al., 2010). However, there is little discussion on whether or not atmospheric forcing in the other seasons is also important. To obtain a perspective on large-scale upper ocean variability and its relation to atmospheric variations, we need to carefully evaluate the impacts of atmospheric forcing in each season.

In the light of disaster prevention, upper ocean variability on a shorter timescale like daily-to-weekly timescale is important (e.g., Mogensen et al., 2017). Typhoons in the western North Pacific cause heavy rainfall and windstorms in Japan and east Asia. Typhoons largely decrease SST along their wakes (e.g., Sakaida et al., 1998; Zhang et al., 2010) and the decreased SST region called cold wakes works to weaken the subsequent typhoons (e.g., Park et al., 2019). However, it has not been clarified whether or not SST in the Kuroshio region characterized by relatively high SST and large ocean heat content compared with its surrounding region is also decreased by typhoons because the width of the Kuroshio is as narrow as about 100 km and it is difficult to observe SST in the Kuroshio region directly under typhoons. Understandings of ocean-typhoon interactions in the Kuroshio region would contribute to an improvement of typhoon forecast and then disaster prevention in Japan and east Asia.

1.2 Scope of this dissertation

Based on the above background, we conduct five studies on upper ocean variability in the North Pacific subtropical gyre. In Chapter 2, we reveal temporal variations of CMW formation using *T*/*S* profiles taken by Argo floats for 2003–2013. We especially focus on its lighter variety (L-CMW). Firstly, *T*/*S* properties of L-CMW are defined from a frequency distribution of the deep winter mixed

layer on a *T*/*S* diagram. In the L-CMW formation region where the deep winter mixed layer forms, we investigate temporal variability of L-CMW formation and its cause. Influences of L-CMW formation variations on summertime subsurface ocean in the North Pacific subtropical gyre are also explored.

In Chapter 3, we investigate changes and variations of thermohaline in the North Pacific subtropical gyre using repeated hydrographic sections along 165ºE near the central part of the North Pacific, which have been maintained by the Japan Meteorological Agency (JMA) since 1996. We focus on *T*/*S* trends and inter-annual to decadal variations in the salinity maximum layer (i.e., NPTW) and the main thermocline/halocline. Combining the 165ºE sections with optimally interpolated grid *T*/*S* dataset based on Argo floats, we further reveal the mechanism generating the *T*/*S* changes and variations in the upper ocean.

In Chapter 4, we originally estimate net Kuroshio transport for 1972–2018 based on JMA hydrographic sections along 137ºE. We reveal predominant timescales of net Kuroshio transport and their relationships to large-scale atmospheric circulation in the North Pacific in terms of the AL and NPSH. We discuss impacts of the net Kuroshio transport variation on SST and air-sea heat exchanges in the Kuroshio and KE regions.

In Chapter 5, we investigate an influence of atmospheric forcing in cold and warm seasons on Kuroshio transport and STMW distribution/temperature, by performing numerical experiments for 1978–2013 with an eddy-resolving ocean general circulation model for the North Pacific. We attempt to understand which season has dominant impacts on inter-annual or longer timescale variability of Kuroshio transport and STMW distribution/temperature.

In Chapter 6, we analyze outputs of atmosphere-ocean coupled model simulations and recently-developed ultra-high resolution satellite-derived SST product to investigate SST responses to typhoons in the western North Pacific including the Kuroshio region. A mixed layer heat budget analysis is performed to quantitatively assess a cause of the SST response in the Kuroshio region during typhoon passages. We discuss impacts of the SST changes in the Kuroshio region on subsequent typhoons.

In Chapter 7, we summarize the main results of this dissertation. We describe remaining issues to be addressed in future works for further understandings of the upper ocean variability in the North Pacific subtropical gyre.

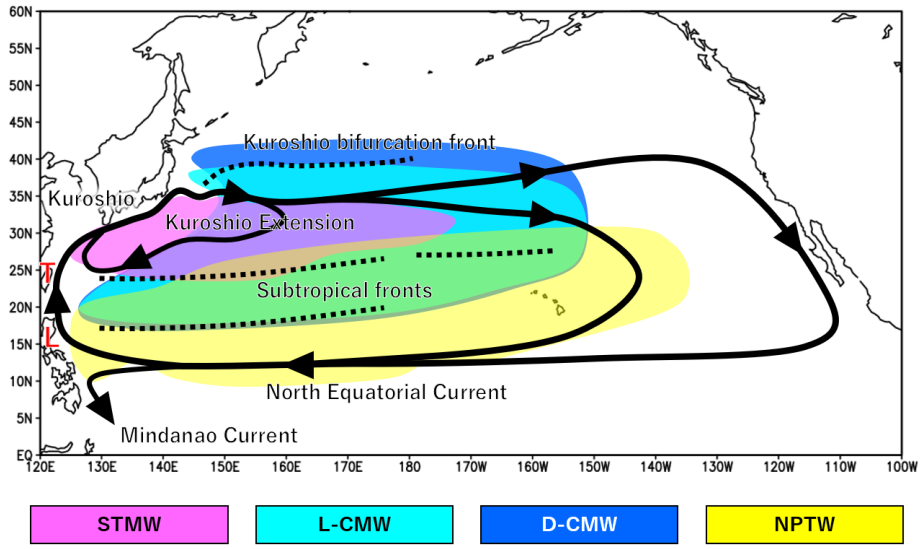

Figure 1.1

Schematic illustration of the North Pacific subtropical gyre. Black lines denote the large-scale ocean circulation in the North Pacific. Regions with red, light blue, dark blue, and yellow shading indicate the distribution area of STMW, L-CMW, D-CMW, and NPTW, respectively. Dashed lines represent the Kuroshio bifurcation front and subtropical fronts. L and T written in red mean the island of Luzon and the island of Taiwan, respectively.

Chapter 2

Inter-annual zonal shift of the formation region of the lighter variety of the North Pacific central mode water (L-CMW)

2.1 Introduction

The North Pacific central mode water (CMW), which is formed in the wintertime deep mixed layer (ML) near the northern boundary of the subtropical gyre, is characterized by a pycnostad in the lower ventilated pycnocline in the central part of the North Pacific subtropical gyre. In two separate investigations based on different climatological data, the CMW was identified as a thermostad with core temperature of 8.5°C–11.5°C by Nakamura (1997) and of 10°C–13°C by Suga et al. (1997). Numerous studies have investigated climatological features of the CMW formation in the deep winter ML to the north of the Kuroshio Extension (KE) and its circulation along the subtropical gyre (e.g., Ladd and Thompson, 2000; Ohno et al., 2004; Suga et al., 2004). Suga et al. (2004) showed the distribution of CMW and figured its possible formation area based on isopycnally-averaged climatology; they found that the CMW is centered to the east of the International Dateline at 35–40°N and extends southwestward in the subtropical gyre on isopycnal layers of 26.0–26.5 kg m^{-3}. The CMW, which supplies large amounts of water to the ocean interior (Suga et al., 2008), plays an important role in generating surface layer stratification and unique currents accompanied by subtropical fronts (Aoki et al., 2002; Kobashi et al., 2006). Sugimoto et al. (2012) revealed that the intensity of the North Pacific eastern subtropical front is associated with the CMW formation, based on ocean general circulation model outputs. The CMW is also important for biogeochemical transport in the subsurface ocean; for example, the CMW is presumably a significant transporter of CO_2 into the ocean interior in its formation region, as the region corresponds to a prominent CO_2-absorbing region (Takahashi et al., 2009).

Oka and Suga (2005) revealed more details of the structure of the CMW formation region based on an analysis of repeat hydrographic section data along 165°E. They reported that the CMW formation is closely related to thermohaline fronts in the western North Pacific, namely the Kuroshio Extension Front (KEF), the Kuroshio Bifurcation Front (KBF), and the Subarctic Front (SAF). They also showed that the lighter variety of CMW (L-CMW; potential density (σ_θ) = 25.8–26.2 kg m^{-3}) is formed between the KEF and the KBF, and that the denser variety (D-CMW; σ_θ = 26.3–26.4 kg m^{-3}) is formed between the KBF and the SAF, as suggested by synoptic observations (Mecking and Warner,

2001) and an eddy-resolving ocean general circulation model (Tsujino and Yasuda, 2004). In an analysis of Argo profiling data for 2003–2008, Oka et al. (2011) defined the L-CMW (D-CMW) property as a potential temperature (θ)–salinity (S) mode at approximately 13°C–34.4 (9°C–34.0) based on deep winter ML properties, and detected the L-CMW (D-CMW) formation region in terms of winter ML properties. The L-CMW (D-CMW) is formed in a zonal band of 33–39°N (39–42°N), just to the north of the KEF (KBF) and from the east coast of Japan to a region east of the International Dateline. After spring, both the L-CMW and D-CMW subduct to the subsurface layer and circulate in the subtropical gyre.

Past studies have reported low-frequency variations of the CMW distribution area, associated with a regime shift that occurred in 1975/1976 (Yasuda and Hanawa, 1997) and decadal-scale (about 10 years) changes in the path state of the KE (Oka et al., 2012). However, high-frequency (e.g., year-to-year) variations of CMW formation have not been yet clarified because of a shortage of observational data. At present, relatively high-resolution data are available over the North Pacific for a period of over 10 years owing to the sustained deployment of Argo floats. In this study, we investigate the temporal and spatial variability of the L-CMW formation and explore its cause using Argo profile data for 2003–2013.

2.2 Data and method

We use near-real-time temperature–salinity data from Argo profiling floats for 2003–2013 that passed the quality control criteria outlined by Oka et al. (2007). These criteria specified the removal of profiles with fewer than 20 sampling depths, as well as defective profiles, such as those with the shallowest depth deeper than 10 dbar, those lacking intermediate layers, and those with bad temperature, salinity, or pressure values. We vertically interpolated each profile at 1-dbar intervals using an Akima spline (Akima, 1970). Then θ and σ_θ are calculated. The MLD was defined as the depth at which σ_θ increases by 0.03 kg m^{-3} above the value at the 10-dbar depth (Weller and Plueddemann, 1996). We regard the ML with the depth > 150 dbar as deep ML, following to Oka et al. (2011) and Kouketsu et al. (2012). The ML property (θ–S) is represented by the value at a depth of 10 dbar. We specifically focus on winter of February–April when the MLD around the CMW formation region is deepest (Oka et al., 2007). Figure 2.1 displays the number of Argo float profiles around the L-CMW formation region (33–39°N, 140°E–160°W; reviewed in Oka and Qiu, 2012) in winter, revealing the availability of over 100 profiles in the region since 2003.

We also use satellite-derived sea surface height (SSH) dataset from the Archiving, Validation, and Interpretation of Satellite Oceanographic data (AVISO; www.aviso.oceanobs.com), with a temporal resolution of 7 days and a spatial resolution of 0.25° (longitude) × 0.25° (latitude). We use monthly surface net heat flux (NHF; sum of the latent heat flux, sensible heat flux, net surface longwave radiation, and net surface shortwave radiation) and wind stress data from the Japanese 25-year Reanalysis/Japan Meteorological Agency Climate Data Assimilation System (JRA-25/JCDAS) (Onogi et al., 2007) on a horizontal resolution of 2.5° (longitude) × 2.5° (latitude). We use the satellite-derived sea surface temperature (SST) products based on the Advanced Very High Resolution Radiometer (AVHRR) infrared satellite data (Reynolds et al., 2007) with a spatial resolution of 0.25° (longitude) × 0.25° (latitude).

2.3 Climatological L-CMW property and formation region

Figure 2.2 displays the distribution of deep ML in winter. Three regions with deep ML are detected, as in previous studies (e.g., Suga et al., 2004): the western to central part of the mid-latitude North Pacific, the Bering Sea, and the eastern part of the mid-latitude North Pacific. Among these locations, the CMW is formed in the western to central part of the mid-latitude North Pacific (Suga et al., 2004; Oka and Suga, 2005; Oka et al., 2011).

We investigate the properties of the deep winter ML. Several clusters clearly emerge on a θ–S diagram (Figure 2.3a). To detect each cluster, we counted the number of θ–S values in each 0.05 × 0.5°C grid box (Figure 2.3b). Four clusters are identified, with θ–S modes [θ, S] at approximately [18°C, 34.8], [13°C, 34.4], [9°C, 34.0], and [7°C, 33.8]. Among them, the mode centered at [13°C, 34.4] represents the L-CMW property. In this study, we define the L-CMW property as θ = 10–16°C and S = 34.2–34.6 by encompassing the grid boxes with profiles greater than 10 around [13°C, 34.4].

2.4 Variation of the L-CMW formation region

We investigate temporal variations of the L-CMW formation region, as represented by the deep winter ML with the L-CMW properties. The L-CMW formation region shows a marked zonal shift interannually (Figure 2.4): an eastward location in 2003–2005 and 2010, and a westward location in 2006–2009 and 2011–2013. An examination of the deep winter ML distributions during these two periods confirms that during the former period (2003–2005 and 2010) the deep ML tends to be in the eastern region (Figure 2.5a), while during the latter period (2006–2009 and 2011–2013) the deep ML

tends to be in the western region (Figure 2.5b). In addition, we examine the deep winter ML distribution and its temporal behavior. Figure 2.6 displays the longitudinal distribution of the MLD with L-CMW property during the two periods, and Figure 2.7 shows a time series of the frequency of the deep winter ML with the L-CMW property. It is apparent that the ML is deeper in the eastern part (180°–160°W) during 2003–2005 and 2010 (Figures 2.6a and 2.7a), and deeper in the western part (140–155°E) during 2006–2009 and 2011–2013 (Figures 2.6b and 2.7c). The deep ML is distributed in the central region (155°E–180°) between the western and eastern parts throughout the analysis period (Figures 2.6 and 2.7b).

In the following analyses, we focus specifically on the eastern period (2003–2005 and 2010) and the western period (2006–2009 and 2011–2013) of the L-CMW formation region, and explore the temporal behavior of winter MLD in eastern (30–40°N, 180°–160°W) and western (36–40°N, 140–155°E) parts of the L-CMW formation region.

2.4.1 Winter mixed layer depth variations in the eastern L-CMW formation region

We investigate temporal variation of the MLD in the eastern part of the L-CMW formation region. Past studies have reported that in the recirculation regions south of the KE, winter cooling attributable to atmospheric forcing is a dominant factor in the deepening of the MLD on inter-annual timescales.

To examine the influence of wintertime atmospheric forcing on the MLD, we investigate sea surface wind stress in winter (January–March; note one month prior to ocean winter, as the time of peak cooling of the ocean surface due to atmospheric forcing precedes the winter months of the ocean field by one month). During the eastern period (Figure 2.8a), the strong westerlies prevail across the North Pacific, while, during the western period (Figure 2.8b) the westerlies turn to the north in the central North Pacific. As a result, a marked difference between the eastern and western periods is found over the eastern part of the L-CMW formation region (Figure 2.8c), presumably reflecting changes in the strength of the Aleutian Low, which is located in the central North Pacific.

It is expected that the difference in wind stress influences oceanic surface cooling over the formation region. We thus explore oceanic heat loss, which is the sum of the NHF and Ekman heat advection, in winter (January–March). Here, the Ekman heat advection (Q_e) is calculated as,

$$Q_e = -\rho_w C \boldsymbol{u_e} \cdot \boldsymbol{\nabla} T \qquad (2.1)$$

where ρ_w is the density of sea water, C is the specific heat of sea water, T is the SST, and $\boldsymbol{u_e}$ is Ekman

transport, which is related to the surface wind stress vector $\boldsymbol{\tau}$ by $\boldsymbol{u_e} = -\mathbf{k} \times \boldsymbol{\tau}/(\rho_w f)$, where f is the Coriolis parameter.

In the eastern part, the NHF (189 W m^{-2}) is, on average, much larger than the Ekman heat advection (27 W m^{-2}) during the 2003–2013 period. However, anomalies in the NHF are comparable to those of the Ekman heat advection (Figure 2.9), and they covary with one another. Thus, the NHF and Ekman heat advection have an equivalent impact on oceanic heat loss. Figure 2.7a displays the time series of wintertime oceanic heat loss in the eastern part of the L-CMW formation region. The oceanic heat loss undergoes inter-annual variations and its temporal behavior is very similar to the occurrence of the deep winter ML in this area (black bar in Figure 2.7a).

We then examine the spatial characteristics of oceanic heat loss, which is remarkably large in the eastern part of the L-CMW formation region. The results show that the oceanic heat loss associated with changes in the strength of westerlies is responsible for variations in the winter MLD in the eastern part of the L-CMW formation region.

2.4.2 Winter mixed layer depth variations in the western L-CMW formation region

We explore the causes of variations of the winter MLD in the western part of the L-CMW formation region. In contrast to the eastern part, the variations in oceanic heat loss in the western part are relatively small (Figure 2.8c).

The KE is located to the south of the western part of the L-CMW formation region. Recent studies have indicated two dominant states of the KE path as represented by eddy activity (Qiu and Chen, 2005, 2010): a stable path state with low eddy activity and an unstable path state with high eddy activity. Figure 2.10, which shows the yearly paths of the KE axis at 2-week intervals, reveals that the KE path is in the stable state in 2003–2005 and 2010–2011, and in the unstable state in 2006–2009 and 2012–2013. Recent studies have pointed out that the KE in the unstable path state tends to pinch off anti-cyclonic meso-scale eddies to the north (Kouketsu et al., 2012; Oka et al., 2012). Since surface stratification is weak in anti-cyclonic eddies, winter ML is likely to become deeper when the KE is in an unstable path. In fact, it is confirmed that a few anti-cyclonic eddies are distributed in the western part of the L-CMW formation region, and the MLD in those eddies is deep during the unstable KE path state of March 2009 (Figure 2.11a). On the other hand, in 2010, in the stable KE path state (Figure 2.11b), fewer anti-cyclonic eddies are present, and a deepening of the MLD is not detected.

We explore temporal variations in the KE path state, the anti-cyclonic meso-scale eddies

distribution, and the MLD in the western part of the L-CMW formation region during 2003–2013, using satellite-derived SSH and Argo float data, to investigate the relationships among these variables. We investigate the SSH as an indicator of KE path variability, as high SSH in the western part of the L-CMW formation region would be produced by anti-cyclonic eddies. Figure 2.7c displays a time series of SSH averaged over the western part of the L-CMW formation region (red line). The SSH in this region is higher during the unstable state of the KE (2006–2009 and 2012–2013) than during the stable state, reflecting the presence of anti-cyclonic eddies, and its temporal behavior is very similar to the occurrence of the deep MLD with the L-CMW property (black bar in Figure 2.7c). Deep MLs are formed in the western part of the formation region when the KE path is in an unstable state and weakly stratified anti-cyclonic eddies are present in the region. Therefore, we conclude that weakened surface stratification associated with the presence of anti-cyclonic eddies is responsible for the formation of the deep winter ML in the western part of the L-CMW formation region.

2.5 Summertime L-CMW distribution in the subsurface layer

Does the inter-annual zonal shift of the L-CMW formation region have any large-scale consequences? We examine whether or not the L-CMW formed in the eastern part is different from that in the western part in terms of its distribution in the ocean subsurface layer. We explore potential vorticity (PV), as the L-CMW is detected as low-PV (vertically homogeneous) water. Here, the PV is calculated as,

$$\mathrm{PV} = -\frac{f}{\rho}\frac{\partial \sigma_\theta}{\partial z} \tag{2.2}$$

where ρ is the density of seawater and z is a vertical coordinate. The relative vorticity is ignored because the L-CMW distribution region is far from any strong currents, near which the relative vorticity is comparable to the planetary vorticity.

Figure 2.12 displays the frequency of occurrence of profiles with low PV in summer (June–October) on the isopycnal surface σ_θ = 25.8 kg m^{-3}, which corresponds to the core density of the L-CMW. Interestingly, the L-CMW distribution in the subsurface layer is different between the two periods: the L-CMW formed in the eastern period tends to be widely distributed over the North Pacific subtropical gyre, while the L-CMW formed in the western period is hardly detected in the subsurface layer. This finding is possibly the result of the L-CMW formed in the eastern part being transported southward and effectively subducted into the ocean interior by crossing the MLD front, which results in the wide distribution of the L-CMW over the North Pacific subtropical gyre. In contrast, the L-

CMW formed in the western part is dissipated or entrained into the deep ML during the subsequent winter, during its eastward movement. Toyama et al. (2015) have recently reported that the annual subduction rate in the density range of the L-CMW shows consistent and marked inter-annual variations, which is reflected in winter MLD variations in the eastern part of the L-CMW formation region. These findings indicate that the L-CMW in the subtropical gyre in the eastern part of the formation region is mainly subducted, and implies that the L-CMW formed in this region is responsible for ventilation of the isopycnals at approximately σ_θ = 25.7–26.1 kg m^{-3}.

2.6 Summary and discussions

By using Argo profile data for 2003–2013, we investigated the L-CMW formation variability, focusing on the deep (> 150 dbar) winter ML with the L-CMW property (θ = 10°C–16°C, S = 34.2–34.6). The L-CMW formation region showed marked zonal shift interannually: the deep MLD in the eastern part of the L-CMW formation region (east of the International Dateline) in 2003–2005 and 2010 (eastern period), and the deeper in the western part (west of 155°E) in 2006–2009 and 2011–2013 (western period).

In the eastern part of the L-CMW formation region, the deep winter ML results from the large oceanic heat loss (sum of the NHF and Ekman heat advection), attributable to the strong westerlies associated with strengthening of the Aleutian Low. Subsequently, the L-CMW is subducted into the subsurface layer, which results in its wide distribution over the North Pacific subtropical gyre. In contrast, in the western part of the L-CMW formation region, the deep winter ML is caused by weak surface ocean stratification due to the anti-cyclonic meso-scale eddies pinched off northward from the KE in the unstable state of the KE path. The L-CMW formed in the western part is hardly detected in the subsurface layer during the following summer, possibly because the L-CMW property is lost through dissipation and/or entrainment process to the ML during the following winter, during eastward movement. That is, the L-CMW formed in the eastern part of the formation region is responsible for ventilation on isopycnals around σ_θ = 25.7–26.1 kg m^{-3}.

Our results show that MLD variation in the eastern part of the L-CMW formation region is in a phase opposite to that in the western part, despite the fact that the cause is quite different in the two parts; the process connecting the two parts might be oceanic Rossby waves. A recent study by Oka et al. (2012) denoted the oceanic Rossby waves formed as a result of strong westerlies propagate westward and reach the KE region after a delay of several years, leading to the unstable state of the

KE path. In this way, the MLD variations in the eastern part seem to be correlated with those in the western part, with a delay of several years, as is apparent in Figures 2.7a and 2.7c. The time lag is approximately consistent with the propagation period of oceanic Rossby waves from the eastern part to the western part of the L-CMW formation region. Therefore, it is expected that MLD variations in the western part of the L-CMW formation region are linked to those in the eastern part through oceanic Rossby waves caused by the strong westerlies. To gain a further understanding of the relationship between the MLD variations in the two KE paths (stable and unstable), long-term observational data are needed.

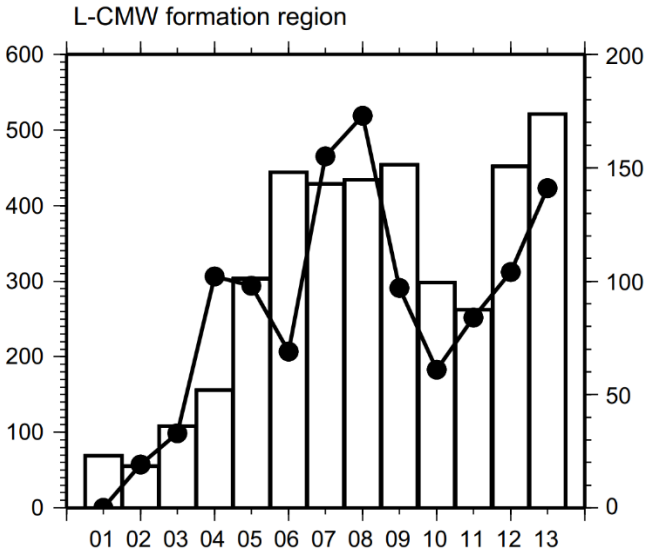

Figure 2.1

Number of profiles around the L-CMW formation region (34–39°N, 140°E–160°W) in winter (February–April) of 2001–2013 (white bar, left axis). Black line indicates the number of profiles in the eastern part of the L-CMW formation (east of 170°E, right axis).

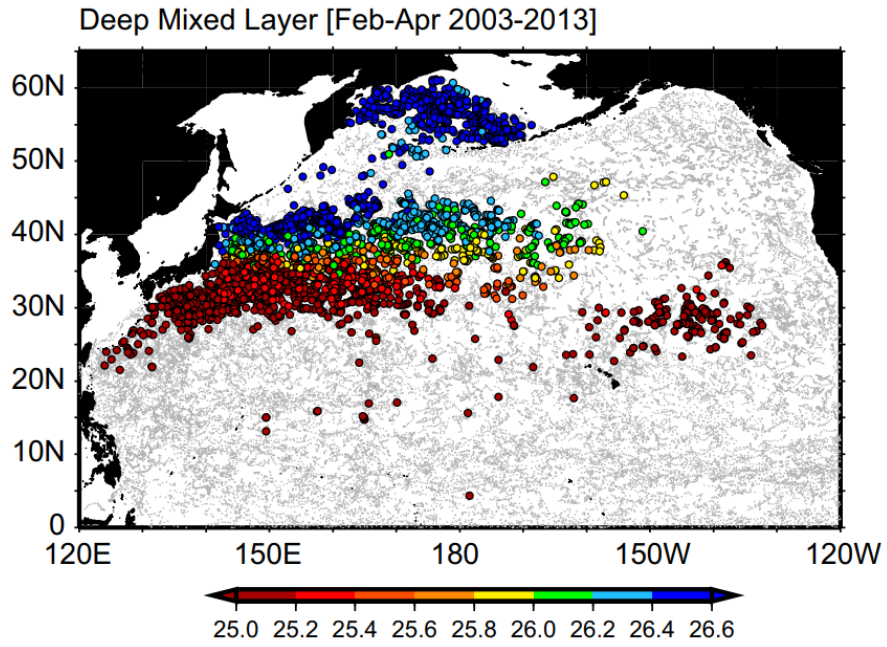

Figure 2.2

Distribution of potential density [kg m^{-3}] of deep ML (> 150 dbar) in winter (February–April) of 2003–2013 (color dots). Gray dots indicate ML depths of < 150 dbar.

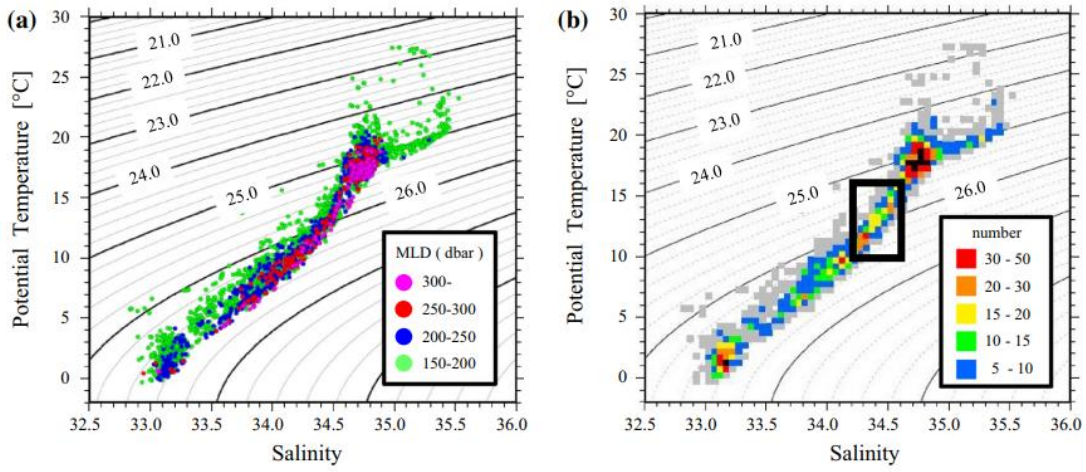

Figure 2.3

(a) Potential temperature–salinity diagram of the deep ML in winter (February–April) of 2003–2013 in the North Pacific. Symbol color indicates the MLD. Contours denote potential density [kg m^{-3}]. (b) The number of deep ML values in each 0.05 (salinity) × 0.5°C (potential temperature) bin. Thick rectangle indicates the range of L-CMW property determined in this study.

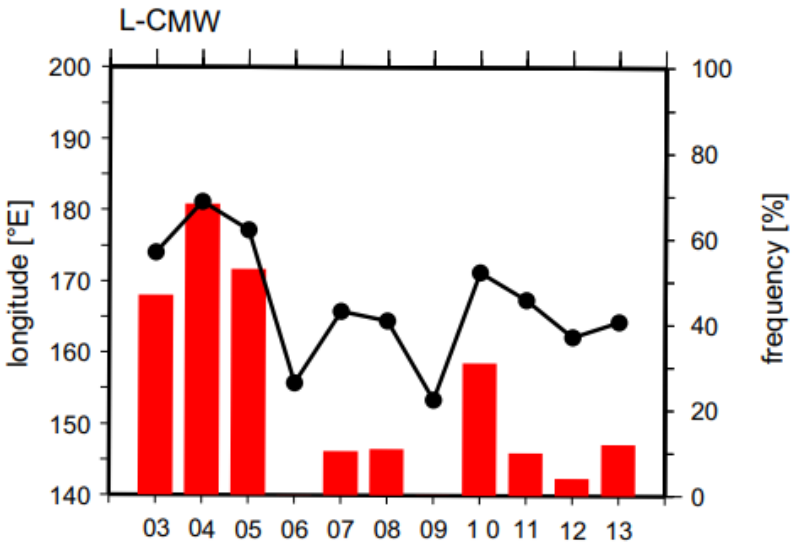

Figure 2.4

Time series of the longitudinal position averaged for profiles in the deep winter (February–April) ML with the L-CMW property (solid line, left axis). Red bars indicate the ratio of the number of profiles of deep winter MLs with L-CMW property east of the International Dateline to all profiles of deep winter MLs with L-CMW property (right axis).

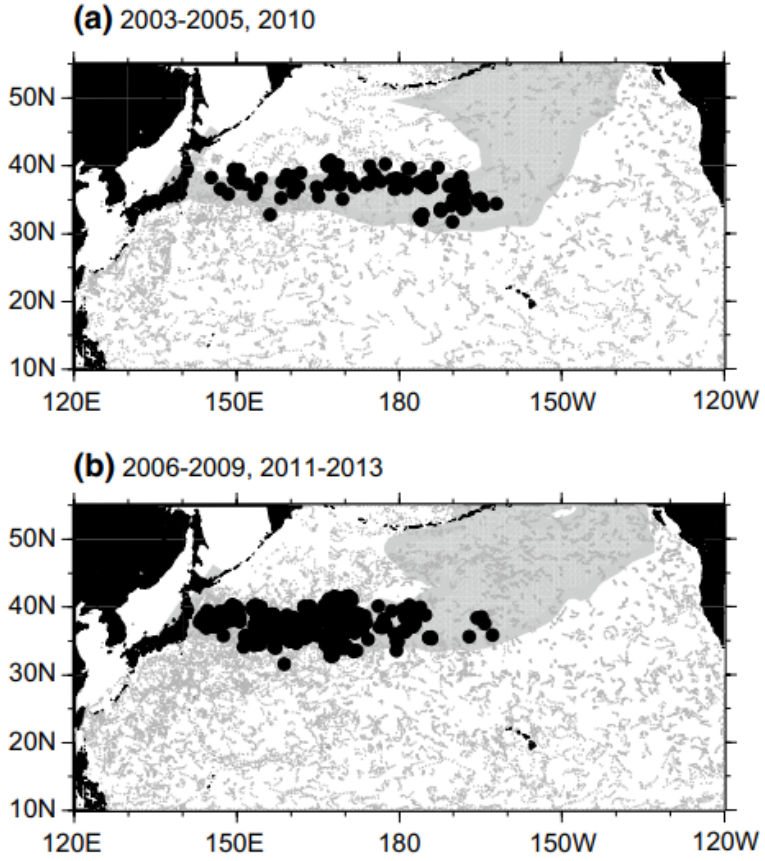

Figure 2.5

Distribution of the deep ML with the L-CMW property in winter (February–April) of (a) 2003–2005 and 2010, and (b) 2006–2009 and 2011–2013 (black dots). Grey dots indicate observation points where no deep ML with the L-CMW property was present. Gray shading denotes the outcrop zone of σ_θ = 25.5–26.1 kg m^{-3}, averaged in March based on the monthly gridded temperature–salinity (θ–S) data set (Grid Point Value of the Monthly Objective Analysis using the Argo data: MOAA-GPV) produced by Hosoda et al. (2008).

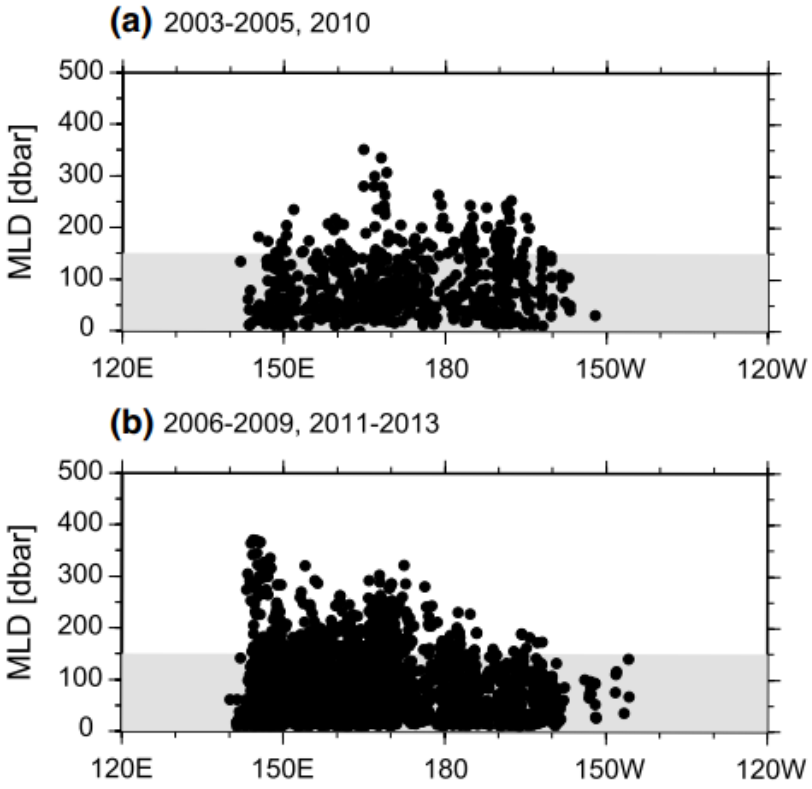

Figure 2.6

Longitudinal distribution of profiles with a MLD that includes the L-CMW property in winter (February–April) of (a) 2003–2005 and 2010, (b) 2006–2009 and 2011–2013 (black dots). Grey shading indicates MLD < 150 dbar.

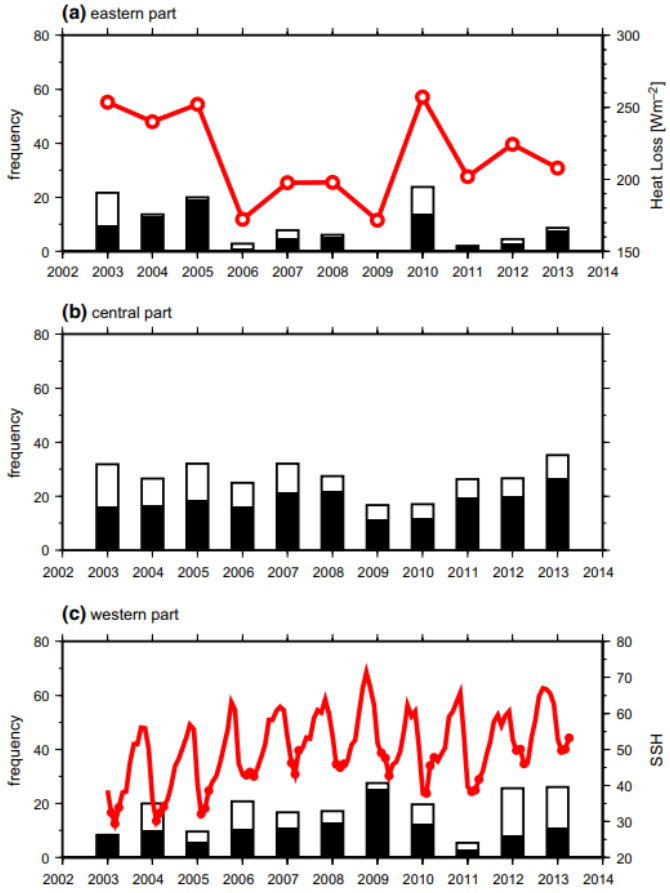

Figure 2.7

Time series of ratio [%] of profiles in the winter (February–April) deep ML (> 150 dbar) relative to all profiles (white bar): (a) the eastern part (30–40°N, 180°–160°W), (b) the central part (35–40°N, 155°E–180°), and (c) the western part (36–40°N, 140–155°E) of the L-CMW formation region (Black bar). As in white bar, but for the deep ML with the L-CMW property. Red line indicates the oceanic heat loss (sum of the NHF and Ekman heat advection; right axis) [W m^{-2}] averaged for January–March in the eastern part (a), and the monthly SSH [cm] in the western part (c). Red dots show winter values (February–April).

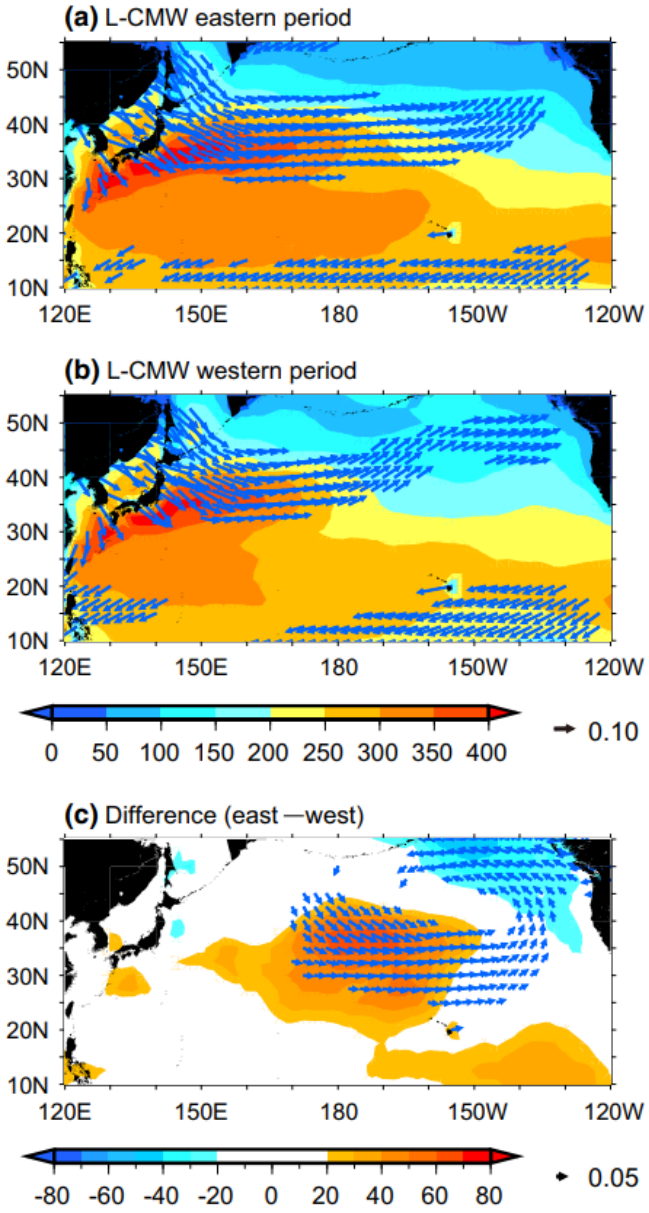

Figure 2.8

Map of the surface wind stress [N m^{-2}] (vector) and oceanic heat loss (sum of the NHF and Ekman heat advection) [W m^{-2}] (color shading) in winter (January–March): (a) the eastern period (2003–2005 and 2010) and (b) the western period (2006–2009 and 2011–2013). (c) Difference between the two periods.

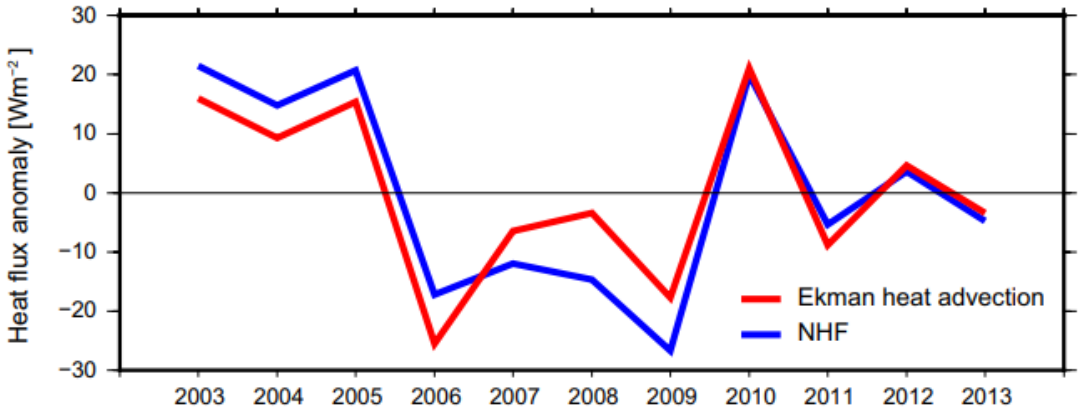

Figure 2.9

Temporal variations in the winter (February–April) NHF anomaly (blue line) and Ekman heat advection anomaly (red line) [W m^{-2}] in the eastern part of the L-CMW formation region (30–40°N, 180°–160°W).

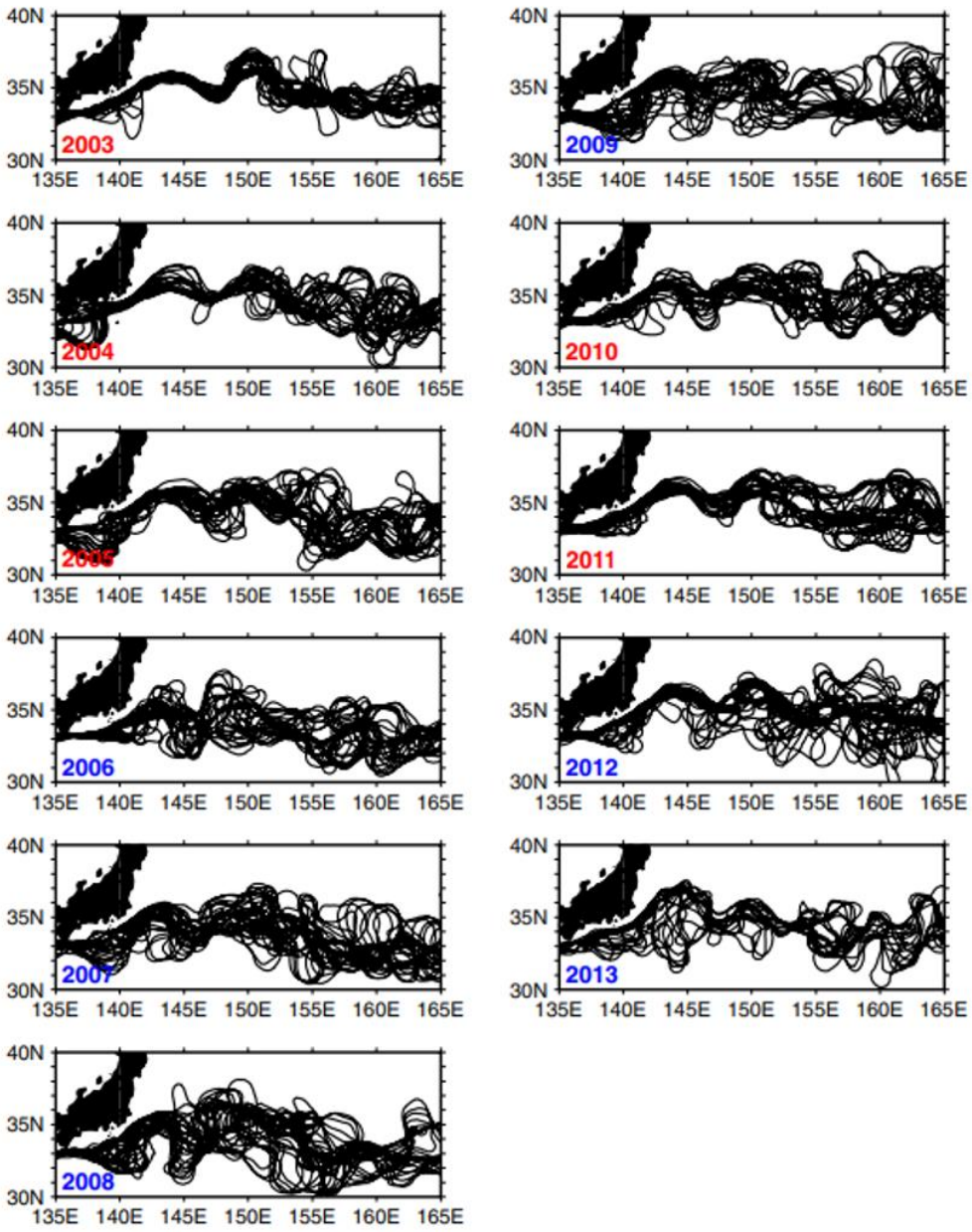

Figure 2.10

Yearly paths of the Kuroshio and the KE every two weeks, as in Qiu and Chen (2005). Paths are defined as the 110-cm SSH contour, which is consistently located at, or near, the maximum north–south gradient of SSH. Red (blue) number of year labels indicates the stable (unstable) path state.

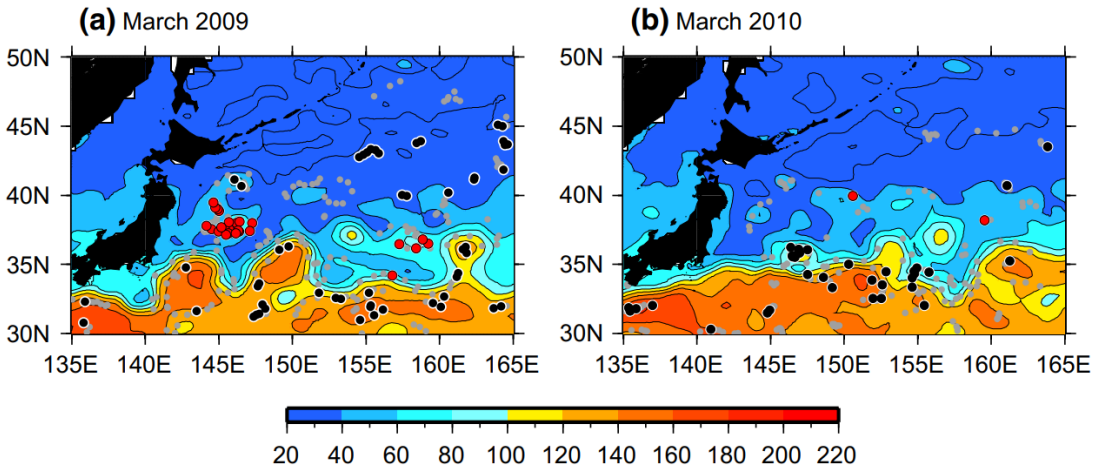

Figure 2.11

Map of the SSH [cm] in (a) March 2009 and (b) March 2010 (color shading). Red dots indicate the location of the deep ML with the L-CMW property. Black dots indicate the location of the deep ML with no L-CMW property. Gray dots indicate observation points where no deep ML was present.

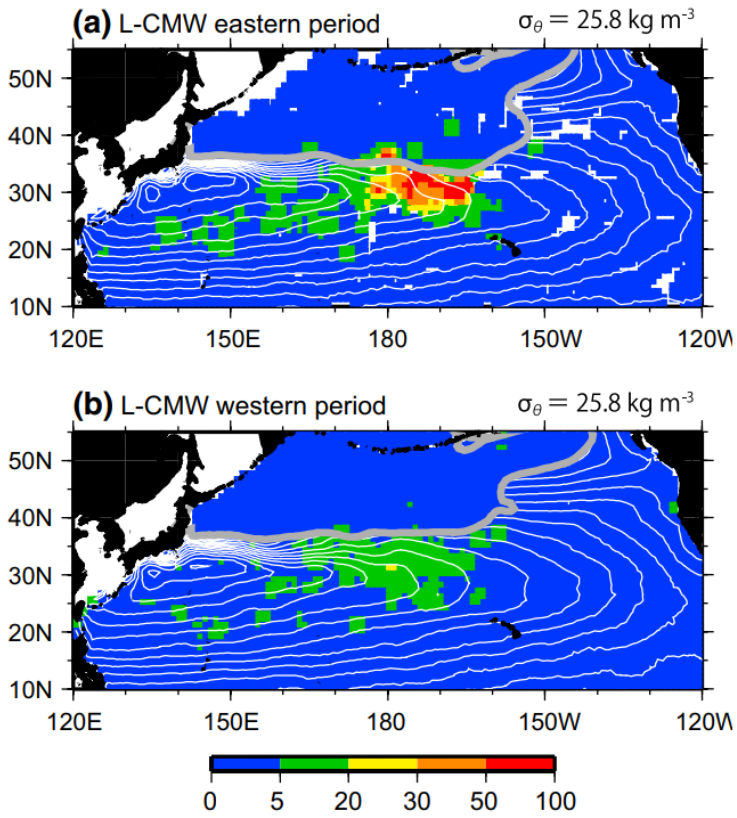

Figure 2.12

Percentage [%] of profiles with low PV (< 2.0×10^{-10} $m^{-1}s^{-1}$) on the isopycnal surface σ_θ = 25.8 kg m^{-3} in summer (June–October) (color shading): (a) the eastern period (2003–2005 and 2010) and (b) the western period (2006–2009 and 2011–2013). The percentage in each 1° × 1° grid box is calculated using data in 3° × 3° box centered on the 1° × 1° box only if 10 or more data values exist in the 3° × 3° box (see Oka et al., 2011). Gray curve indicates the outcrop line of the σ_θ = 25.8 kg m^{-3} in March; white contour indicates the acceleration potential relative to 2000 dbar (contour interval, 1 m^2 s^{-2}), averaged for April–September based on the MOAA-GPV.

Chapter 3
Long-term thermohaline variations in the North Pacific subtropical gyre

3.1 Introduction

Previous studies have reported long-term thermohaline changes in the surface and subsurface layers of the world oceans, such as global warming and intensification of salinity contrast between basins and regions (Boyer et al., 2005; Levitus et al., 2005; Deser et al., 2010; Hosoda et al., 2009; Durack and Wijffels, 2010). Previous studies demonstrated that changes of ocean temperature and salinity greatly influence not only the density-driven geostrophic ocean circulation but also the marine ecosystem (Roemmich and McGowan, 1995; Mantua et al., 1997) and sea level (Antonov, 2002; Suzuki and Ishii, 2011). Furthermore, thermohaline variations in the upper ocean can influence climate variability. For example, Schneider (2004) showed that density-compensated thermohaline anomalies that form in the Pacific subtropics can modulate the tropical climate through their advection towards the equatorial upwelling region and affecting the sea surface temperature (SST), which has a great impact on the atmosphere via air–sea interaction. Therefore, it is important to monitor ocean variations and understand their mechanisms.

In the western part of the North Pacific subtropical gyre, numerous studies of thermohaline variations and changes have been performed using data from the 137°E repeat hydrographic section conducted by the Japan Meteorological Agency (JMA) across the western North Pacific, which was initiated in 1967 and celebrated its 50th anniversary in 2016, and from Argo float profiles since 2000. North Pacific tropical water (NPTW; Cannon, 1966), which is the subsurface salinity maximum water with salinity around 35.0, is formed in the surface salinity maximum region in the North Pacific subtropical gyre; along the 137°E section, both its extent and salinity have decadal variations (Nakano et al., 2015) while its salinity increased abruptly in association with the 1976/1977 regime shift (Suga et al., 2000). Nakano et al. (2015) pointed out that the variations of NPTW are related to freshwater flux and eddy activity in the western part of the subtropical gyre. The North Pacific subtropical mode water (STMW), which forms in the deep winter mixed layer in the Kuroshio Extension (KE) recirculation gyre region (Masuzawa, 1969; Hanawa and Hoshino, 1988), has decadal variability in temperature (Taneda et al., 2000; Hanawa and Kamada, 2001; Sugimoto and Kako, 2016). The mixed layer depth (MLD) and its temperature before 1990 were controlled by cooling associated with the winter monsoon (Suga and Hanawa, 1995a; Yasuda and Hanawa, 1999). After 1990, however, the

winter MLD became more sensitive to the strength of subsurface stratification, responding to a change in the main thermocline/halocline depth (MTD) associated with oceanic Rossby waves (Sugimoto and Kako, 2016) and to changes in the path state of the KE (Qiu and Chen, 2006); the vertical entrainment process associated with the deepening of the mixed layer induced the decadal-scale temperature variations (Iwamaru et al., 2010; Sugimoto and Kako, 2016). The STMW salinity also exhibited decadal-scale variability, which is controlled by precipitation in the preceding warm season (Sugimoto et al., 2013; Kitamura et al., 2016) and meridional water exchange across the KE resulting from eddy activity associated with the dynamic state of the KE (Oka et al., 2019). The STMW has warmed at twice the rate of surface warming averaged over the global ocean as shown by historical hydrographical observations (Sugimoto et al., 2017b) and the 137°E repeat hydrographic section (Oka et al., 2019), and has freshened at a rate that is gradually accelerating along 137°E (Oka et al., 2017). The long-term trends in STMW cause warming and freshening in the main thermocline/halocline (Nakano et al., 2007; Nan et al., 2015; Oka et al., 2017) through its subduction and advection.

Decadal variability and long-term trends observed in the western North Pacific subtropical gyre, such as along the 137°E section, may have their origin farther east because of the advection of water masses such as STMW and NPTW along the anti-cyclonic subtropical gyre, oceanic Rossby waves propagating from the east, and large-scale atmospheric forcing represented by the Aleutian Low in the central North Pacific (Trenberth and Hurrell, 1994; Minobe, 1997; Sugimoto and Hanawa, 2009). Investigation in eastern regions is useful for better understanding of the 3-dimensional variability of the North Pacific subtropical gyre. However, observations in the eastern region were not adequate before the Argo era, and it is difficult to capture the decadal variability and long-term trends. The JMA has maintained hydrographic observations along 165°E, traversing the Pacific Ocean from 8°S to 50°N (Figure 3.1a), for more than 20 years since 1996 (Figure 3.1b). The observations along 165°E are valuable and effective for exploring the temporal thermohaline variability of eastern regions of the North Pacific. In this study, we investigate the long-term thermohaline variations and changes in the North Pacific subtropical gyre, focusing on relationships with those in the central North Pacific regions, by using the repeat hydrographic sections along 165°E.

3.2 Data

The JMA has conducted repeat hydrographic observations along the 165°E meridian from 8°S to 50°N since 1996 (Figure 3.1). CTD observations are typically conducted at a latitudinal interval

of 1° and repeated every year (Figure 3.1b), mainly in winter and/or summer, but not always in these seasons (Figure 3.1c). Between 7°N and 12°N, the hydrographic stations are shifted westward by about 1° (Figure 3.1a) to avoid the U.S. Armed Forces training area. The data collected are publicly available on the JMA website: http://www.data.jma.go.jp/gmd/kaiyou/db/vessel_obs/data-report/html/ship/ship_e.php. In this study, we analyzed temperature/salinity (T/S) profiles between 0° and 50°N for 1996–2018. The accuracy of the T and S observations is 0.002 °C and 0.001, respectively. Note that seasonal signals may be partially included in the following results, especially in the upper layers, although their influence would be smaller under the seasonal thermocline. In this study, we focus on the subsurface layers to reduce the influence of seasonal signals. We checked that using only summer profiles or only winter profiles has little effect on the results presented in this paper. The vertical resolution of profiles used in this study is 1 dbar. We interpolated data from each cruise onto 1° latitudinal grid intervals by using the nearest profile within $\pm 0.1°$ latitudinal range. We then calculated potential temperature (θ) and potential density (σ_θ). θ and S on isopycnal surfaces were also calculated by a linear interpolation onto a vertical interval of 0.1 kg m^{-3}.

We used the monthly mean T/S gridded dataset based on Argo float profiles, the Grid Point Value of the Monthly Objective Analysis using Argo (MOAA-GPV; Hosoda et al., 2008). The dataset is constructed by optimal interpolation of observed T/S anomalies into the World Ocean Atlas climatology (Conkright et al., 2002) on a horizontal resolution of 1° (longitude) × 1° (latitude) at each standard pressure level (every 10 dbar over 10–30 dbar, every 25 dbar over 50–150 dbar, every 50 dbar over 150–300 dbar, every 100 dbar over 300–1500 dbar, and every 250 dbar over 1500–2000 dbar). The interpolation errors are relatively large at the beginning of the 2000s, though these become small after 2003 owing to enhanced Argo coverage. To examine relationships between thermohaline variations in the ocean interior and the atmospheric forcing, we used monthly net surface heat flux (NHF, the sum of net surface short-wave radiation, net surface long-wave radiation, latent heat flux, and sensible heat flux), wind stress, evaporation (E), and precipitation (P) data from the Japanese 55-year Reanalysis (JRA-55; Kobayashi et al., 2015). The horizontal resolution of this dataset is 1.25° (longitude) × 1.25° (latitude). We also used sea surface height (SSH) anomaly data derived from satellite measurements from Archiving, Validation, and Interpolation of Satellite Oceanographic data (AVISO: www.aviso.oceanobs.com), with a horizontal resolution of 0.25° (longitude) × 0.25° (latitude) and temporal resolution of 7 days. We also used SST data from the Merged satellite and in situ data from the Global Daily Sea Surface Temperatures dataset (MGDSST; Kurihara et al., 2006)

with a horizontal resolution of 0.25° (longitude) × 0.25° (latitude).

3.3 Long-term trends and variations

To obtain a perspective on long-term thermohaline changes along 165°E, we calculated long-term trends based on a linear regression by using all profiles for 1996–2018 (Figure 3.2). Trends exceeding a 5% significance level are detected in the salinity maximum area and the main thermocline/halocline. Marked salinification is detected between 10°N and 26°N in the salinity maximum region representing NPTW (Figure 3.2b). The maximum salinification rate exceeds 0.005 year^{-1}. Long-term salinification of NPTW is also observed along the 137°E section (Oka et al., 2017). Since the vertical gradient of S is small in the salinity maximum area, the influence of isopycnal heaving (changes in the depth of isopycnal surfaces) on the salinification would be small, and the NPTW salinification reflects the salinification in the subtropical gyre associated with intensification of freshwater circulation at global scale (Hosoda et al., 2009; Durack and Wijffels, 2010). Evaporation minus precipitation (*E*–*P*) is increasing in the regions where annual evaporation exceeds annual precipitation such as the subtropics, because of enhanced evaporation due to increased atmospheric ability to hold water vapor associated with increased air temperature, and the enhanced excess evaporation results in the salinification in those regions.

In the main thermocline/halocline of the subtropical gyre between 10°N and 30°N, a significant freshening is observed (Figure 3.2b). The maximum negative salinity trend along 165°E is –0.0079 year^{-1} located around 16°N, 280 dbar. The freshening is also observed at the 137°E section (Nakano et al., 2005; Oka et al., 2017), at almost the same rate (–0.0064 year^{-1} around 22°N, 420 dbar) as that in the 165°E section. The spatially homogenous freshening in the western subtropical gyre is consistent with measurements from a zonal section along 24°N by Ren and Riser (2010). The freshening is mostly caused by density-compensated $\theta-S$ changes on isopycnal surfaces, but isopycnal heaving because the trend of θ is also mostly negative, and the trend of σ_θ is quite small and not statistically significant in the main thermocline/halocline over 10–30°N (Figures 3.2a and 3.2c).

In the southernmost part of the subtropical gyre around 10°N corresponding to the North Equatorial Current (NEC) region, marked warming and salinification (and lightening) are observed from the sea surface to 200 dbar (Figure 3.2). On the other hand, the trends in the southern subtropical gyre along the 137°E section were observed over a wider range from 4°N to 18°N, which resulted

from the long-term southward shift of the NEC (Qiu and Chen, 2012); the southward shift of the NEC allows warm and salty subtropical subsurface water to extend southward and depresses the main thermocline/halocline, resulting in warming and salinification (and lightening) in the southern subtropical gyre. Qiu and Chen (2012) pointed out that upper layer deepening (i.e., thermocline/halocline deepening) associated with wind-driven Ekman convergence also contributes to the broad warming and salinification along 137°E. The upper layer deepening is then detected as sea level rise. However, sea level rise along 165°E is considerably smaller than along 137°E (e.g., figure 1 of Qiu and Chen, 2012). This means that the effect of the upper layer deepening is less striking along 165°E. Therefore, along 165°E, the warming and salinification (and lightening) mainly reflect the southward migration of the NEC, resulting in signals confined around the NEC region.

In the main thermocline/halocline around 31°N, which is south of the KE, θ has increased at a maximum rate of 0.0872 °C year^{-1} (Figure 3.2a), which confirms the STMW warming seen in historical observations (Sugimoto et al., 2017b) and in observations at 137°E (Oka et al., 2019). On the other hand, there is no significant S trend. Therefore, it is reasonable to assume that the warming is responsible for the lightening (Figure 3.2c). Along the northern boundary of the subtropical gyre around 35°N, marked negative trends of θ and S are detected from the surface to 600 dbar, but these trends are not statistically significant.

We investigate temporal variations of θ, S, and σ_θ, averaged in six regions where θ and/or S have the largest trends (Figure 3.2). Temporal variations of θ, S, and σ_θ differ considerably among the six regions (Figure 3.3). In region 1 (8–13°N, 50–200 dbar) located in the southern boundary region of the subtropical gyre, θ and S are increasing until 2014 but decrease after 2014 (Figure 3.3a). Conversely, σ_θ is decreasing until 2014 and increases after 2014. The θ, S, and σ_θ fluctuate on an inter-annual to decadal timescale, which is related to the occurrence of El Niño/La Niña events as pointed out at the 137°E section (Shuto, 1996); the θ and S tend to decrease (increase) and σ_θ tends to increase (decrease) in El Niño (La Niña) years. This is associated with northward (southward) migration of the NEC in El Niño (La Niña) years, resulting in southward expansion (northward shrinkage) of the warm and salty subtropical subsurface water and depression (elevation) of the main thermocline/halocline (Qiu and Chen, 2012). It is suggested that the recent marked decreases of θ and S are partially due to the last strong El Niño that occurred from 2014 to 2016.

In region 2 (16–26°N, 50–150 dbar), which is located in the salinity maximum (i.e., NPTW),

S shows a clear decadal-scale oscillation with marked salinification, but θ variation is small (Figure 3.3b). In addition, σ_θ shows small fluctuation and is negatively correlated with the θ but not correlated with the S. These results imply that isopycnal heaving is not an important factor for long-term S variability in NPTW. This is probably because of the small vertical gradient of S in the salinity maximum region (region 2) (Figure 3.2b). The S variability is mainly explained by density-compensated $\theta-S$ changes on isopycnal surfaces. The decadal variability in NPTW is described in Section 4.1 and the cause of the long-term NPTW salinification is discussed in Section 5.

In region 3 (16–24°N, 200–500 dbar) and region 4 (26–29°N, 300–600 dbar) corresponding to the main thermocline/halocline, θ and S decline steadily with relatively small decadal fluctuations (Figures 3.3c and 3.3d). On the other hand, σ_θ is almost constant in both regions. Accordingly, the long-term variability in the main thermocline/halocline is not caused by isopycnal heaving and reflects the density-compensated $\theta-S$ changes on isopycnal surfaces. The variations and trends in the main thermocline/halocline are discussed in Section 4.2 and Section 5, respectively.

Region 5 (30–32°N, 200–500 dbar) and region 6 (33–36°N, 200–500 dbar) correspond to the main thermocline/halocline in the northern part of the subtropical gyre. In region 5, θ increases and σ_θ decreases (Figure 3.3e). These features probably reflect the long-term STMW warming (Sugimoto et al., 2017b). In region 6 (33–36°N, 200–500 dbar), θ and S show long-term decrease (Figure 3.3f). In addition to the trends, in regions 5 and 6, θ and S show a decadal variation (Figures 3.3e and 3.3f). The σ_θ also fluctuates on a decadal timescale with opposite phase to the variations of θ and S; i.e., θ and S increase (decrease) when σ_θ decreases (increases). This implies that the decadal variations of θ and S are caused by isopycnal heaving. Along the northern boundary of the subtropical gyre around the KE, eddy activity is high with mesoscale eddies pinched off from the KE (Qiu and Chen, 2005). In the cyclonic (anti-cyclonic) eddies pinched off southward (northward) from the KE, the MTD is elevated (depressed) and SSH is depressed (elevated). The vertical movement of the main thermocline/halocline and the sea surface are also caused by long-term variations of the Aleutian Low. In the central North Pacific, a positive (negative) anomaly of the MTD is generated in association with the strengthening (weakening) and/or northward (southward) movement of the Aleutian Low because of negative (positive) wind stress curl anomaly, and then the MTD anomaly propagates westward as oceanic Rossby waves (e.g., Sugimoto and Hanawa, 2009, 2010). It is probable that the large thermohaline variations in regions 5 and 6 are caused by the vertical movement of the main thermocline/halocline.

We examine the relationships between θ and S variability and the MTD/SSH anomaly in regions 5 and 6. Here, the MTD is regarded as the depth of the 12 °C isotherm following Uehara et al. (2003). Our results show that θ and S increase (decrease) when MTD is depressed (elevated) and SSH is elevated (depressed) (Figures 3.3e, 3.3f, and 3.4). The correlation coefficient between MTD and θ (S) is $r = 0.97$ (0.89) in region 5 and $r = 0.99$ (0.94) in region 6 (all coefficients exceed the 1% significance level). We conclude that thermohaline variations in the northern part of the subtropical gyre are greatly influenced by the vertical movement of the main thermocline/halocline. We further examine the relationship between the MTD and eddy activity using eddy kinetic energy (EKE). Here, the EKE is calculated in the KE region around the 165°E section (30–36°N, 160–170°E), following Qiu and Chen (2013):

$$\mathrm{EKE} = \frac{1}{2}\left[\left(\frac{g}{f}\frac{\partial h'}{\partial x}\right)^2 + \left(\frac{g}{f}\frac{\partial h'}{\partial y}\right)^2\right] \tag{3.1}$$

where x and y are the zonal and meridional coordinates, h' is the high-pass filtered SSH anomaly with timescales shorter than 300 days, f is the Coriolis parameter, and g is the acceleration due to gravity. The EKE fluctuates on a decadal timescale, with maxima around 1995, 2005, and 2015, and minima around 2000 and 2009 (Figure 3.4). However, the EKE is not significantly correlated with MTD ($r = 0.19$ in region 5 and $r = 0.23$ in region 6). Therefore, we conclude that mesoscale eddies are not an important factor for the long-term MTD variation and the related thermohaline variations in the KE region along 165°E.

The thermohaline variations mainly reflect θ–S changes on isopycnal surfaces and the vertical movement of isopycnal surfaces. The former is advected on isopycnal surfaces along the subtropical gyre and the latter propagates westward as oceanic Rossby waves. However, it is difficult to distinguish the two effects on the changes when considering pressure as the vertical coordinate. We further investigate thermohaline changes and variations on the σ_θ coordinate to remove the effect of the vertical movement of isopycnal surfaces. There are marked positive θ–S trends exceeding a 5% significance level in the salinity maximum from the sea surface to the layers around $\sigma_\theta = 24.5$ kg m^{-3}, and significant negative trends in the main thermocline/halocline at $\sigma_\theta = 25.0$–26.4 kg m^{-3} (Figure 3.5), similar to those seen in terms of the pressure coordinate (Figure 3.2) and along the 137°E section (Oka et al., 2017). Note that the main thermocline/halocline in the northern boundary of the subtropical gyre where marked negative θ and S trends are detected on the pressure coordinate (region 6 in Figure 3.2) also shows negative θ and S trends on the σ_θ coordinate, implying that the trends mainly reflect density-compensated θ–S changes. Isopycnal surfaces of $\sigma_\theta = 23.5$–24.5 kg

m^{-3} with marked positive $\theta-S$ trends correspond to NPTW and those of $\sigma_\theta = 25.0$–26.5 kg m^{-3} with negative $\theta-S$ trends correspond to STMW and North Pacific central mode water (CMW; Nakamura, 1996; Suga et al., 1997; Oka et al., 2011), which is formed in the deep winter mixed layer north of the KE. A maximum freshening rate in the interior of the subtropical gyre on the $\sigma_\theta = 25.5$ kg m^{-3} surface is, for example, estimated as –0.0066 $year^{-1}$ at 22°N and this rate is almost the same as the results from the 137°E section (–0.0079 $year^{-1}$ around 21°N; Oka et al., 2017). There are no significant signals below the $\sigma_\theta = 26.5$ kg m^{-3} surface, which is the densest layer to outcrop and ventilate in the North Pacific during winter. From these features, it is acceptable that the marked thermohaline changes along 165°E are induced by the changes in the winter ocean mixed layer in the main water mass formation regions. It is, however, difficult to estimate the exact long-term changes in the mixed layer in these regions since the number of observations is insufficient before the Argo era. We discuss the causes of the thermohaline trends in section 5. In the next section, we describe long-term thermohaline variability in NPTW and the main thermocline/halocline that have large trends on the isopycnal coordinate (also on the pressure coordinate) along 165°E, and investigate their causes, focusing on the winter ocean mixed layer in the outcrop region of the isopycnal surfaces.

3.4 Mechanism of long-term variations

The significant long-term changes and variations in NPTW and the main thermocline/halocline described in Section 3 are expected to reflect the thermohaline variations on isopycnal surfaces. In this section, we perform an isopycnal analysis to investigate density-compensated thermohaline changes and variations on the isopycnal surfaces and the associated mechanisms.

3.4.1 North Pacific tropical water

On the surfaces $\sigma_\theta = 23.5$, 24.0, and 24.5 kg m^{-3} that correspond to NPTW in the southern part of the subtropical gyre, both θ and S have a decadal variation, with maxima around 2004, 2011, and 2015, and minima around 1998, 2008, and 2018 (Figure 3.6). The S variations on the NPTW surfaces are similar to the S variation in the salinity maximum region on the pressure coordinate (region 2) (Figure 3.3b) in terms of both phase and amplitude. This means that the S variability of NPTW is mainly explained by variations on isopycnal surfaces as pointed out in the analysis on pressure levels in the previous section.

Previous work has reported that long-term variations of NPTW originate in the mixed layer in the western part of the NPTW formation region (21–28°N, 165°E–172°W) (Katsura et al., 2013), which is defined as the salinity maximum at the sea surface in the subtropical gyre (Figure 3.1a). We explore mixed layer temperature (MLT), salinity (MLS), and density. Here, we regard the MLT, MLS and mixed layer density as the θ, S, and σ_θ at 10 dbar, respectively. The MLS exhibits an inter-annual or longer timescale variation although the MLT has a dominant seasonal timescale (Figure 3.7a). Nonaka and Sasaki (2007) suggested that $\theta-S$ anomalies are formed on isopycnal surfaces through meridional migration of isopycnal outcrop regions at the sea surface in the South Pacific subtropical region. In the western NPTW formation region, mixed layer density is determined by MLS on an inter-annual or longer timescale (Figure 3.7a) and the meridional migration of isopycnal outcrop regions is accompanied by large MLS variation. Isopycnal surfaces corresponding to NPTW in high-MLS years are located south of those in low MLS years (Figure 3.8) because an increase of density attributable to high MLS is compensated by a decrease of density associated with increased MLT farther south. The latitudinal difference between the two periods is about 2°. It is expected that warm and salty (cold and fresh) anomalies are generated in the outcrop region as a result of high (low) MLS in the NPTW formation region and its associated southward (northward) migration to warm (cool) the outcrop region. We investigate the temporal behavior of MLS in the outcrop region of $\sigma_\theta = 23.5$, 24.0, and 24.5 kg m^{-3} in March when the mixed layer becomes deepest in the NPTW formation region. The MLS in the outcrop region shows an inter-annual to longer timescale variation that tracks with the MLS averaged in the western NPTW formation region (Figure 3.7b). The $\theta-S$ anomalies originating in the outcrop region are expected to be advected southwestward on the isopycnal surfaces along the subtropical gyre over a few years. In fact, the MLS variations in the outcrop regions are also very similar to S variations observed along the 165°E section (Figure 3.6). To examine the relationship between the thermohaline variability in the western NPTW formation region and those along the 165°E section, we perform a lag correlation analysis. The highest correlation is obtained for a 1-year lag. For example, $r = 0.86$ (over a 5% significance level) is obtained at 1-year lag between the S variation on the $\sigma_\theta = 24.0$ kg m^{-3} surface averaged over 16–20°N and the MLS variation in the outcrop region. This relationship agrees with the correlation analysis based on MOAA-GPV (Figure 3.9). The S anomaly on the $\sigma_\theta = 24.0$ kg m^{-3} surface correlated with the MLS in the outcrop region is advected southwestward from the western NPTW formation region along the subtropical gyre and passes 165°E within 1 year.

We further perform a salinity budget analysis to examine the factors affecting the MLS variation. The MLS budget equation is written as follows:

$$\frac{\partial \mathrm{MLS}}{\partial t} = \frac{(E-P)\mathrm{MLS}}{H} + \epsilon \tag{3.2}$$

where H is the MLD, defined as the depth at which σ_θ increases by 0.125 kg m^{-3} from its value at 10 dbar. The term on the left side of Eq. (3.2) is the MLS change term, which is calculated as MLS in each month minus MLS in the previous month. The first and second term on the right side is the $E-P$ flux term and residual term that includes effects as eddy diffusion. In the western NPTW formation region, because the $E-P$ flux term constantly works to increase the MLS (Figure 3.10), the residual term works to decrease the MLS. The $E-P$ flux term and the residual term have comparable magnitudes. However, the MLS change term is significantly correlated with the residual term ($r =$ 0.55, exceeding a 1% significance level) and not correlated with the $E-P$ flux term ($r =$–0.08). This means that the residual term is responsible for the inter-annual or longer timescale variation of the MLS.

Katsura et al. (2013) pointed out that eddy diffusion, which induces the MLS decrease, is an important factor for NPTW variability. We examine the relationship between the residual term and eddy activity. There are almost the same number of cyclonic and anti-cyclonic eddies in the western NPTW formation region each year, and the temporal change of eddy number is consistent with EKE variation (Figure 3.10). According to Qiu and Chen (2013), there are two zonal bands with high eddy activity in the North Pacific: the KE region and the eastward Subtropical Counter-current and Hawaiian Lee Counter-current region. The western NPTW formation region is located between the two bands. Therefore, it is expected that most eddies in the NPTW formation region are formed in the regions of high eddy activity. Salinity in these eddies is relatively low compared to the NPTW because the NPTW is characterized by the salinity maximum. The eddies transport and diffuse low-salinity water into the NPTW formation region, contributing to the MLS decrease. Both cyclonic and anti-cyclonic eddies have this effect (low-salinity transport and diffusion). The residual term is correlated with the EKE variation ($r =$ –0.58, exceeding a 1% significance level), taking large (small) negative values during high (low) EKE, consistent with a strong (weak) eddy diffusion process. This suggests that the residual term which controls the MLS variation may largely derive from eddy activity. According to Qiu (1999), eddy activity is also modulated by density changes through baroclinic instability. We perform a lag correlation analysis to determine whether eddy activity results in or is driven by the MLS changes. We obtain the highest correlation coefficient ($r =$ –0.52, exceeding 1%

significance level) when the EKE leads the MLS by a half-year, meaning that the eddy activity results in MLS changes in the NPTW formation region. Therefore, it is suggested that the MLS in the western NPTW formation region is controlled by eddy diffusion. From the results above, we conclude that thermohaline variations on the surfaces of σ_θ = 23.5–24.5 kg m^{-3} (i.e., in NPTW) along 165°E originate in the western part of the NPTW formation region to the east due to eddy diffusion and the $\theta-S$ anomalies are transported southwestward by the geostrophic flow.

3.4.2 Main thermocline/halocline

On the σ_θ = 25.0 and 25.5 kg m^{-3} surfaces, which correspond to lighter and denser parts of STMW, respectively, both θ and S fluctuate on a decadal timescale with a long-term decreasing trend (Figure 3.11). The θ and S variations on these surfaces are similar to those in the main thermocline/halocline seen on the surfaces of constant pressure (Figures 3.3c and 3.3d), implying that the variations on pressure surfaces are mostly explained by variations on the isopycnal surfaces. On the σ_θ = 26.0 kg m^{-3} surface, which represents the lighter variety of CMW, decreases in both θ and S are clear but decadal variations are not observed (Figure 3.11). On denser surfaces, both negative trends and decadal variations are very weak, and are still weak below the σ_θ = 26.5 kg m^{-3} surface (not shown). The isopycnal surfaces σ_θ = 25.0–26.5 kg m^{-3} remain below the mixed layer from spring to autumn and outcrop at the sea surface into the deep mixed layer in winter. The deep winter mixed layer with σ_θ = 25.0–26.5 kg m^{-3} (i.e., outcrop region of those isopycnals, and the formation region of STMW and CMW) extends from the western boundary region of the North Pacific to the central North Pacific (Figure 3.12), which is the upstream region for the 165°E section in terms of the anti-cyclonic subtropical gyre (Figure 3.12). It is therefore presumed that the $\theta-S$ variations along the 165°E section originate in the winter mixed layer in the central North Pacific, and are distributed by advection of STMW and CMW along the subtropical gyre.

In the central North Pacific (28–40°N, 165°E–170°W) (Figures 3.1a and 3.12), which covers the eastern part of the formation region of STMW and CMW, MLT in winter (March) has a long-term variation with amplitude of 0.6 °C, while the winter MLS is less variable, so that winter mixed layer density is determined by the MLT (Figure 3.13a). Therefore, in this region, meridional migration of the isopycnal outcrop region is accompanied by the MLT variations. The isopycnal surfaces corresponding to STMW and CMW in years with increased MLT are located north compared to those in years with decreased MLT (Figure 3.14). The northward (southward) migration to the cold and fresh

(warm and salty) outcrop region during years of increased (decreased) MLT generates cold and fresh (warm and salty) anomalies in the outcrop region (Figure 3.13b). The $\theta-S$ anomalies that originate in the outcrop region in the central North Pacific are expected to be advected southwestward on the isopycnal surfaces along the anti-cyclonic subtropical gyre over several years (Figure 3.12). In fact, the MLT variations in the outcrop region are similar to, and lead by a few years, θ and S for the $\sigma_\theta =$ 25.0 and 25.5 kg m^{-3} surfaces along the 165°E section (Figure 3.11). To examine the relationship between thermohaline variations in the outcrop region and along 165°E, we perform a lag correlation analysis between the MLT in the outcrop region and θ on the isopycnal surfaces in the 165°E section. Significant correlation coefficients are obtained with 2–4 years lag. For example, $r =$ 0.91 (over a 5% significance level) is obtained with a 3-year lag between θ variation on the $\sigma_\theta =$ 25.5 kg m^{-3} surface averaged over 21–25°N along 165°E and the MLT variation in the outcrop region. Correlation analysis based on Argo data (Figure 3.15) also shows the circulation of the θ anomalies; the θ anomaly correlated with the MLT in the outcrop region in the central North Pacific circulates in the subtropical gyre and reaches 165°E within 2–4 years. Sasaki et al. (2010) and Kolodziejczyk and Gaillard (2012) found that density-compensated $\theta-S$ anomalies in the upper main thermocline/halocline in the eastern subtropical North Pacific circulate along the subtropical gyre. However, interestingly, the thermohaline variability in the main thermocline/halocline along the 165°E section is coherent meridionally over the broad subtropical gyre (Figures 3.11a and 3.11b), though much more time should be needed for the $\theta-S$ anomalies to reach the southern part of the subtropical gyre if the pathway is based on climatological streamlines. This is also seen in the correlation analysis based on Argo data (Figure 3.15). The θ anomaly derived from MLT in the outcrop region is detected widely on the isopycnal surface at lags of 2 and 3 years (Figures 3.15c and 3.15d), suggesting a rapid southward spread of the θ anomalies. Since eddy activity is elevated in the western to central part of the subtropical gyre compared to the eastern part (e.g., Qiu and Chen, 2013), mesoscale eddies (Zhang et al., 2014; Shi et al., 2018) and/or sub-mesoscale phenomena may play important roles in the rapid distribution of the θ anomalies. The high-correlation regions shrink to the east of 150°E at lags of 4 and 5 years and do not reach regions farther west (Figures 3.15e and 3.15f). This implies that thermohaline variations in the western boundary region are driven by other mechanisms such as those mentioned in the Introduction. It is also interesting that high correlation coefficients appear in the KE recirculation gyre around 30°N, 145°E at a lag of 2 years (Figure 3.15c), and then propagate southwestward (Figures 3.15d, 3.15e, and 3.15f). One possible process connecting the thermohaline

variations in the western North Pacific with those in the central North Pacific is the propagation of oceanic Rossby waves. The atmospheric forcing in the central North Pacific is the primary control of the winter MLT there (Yasuda and Hanawa, 1997), and indirectly affects the winter MLT in the KE recirculation gyre after a few years through westward propagation of oceanic Rossby waves that control vertical entrainment and influence the MLT (Sugimoto and Kako, 2016). The relationship between thermohaline variability in the two regions should be investigated in future work.

Unlike the case of the $\sigma_\theta =$ 25.0 and 25.5 kg m^{-3} surfaces, long-term variations are extremely small on the $\sigma_\theta =$ 26.0 kg m^{-3} surface and denser surfaces along the 165°E section though there is MLT variation in the outcrop region (Figure 3.11c). This might be because the outcrop region of such denser surfaces in the central North Pacific is less connected to the interior of the subtropical gyre because those surfaces usually outcrop farther north in the subtropical gyre (Figure 3.1a). The $\theta-S$ anomalies generated on those surfaces would mostly be transported by eastward flow rather than directly distributed southward to the subtropical gyre. The circulation and dissipation of $\theta-S$ anomalies on such denser surfaces are an interesting topic for future work.

Previous studies demonstrated that a variation of winter cooling attributable to the atmospheric forcing associated with Aleutian Low activity is the major factor controlling the winter MLT variation in the central North Pacific (Yasuda and Hanawa, 1997). We further perform a mixed layer heat budget analysis during winter. The mixed layer heat budget equation is written as

$$\frac{\partial \mathrm{MLT}}{\partial t} = \frac{Q_{\mathrm{NHF}} + Q_{\mathrm{ek}}}{\rho C H} + \epsilon \tag{3.3}$$

where Q_{NHF} is NHF averaged for January–March, Q_{ek} is the divergence of Ekman heat transport averaged for January–March, C is the specific heat of sea water (4200 J kg^{-1} °C^{-1}), ρ is mixed layer density, and H is MLD averaged for January–March. The divergence of Ekman heat transport (Q_{ek}) is calculated as

$$Q_{\mathrm{ek}} = \frac{C}{f}(\boldsymbol{k} \times \boldsymbol{\tau}) \cdot \boldsymbol{\nabla} T \tag{3.4}$$

where $\boldsymbol{k}$ is the vertical unit vector, $\boldsymbol{\tau}$ is wind stress, and T is SST. The term on the left side of Eq. (3.3) is the MLT change term, calculated as MLT in March minus MLT in the previous December. The first and second term on the right-hand side is the atmospheric forcing term and residual term that includes ocean effects such as vertical entrainment, geostrophic heat advection, and eddy heat flux. The MLT change term shows decadal fluctuation with almost the same amplitude as a decadal winter MLT variation, and is almost fully explained by the atmospheric forcing (Figure 3.16). This result

means that the variation of winter cooling attributable to atmospheric forcing has a great influence on the decadal winter MLT variation. Note also that contributions of the residual term to the MLT change during winter are small in the central North Pacific. From the results above, we conclude that density-compensated $\theta-S$ anomalies are generated in the winter mixed layer in the central North Pacific by the migration of winter outcrop regions associated with the MLT variation that is greatly affected by the winter atmospheric forcing, and the anomalies are distributed into the main thermocline/halocline over the subtropical gyre through advection of STMW.

3.5 Summary and discussions

Using repeat hydrography along 165°E for 23 years (1996–2018), we have examined the long-term thermohaline changes and variations in the North Pacific subtropical gyre. In the southernmost part of the subtropical gyre, significant warming and salinification with an inter-annual or longer timescale variation are detected in the NPTW, which is characterized by the salinity maximum. $\theta-S$ in NPTW reflects density-compensated $\theta-S$ on isopycnal surfaces, and derives from MLT and MLS in the isopycnal outcrop region. In the NPTW formation region, the MLS determines the mixed layer density on an inter-annual or longer timescale, and controls the meridional position of the outcrop region. Increased (decreased) MLS induces southward (northward) migration of the isopycnal outcrop region, and results in warm and salty (cold and fresh) $\theta-S$ anomalies. The significant salinification in the mixed layer in the outcrop region is not detected by Argo floats over 2001–2018 (Figure 3.7b), but salinification in the subtropical gyre including the NPTW formation region has been reported in many studies based on long-term historical observations (e.g., Durack and Wijffels, 2010). Considering the process of MLS-driven migration of the outcrop region and following $\theta-S$ anomalies on the isopycnal surfaces, we suggest that the significant warming and salinification along the 165°E section are associated with the recent salinification in the subtropical gyre.

In the main thermocline/halocline, a significant cooling and freshening, and a decadal variation are observed. $\theta-S$ in the main thermocline/halocline also reflects density-compensated $\theta-S$ on isopycnal surfaces, and derives from MLT and MLS in the isopycnal outcrop region. In the central North Pacific, where STMW and CMW are formed, the MLT determines mixed layer density on a decadal timescale, and controls the meridional position of the outcrop region. High (low) MLT causes northward (southward) migration of the isopycnal outcrop region, and results in cold and fresh (warm and salty) $\theta-S$ anomalies in STMW and CMW. The anomalies in STMW are brought down

into the main thermocline/halocline over the subtropical gyre through advection, but those in CMW are not observed in the subtropical gyre probably because the outcrop region is not well connected to the interior of the subtropical gyre. Following the process that generates θ–S anomalies on isopycnal surfaces through meridional migration of the outcrop region, the significant cooling and freshening in the main thermocline/halocline can be attributed to basin-scale warming in the North Pacific in the context of global warming (Levitus et al., 2005; Deser et al., 2010). For example, assuming that the surface mixed layer in the central North Pacific warms by 1 °C, θ and S on the $\sigma_\theta = 25.5$ kg m^{-3} surface in the central part of the subtropical gyre change –0.54 °C and –0.16, respectively; these changes are estimated by comparing θ and S in the winter outcrop region of $\sigma_\theta = 25.5$ kg m^{-3} in the central North Pacific derived from the present climatology (averaged for 2003–2018) based on MOAA-GPV and those from a "warmed" climatology (i.e., present climatology + 1 °C). Further, a cooling and freshening that is enhanced in the main thermocline/halocline results in strengthening of the vertical θ/S gradient in the upper ocean, i.e., the strengthening of the main thermocline/halocline itself. Thus, global warming changes the primary structure of the subsurface ocean.

Signals of long-term thermohaline changes and variations in the upper ocean are distributed over the subtropical gyre by the movement of water masses. An understanding of the formation and circulation of water masses will help to improve our knowledge of long-term thermohaline changes and variations in the upper ocean. The role of eddies in water mass formation (e.g., Kouketsu et al., 2012) and spreading (e.g., Zhang et al., 2014; Shi et al., 2018) has been recognized. To develop our understanding of long-term changes in the upper ocean, further examination of the formation, circulation, and dissipation of water masses using both observational data and eddy-resolving models will be useful.

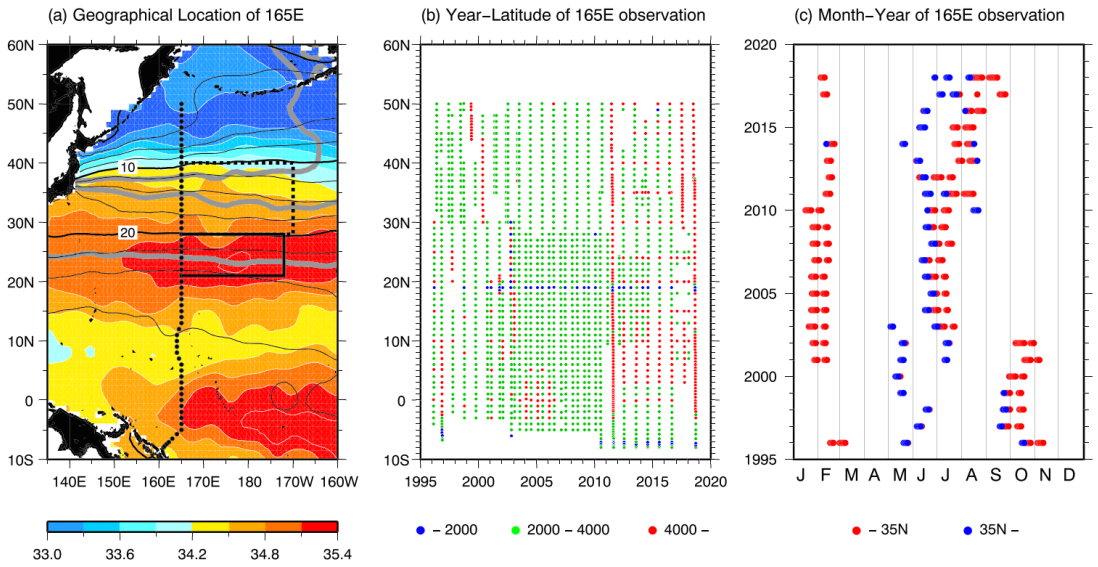

Figure 3.1

(a) Geographical location of ship-board CTD stations along 165°E (dots). Contours and shading indicate potential temperature [°C] and salinity at 10 dbar in March averaged over 2003–2018 based on MOAA-GPV data (Hosoda et al., 2008; see details in the text), respectively. Gray contours denote isopycnals of 24.0, 25.5 and 26.0 kg m^{-3} at 10 dbar in March. Solid rectangle indicates the western NPTW formation region (21–28°N, 165°E–172°W) and dashed rectangle indicates the central North Pacific region (28–40°N, 165°E–170°W). (b) Time-latitude diagram of the observations. Color indicates the maximum depth [m] of the observations. (c) Monthly distribution of the observations as a function of years. Red (blue) circles indicate that casts south (north) of 35°N exist.

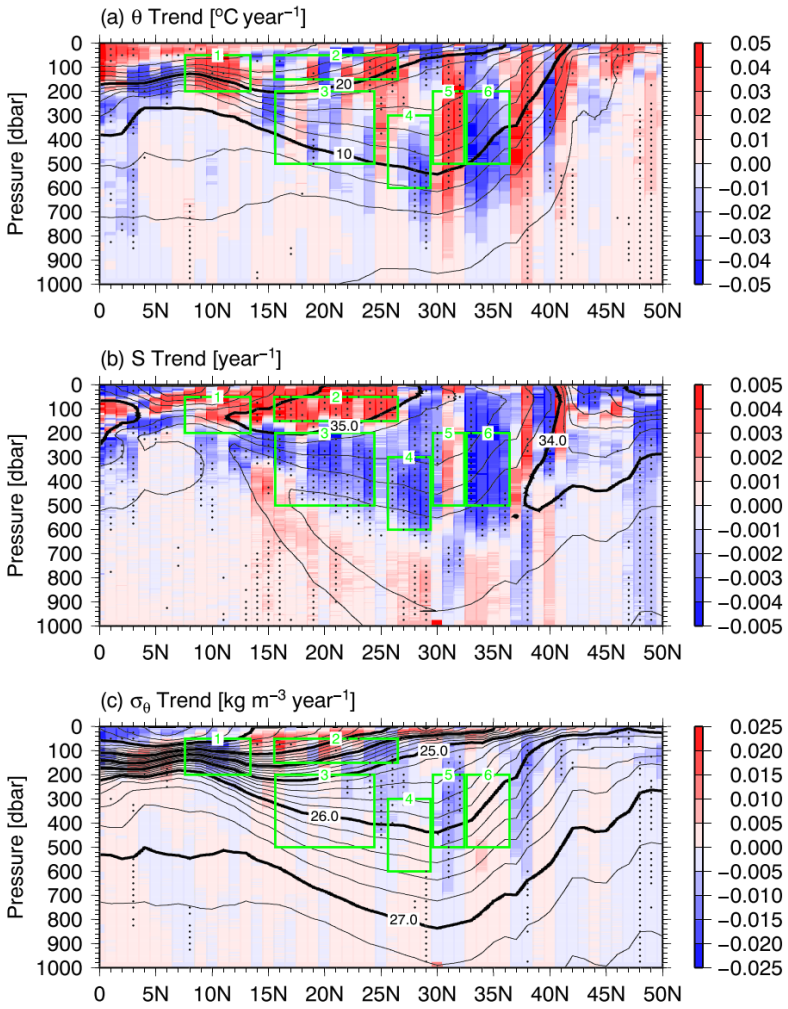

Figure 3.2

Linear trends of (a) θ [°C year^{-1}], (b) S [year^{-1}], and (c) σ_θ [kg m^{-3} year^{-1}] along 165°E on the pressure [dbar] coordinate. Contours indicate mean values calculated for 1996–2018. Dots are drawn at grid points where the linear trend exceeds a 5% significance level. The six green rectangles indicate regions where θ, S, and σ_θ are averaged in Figure 3.3.

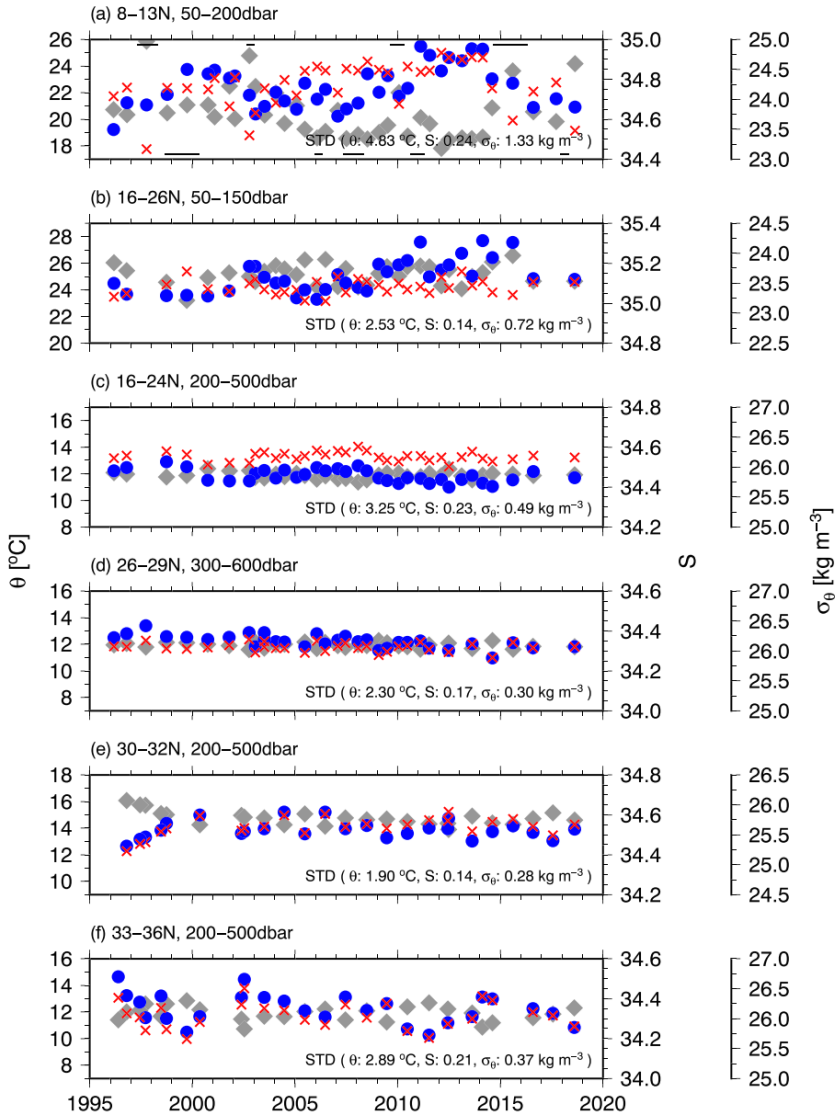

Figure 3.3

Time series of θ [°C] (red crosses; left axis), S (blue dots; right inner axis), and σ_θ [kg m^{-3}] (gray lozenges; right outer axis) averaged in (a) region 1 (8–13°N, 50–200 dbar), (b) region 2 (16–26°N, 50–150 dbar), (c) region 3 (16–24°N, 200–500 dbar), (d) region 4 (26–29°N, 300–600 dbar), (e) region 5 (30–32°N, 200–500 dbar), and (f) region 6 (33–36°N, 200–500 dbar). θ, S, and σ_θ are averaged when there are observations for > 60% of grid points in each region. Standard deviations of θ, S, and σ_θ in every observation are temporally averaged and shown in each panel. Horizontal bars in the top (bottom) of panel (a) mean periods of El Niño (La Niña).

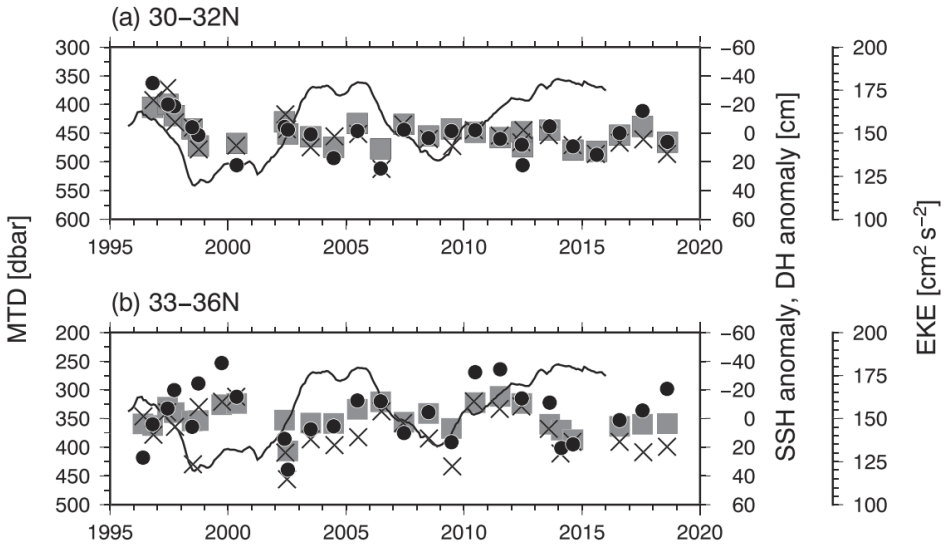

Figure 3.4

Time series of MTD [dbar] (dots; left axis) along the 165°E section and SSH anomaly [cm] (crosses; right inner axis) averaged in the month when MTD is plotted along 165°E over (a) 30–32°N and (b) 33–36°N. Gray squares show anomaly of dynamic height (DH) [cm] relative to 1500 dbar (right inner axis) calculated from 165°E hydrography. The black line indicate 61-month running averaged EKE [$cm^2\ s^{-2}$] (right outer axis) in the KE region around the 165°E section (30–36°N, 160– 170°E).

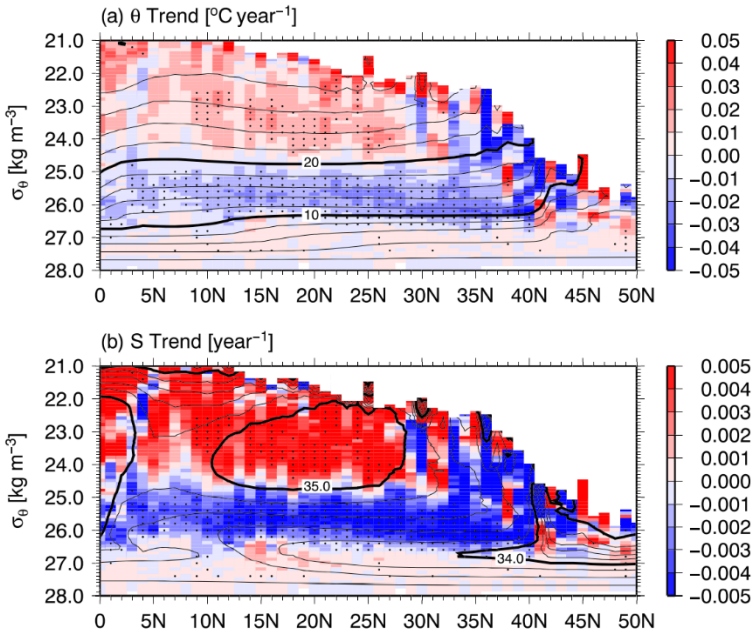

Figure 3.5

Linear trend of (a) θ [°C year^{-1}] and (b) S [year^{-1}] along 165°E on the σ_θ [kg m^{-3}] coordinate. Contours indicate mean values calculated for 1996–2018. Dots are drawn at grid points where the linear trend exceeds a 5% significance level.

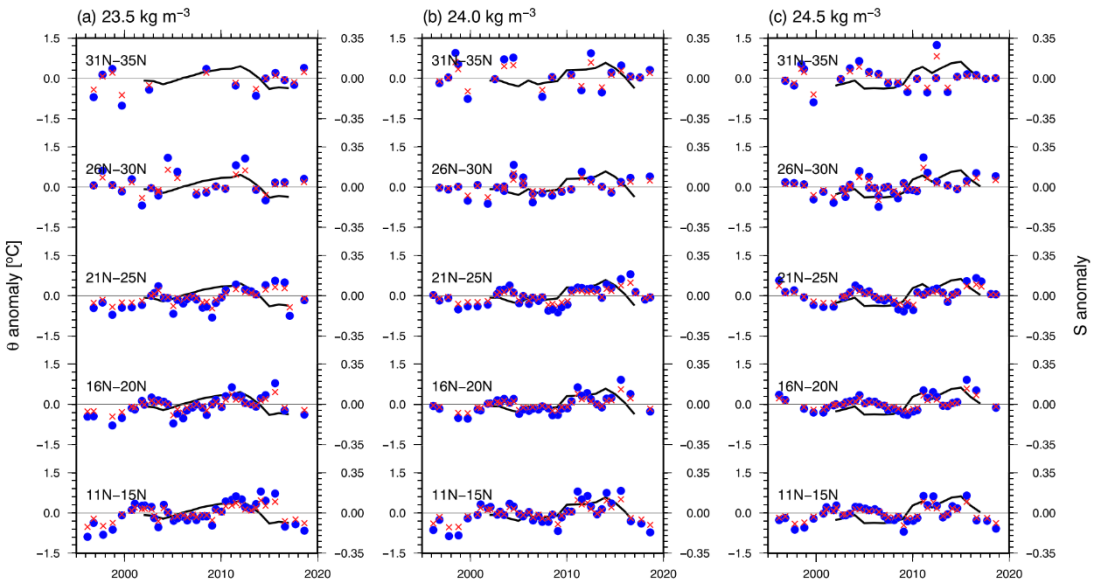

Figure 3.6

Time series of θ [°C] (red crosses; left axis) and S (blue dots; right axis) anomalies along the 165°E section on isopycnal surfaces of σ_θ = (a) 23.5, (b) 24.0, and (c) 24.5 kg m^{-3} every 5° (latitude) over 11–35°N. θ and S were averaged when there were observations for > 60% of grid points in each range. Black lines indicate 3-year running averaged mixed layer salinity (MLS) anomaly in March averaged on the isopycnal outcrop region at the sea surface (within $\pm$0.03 kg m^{-3}) in the western NPTW formation region (21–28°N, 165°E–172°W).

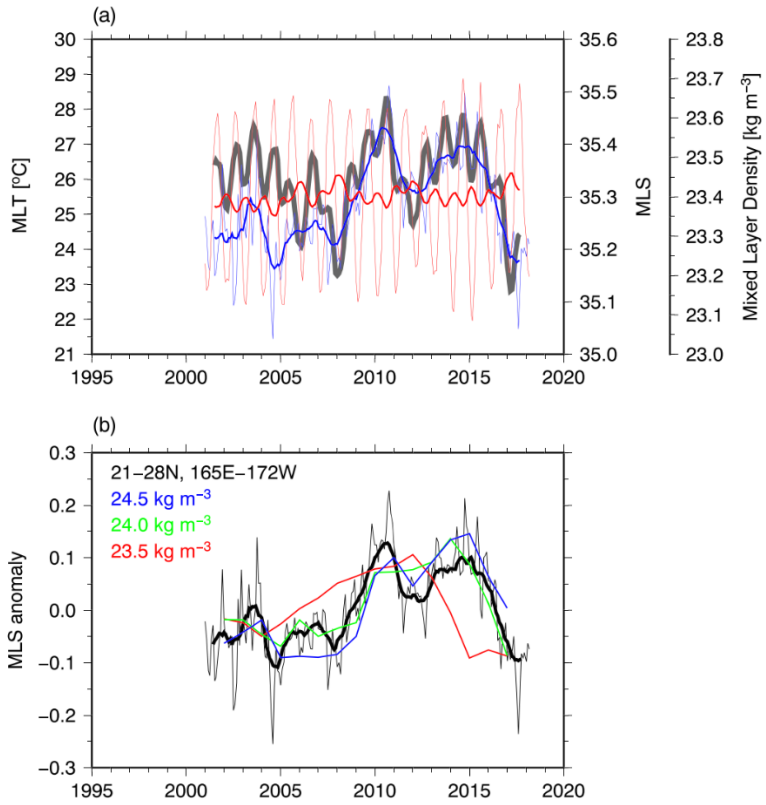

Figure 3.7

(a) Time series of MLT [°C] (red; left axis) and MLS (blue; right inner axis) averaged in the western NPTW formation region (21–28°N, 165°E–172°W). Thick lines indicate 13-month running means. Gray line indicates 13-month running averaged mixed layer density [kg m^{-3}] (right outer axis). (b) Time series of MLS anomaly averaged over the western NPTW formation region (anomaly of MLS in panel (a)) (black) and 3-year running averaged MLS anomaly in the outcrop region of $\sigma_\theta = 23.5$ (red), 24.0 (green), and 24.5 kg m^{-3} (blue) in March.

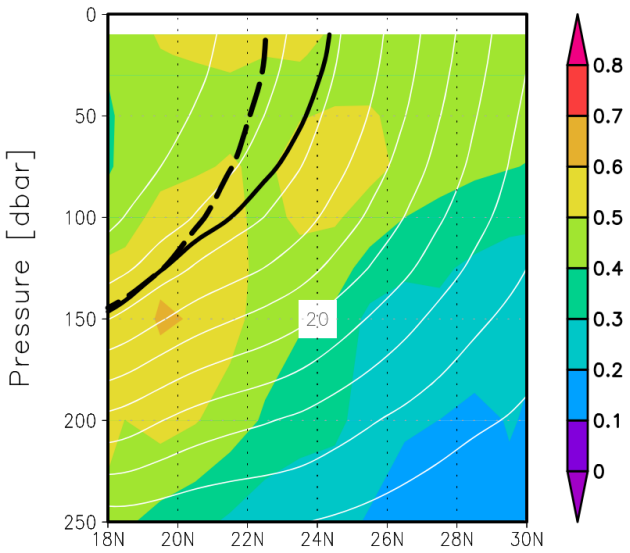

Figure 3.8

Depth-latitude diagram of θ [°C] averaged zonally from 165°E to 172°W. White contours and color shading indicate θ and its standard deviation averaged in March for 2003–2018, respectively. The contour interval is 1°C. A black dashed line indicates the $\sigma_\theta = 24.0$ kg m^{-3} isopycnal in March averaged in high-MLS years (2010, 2011, 2013–2015), and a black solid line indicates the average in low-MLS years (2002, 2004–2006, 2008, 2017). High (low)-MLS years are determined as years when MLS is higher (lower) than the average $+0.7$ (-0.7) standard deviation.

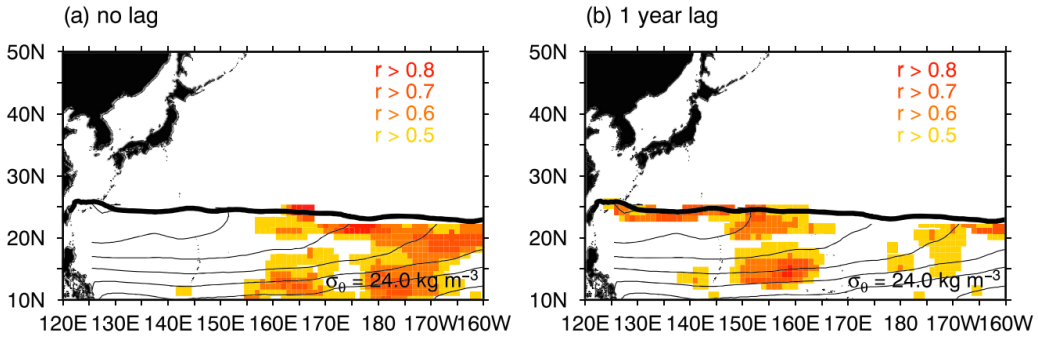

Figure 3.9

Distribution of the correlation coefficient (r) between S on the isopycnal surface of $\sigma_\theta = 24.0$ kg m^{-3} at each horizontal grid point and the MLS averaged on the winter outcrop region at the sea surface in the western NPTW formation region at (a) no lag and (b) 1-year lag. A black line indicates the mean position of the outcrop of $\sigma_\theta = 24.0$ kg m^{-3} in March. Contours indicate acceleration potential [m^2 s^{-2}] relative to 1500 dbar. $r > 0.7$ ($r > 0.6$) exceeds the 5% (10%) significance level.

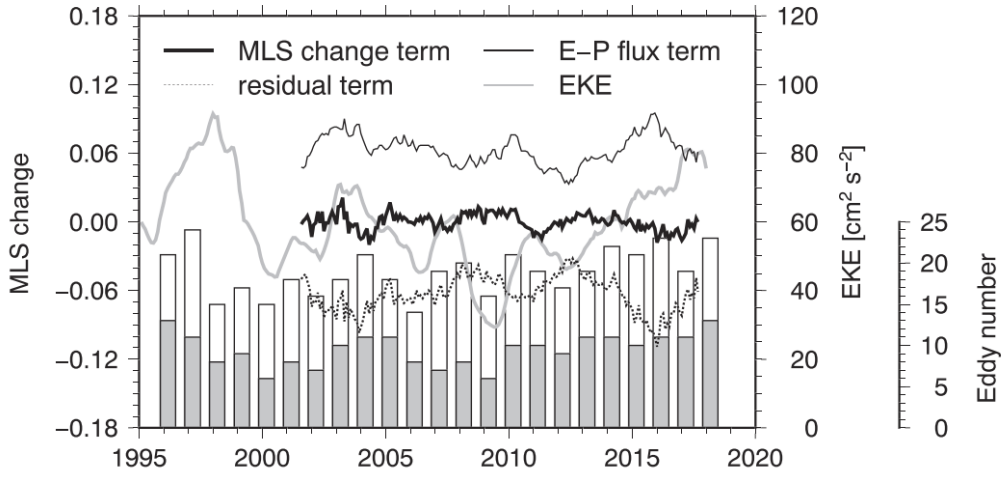

Figure 3.10

Time series of the MLS change term (thick line), $E-P$ flux term (thin line), and residual term (dashed line) in Eq. (3.2) in the western NPTW formation region (21–28°N, 165°E–172°W) (left axis). The MLS change term, $E-P$ flux term, and residual term are calculated after smoothing of MLS, MLD, and $E-P$ using a 13-month running mean filter. Gray line indicates 13-month running averaged EKE [$cm^2\ s^{-2}$] (right inner axis). White and gray bars indicate the number of cyclonic and anti-cyclonic eddies (right outer axis) in the western NPTW formation region in March, respectively. Eddies are counted visually based on SSH data averaged in March.

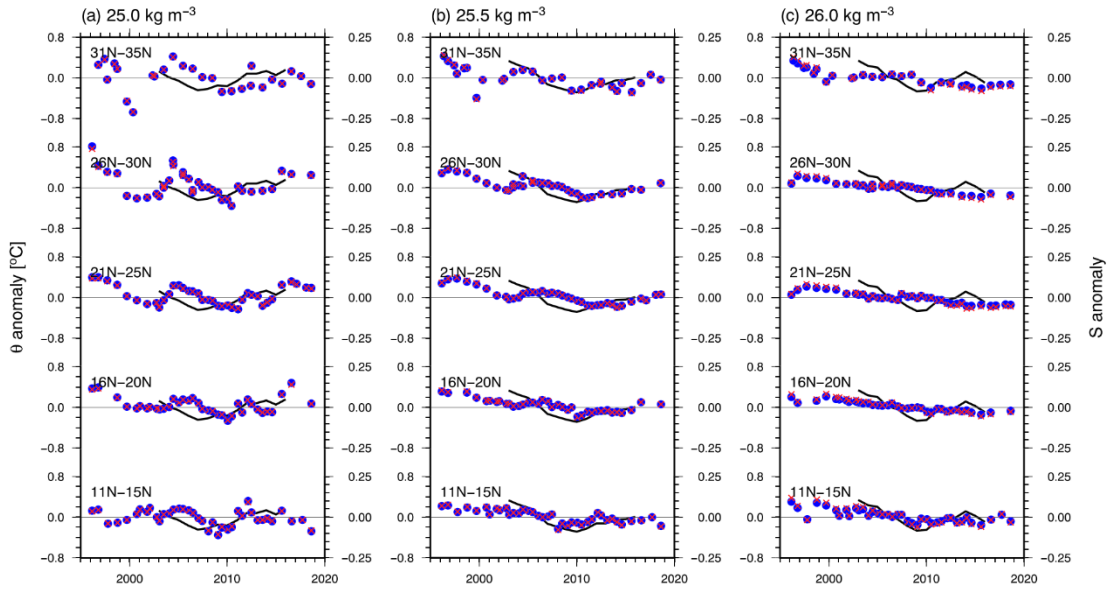

Figure 3.11

Same as Figure 3.6, but for $\sigma_\theta =$ (a) 25.0, (b) 25.5, and (c) 26.0 kg m^{-3}. Black lines indicate 5-year running mean MLT anomaly [°C] in March averaged on the isopycnal outcrop region at the sea surface (within $\pm$0.03 kg m^{-3}) in the central North Pacific (28–40°N, 165°E–170°W).

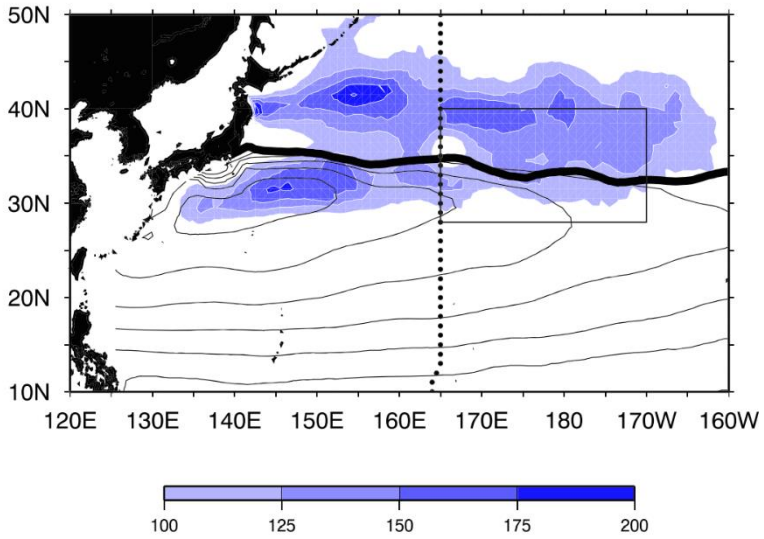

Figure 3.12

Distribution of MLD in March [m] (color) based on MOAA-GPV. Contours denote acceleration potential [$m^2\ s^{-2}$] on the $\sigma_\theta = 25.5$ kg m^{-3} surface relative to 1500 dbar. The rectangle indicates central North Pacific region (28–40°N, 165°E–170°W). The thick line denotes the average position of the $\sigma_\theta = 25.5$ kg m^{-3} isopycnal. Dots indicate the hydrographic stations along 165°E.

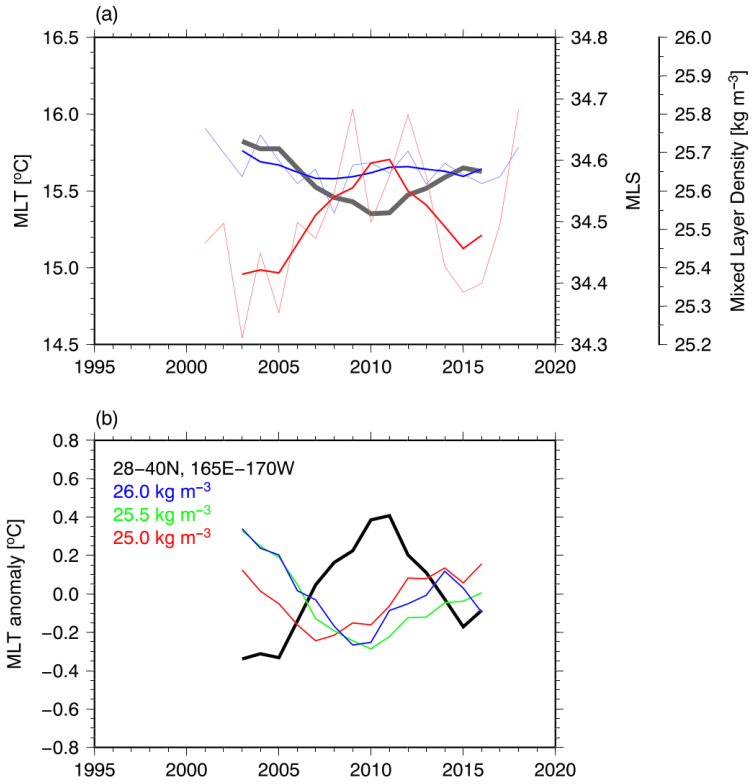

Figure 3.13

(a) Time series of MLT [°C] (red; left axis) and MLS (blue; right inner axis) averaged over the central North Pacific (28–40°N, 165°E–170°W) in March. Thick lines indicate 5-year running means. Gray line indicates 5-year running mean mixed layer density [kg m^{-3}] (right outer axis). (b) Time series of 5-year running mean MLT anomaly [°C] averaged over the central North Pacific in March (anomaly of MLT in panel (a)) (black) and MLT [°C] in the outcrop region of $\sigma_\theta = 25.0$ (red), 25.5 (green), and 26.0 kg m^{-3} (blue) in March.

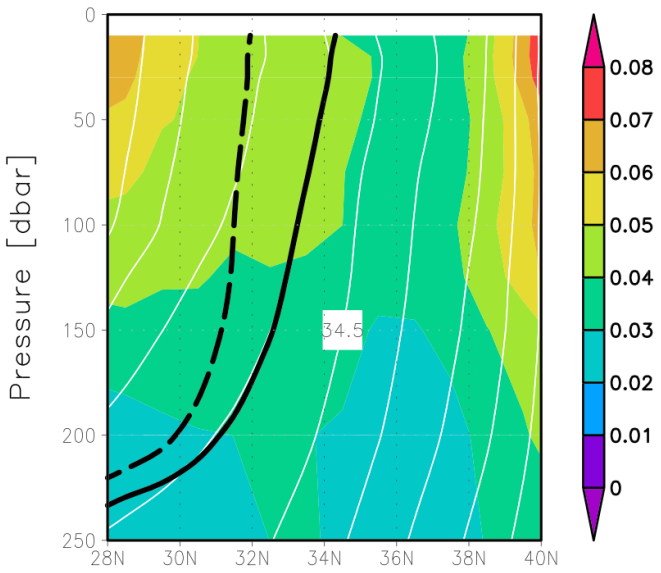

Figure 3.14

Depth–latitude diagram of S averaged zonally from 165°E to 170°W. White contours and color shading indicate S and its standard deviation averaged in March for 2003–2018, respectively. The contour interval is 0.1. The black solid line indicates the $\sigma_\theta = 25.5$ kg m^{-3} isopycnal in March averaged in high-MLT years (2009–2012), and the black dashed line indicates that in low-MLT years (2002, 2003–2005, 2015). High (low)-MLT years are determined as years when MLT is higher (lower) than the average +0.7 (–0.7) standard deviation.

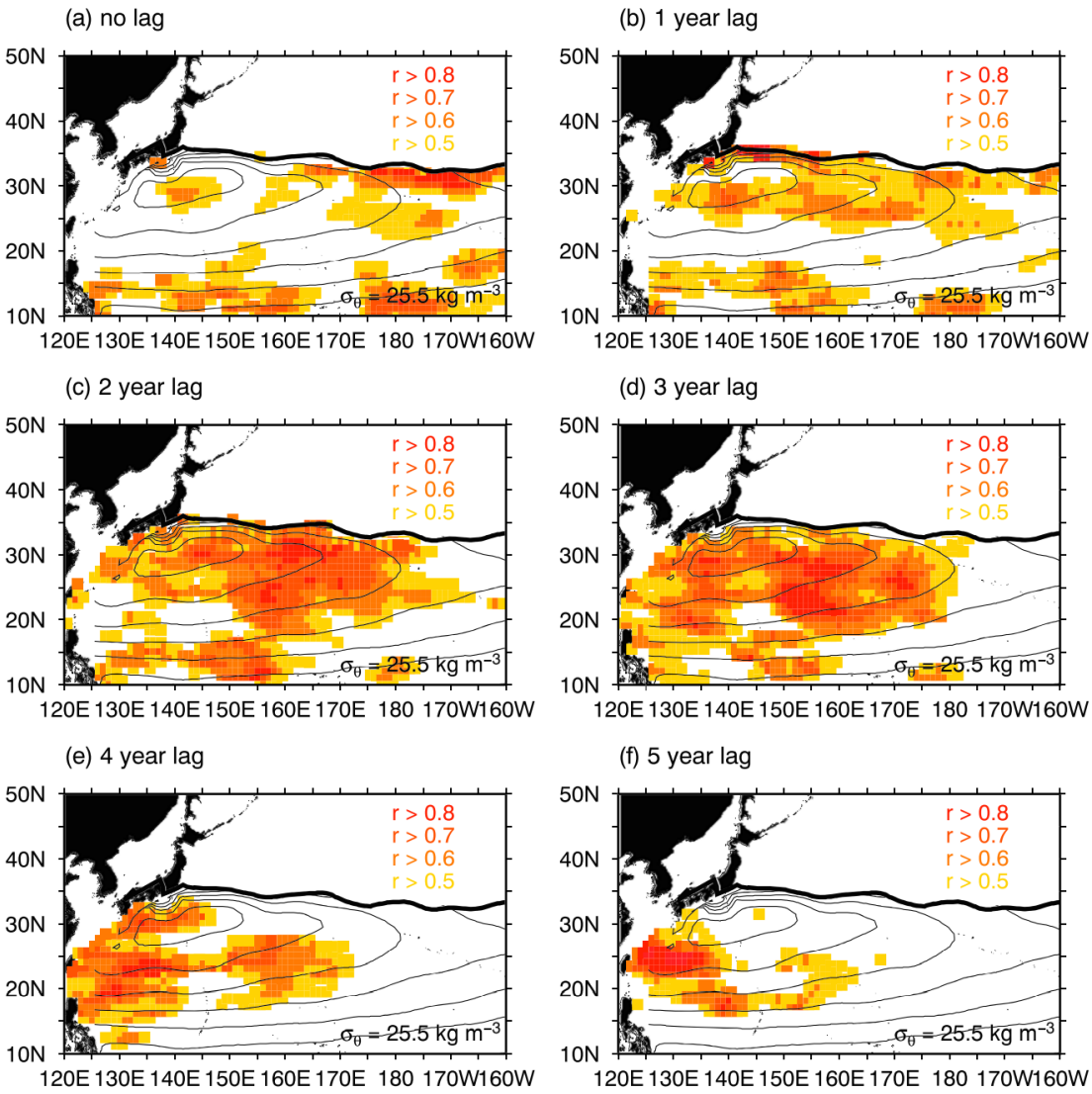

Figure 3.15

Distribution of the correlation coefficient (r) between θ on the $\sigma_\theta = 25.5$ kg m^{-3} isopycnal surface at each horizontal grid point and the MLT averaged on its winter outcrop region at the sea surface in the central North Pacific at (a) no lag, (b) 1-year lag, (c) 2-year lag, (d) 3-year lag, (e) 4-year lag, and (f) 5-year lag. The black line indicates the mean position of the outcrop of $\sigma_\theta = 25.5$ kg m^{-3} in March. Contours indicate acceleration potential [m^2 s^{-2}] relative to 1500 dbar. $r > 0.7$ (0.6) in (a) and (b) exceeds the 5% (10%) significance level. $r > 0.7$ in (c)-(f) exceeds the 10% significance level.

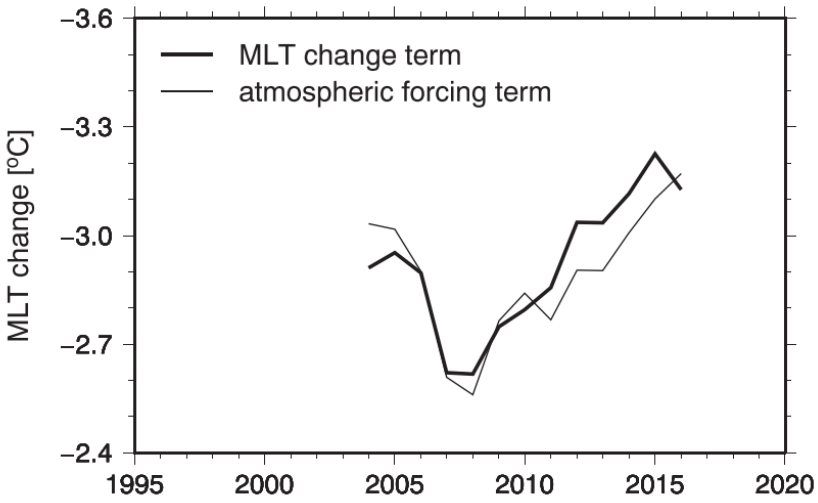

Figure 3.16

Time series of the MLT change term [°C] (thick line) and the atmospheric forcing term [°C] (thin line) in Eq. (3.3) over the central North Pacific (28–40°N, 165°E–170°W). The MLT change term, atmospheric forcing term, and residual term are calculated after smoothing of MLT in March and December, MLD, Q_{NHF}, and Q_{ek} averaged for January–March using a 5-year running average filter.

Chapter 4
Temporal variations of net Kuroshio transport

4.1 Introduction

The Kuroshio is the western boundary current of the North Pacific subtropical gyre. It flows northeastward along the south coast of Japan and transports large amounts of heat from the western tropical Pacific to the mid-latitude North Pacific. The Kuroshio transport can substantially influence regional and basin-scale climate variability by modulating sea surface temperature (SST) in the western boundary region (e.g., Qiu, 2000; Wu et al., 2012). Improved satellite observations and numerical simulations have revealed significant influences of the Kuroshio and its extension, the Kuroshio Extension (KE) on the overlying atmosphere (e.g., Nonaka and Xie, 2003; Tanimoto et al., 2011; Nakamura et al., 2012; Sugimoto, 2014; Kuwano-Yoshida and Minobe, 2017; Sugimoto et al., 2017a).

Since the Kuroshio is a part of the wind-driven circulation in the North Pacific subtropical gyre, many authors have investigated causes of Kuroshio transport variations, focusing on basin-scale wind stress curl (WSC) fields (e.g., Deser et al., 1999; Yasuda and Kitamura, 2003). The wind stress (WS) field over the mid-to-high latitude in the North Pacific largely reflects the Aleutian Low (AL) activity in the northern North Pacific (e.g., Trenberth and Hurrell, 1994) (Figure 4.1). Past works pointed out the AL shows two types of variations; one is intensity variations and the other is meridional position changes (e.g., Sugimoto and Hanawa, 2009). The AL variations have significant impacts on the Kuroshio transport as a result of oceanic baroclinic responses (e.g., Yasuda and Hanawa, 1997; Sugimoto et al., 2010). The North Pacific subtropical high (NPSH) is distributed in the eastern North Pacific (Figure 4.1). Recent study of Qiu et al. (2020) pointed out that WSC changes around the NPSH region have significant influences on the KE path state. However, roles of the NPSH on the Kuroshio transport have not been revealed yet.

The Kuroshio transport varies across a wide range of timescales from inter-annual to bi-decadal (e.g., Qiu and Joyce, 1992; Sugimoto et al., 2010). However, the length of the Kuroshio transport time series used in the previous studies is about 35 years at most, which is not sufficient to investigate low-frequency variations like decadal and bi-decadal variations. The Japan Meteorological Agency (JMA) started hydrographic observations along 137ºE across the Kuroshio in 1967 (Figure 4.2). This repeated hydrography is powerful tool to understand a temporal variation of the Kuroshio

transport. In this study, using the 137ºE sections, we produce a time series of Kuroshio transport which is 10 years longer than that in most existing studies based on integration of geostrophic current velocity relative to 1000 dbar, and then examine causes of the Kuroshio transport variation in terms of the AL and NPSH. We also consider the impact of the Kuroshio transport on SST and air-sea heat exchanges.

4.2 Data

The JMA has maintained hydrographic observations along 137ºE traversing the western North Pacific from 34ºN to 3ºN or further south for more than 50 years (Figure 4.2). The observation has been repeated every winter (usually in January) since 1967, and every summer (usually in July–August) since 1972. Details of the 137ºE observation are reviewed in Oka et al. (2018).

We construct a vertical-meridional gridded point values of winter and summer sections along 137ºE for 0–2000 dbar by applying an optimal interpolation (OI) method for Temperature/Salinity (*T*/*S*) profiles taken by a reversing thermometer, Nansen bottles, Conductivity-Temperature-Depth (CTD) profiler with Niskin bottles, expendable bathythermographs (XBT), expendable CTD (XCTD), and digital bathythermograph (DBT) (Table 4.1), as follows: (1) We produce an average cross section for 0–2000 dbar in each season, using data for 1992–2017 when observations deeper than 2000 dbar have been conducted, except for summer of 1992, 1993, 2002, and 2009 and winter of 1994 and 1995 because of shallow observations and a lack of observations (Figure 4.2a); (2) we vertically interpolate *T*/*S* profiles from a reversing thermometer and Nansen bottles into 1 dbar by a method of Akima (1979), and vertically smooth those from a CTD profiler with Niskin bottles, XBT, XCTD, and DBT by Gaussian filter with an e-folding scale of 10 dbar. Note that, in summer of 2009, CTD profiles observed within ±2º (longitude) from Argo floats, research cruise by the Fisheries Research Agency (FRA), and another cruise by the JMA are also used (Table 1) since observations between 15–34ºN are missing (Figure 4.2a) because of severe weather; (3) we apply the OI with an exponential function with a horizontal and vertical decay scale of 160 km and 400 dbar with the average section in (1) as a first guess; and (4) finally we obtain summer and winter cross section with a horizontal interval of 1/3º for 31–34ºN, 1/2º for 30–31ºN, and 1º for 3–30ºN (Figure 4.2b) and a vertical interval of 1 dbar. For cruises whose observations are mainly in upper 1250 dbar (mainly before 1992, Figure 4.2a), grid point values are calculated in upper 1250 dbar. Based on this OI gridded *T*/*S* dataset, we calculate dynamic height and zonal geostrophic current velocity relative to the reference level of 1000 dbar as a depth of no-motion. We checked the following results are insensitive to the choice of the reference

level; for instance, almost identical results were obtained by using 1250 dbar as the reference level.

We also use monthly WS and sea level pressure (SLP) data from Japanese 55-year Reanalysis (JRA-55; Kobayashi et al., 2015) with a horizontal resolution of 1.25º (longitude) × 1.25º (latitude). WSC is calculated over the North Pacific. Since the WSC is defined by spatial derivative of WS, it tends to include small-scale features. To examine large-scale variations, we spatially smooth the WSC field by applying a 9-point average (with a weight of 1.0 for the center grid, 0.5 for side grids, and 0.3 for corner grids). The latitudinal position of the AL is defined as the latitude of a grid point with the minimum winter SLP within the region of 30–65ºN, 140ºE–140ºW and AL intensity is defined as the minimum winter SLP within this region. The intensity of the NPSH is defined as the maximum winter SLP within 20–40ºN, 120–150ºW.

4.3 Calculation of net Kuroshio transport

The Kuroshio takes various paths (e.g., Kawabe, 1995), and westward flows associated with a cold-core eddy and the Kuroshio Counter Current (KCC) are located in the north and south. Therefore, a calculation of zonal transport in a fixed meridional range (e.g., regarding 30–34ºN along the 137ºE section as the Kuroshio) is not appropriate to estimate Kuroshio transport. We calculate the transport based on a method of Sugimoto et al. (2010); (1) we determine the northern and southern boundaries of westward flow of the cold-core eddy, Kuroshio, and KCC in each section based on a distribution of dynamic height relative to 1000 dbar (Figure 4.3); (2) and we obtain cold-core eddy transport, Kuroshio transport, and KCC transport by integrating zonal geostrophic current velocity from sea surface to 1000 dbar depth within each region (Figure 4.4). Note that the transport can be underestimated when the Kuroshio takes a meander path and crosses the 137ºE section with a slanted angle. We investigated the Kuroshio velocity based on satellite measurements and found that the zonal component of the Kuroshio velocity at 137ºE is consistent with the absolute Kuroshio velocity though there is a little difference between them during the Kuroshio large meander path state. Effects of the Kuroshio path changes on estimation of the transport would not be large. In this study, we especially focus on net eastward transport in the northwestern subtropical gyre and refer to it as net Kuroshio transport. We define the net Kuroshio transport as a sum of cold-core eddy transport, Kuroshio transport, and KCC transport, and explore its annual-mean variation since 1972 when the summer cruise started (Figure 4.5a). The net Kuroshio transport is controlled by atmospheric forcing through Sverdrup balance. Therefore, we focus on a relationship between the net Kuroshio transport variation

and atmospheric variations. Each component of the net Kuroshio transport would be influenced by not only atmospheric forcing but also various oceanic processes such as thermohaline variations in surface water masses and interaction with oceanic eddies. Their variations should be investigated by using eddy-resolving ocean models in future studies.

4.4 Temporal variations of net Kuroshio transport

The net Kuroshio transport fluctuates on inter-annual and decadal timescales (Figure 4.5). The inter-annual variation is obvious for 1972–1990 and 2000–2018. On the other hand, the decadal-scale variation is clearly detected before 2000, but absent after 2000.

We investigate causes of the net Kuroshio transport variation with a focus on winter (December–February) when the atmospheric forcing is strong. A lag-correlation analysis shows that the net Kuroshio transport responds to changes of winter WSC in the central North Pacific (24–34ºN, 150ºE–175ºW; hereafter, we refer to this region as the forcing region), characterized by the negative peak in winter WSC climatology after 2 years (Figure 4.6): the WSC in the forcing region also has inter-annual and decadal timescales. The lag of 2 years is consistent with the time to reach the Kuroshio region south of Japan from the forcing region with a propagation speed of oceanic Rossby waves. We also detect positive correlation coefficients between the net Kuroshio transport and the WSC near the center of the AL (Figure 4.6a). This result implies a close relationship between the net Kuroshio transport variation and AL activities as pointed out in the previous studies and discussed in the following paragraphs.

We investigate the winter WSC variation in the forcing region from a view point of large-scale atmospheric circulation. We perform an Empirical Orthogonal Function (EOF) analysis for winter WSC in the subtropical North Pacific (15–40ºN, 140ºE–120ºW) (Figures 4.7a, 4.7b, 4.7d, and 4.7e). The first mode is dominant along the westerlies and easterlies in the north and south of the forcing region (Figure 4.7b). This mode well reflects meridional movements of the AL (Figure 4.7a) (correlation coefficient r = 0.68, exceeding a 1% significance level), which show an inter-annual timescale before 1985 and after 1995, and decadal timescale before 2000 (Figure 4.8b). The second mode has larger variance in the center of the North Pacific subtropical gyre (Figure 4.7e), and well represents intensity fluctuations of the AL (Figure 4.7d) (r = –0.82, exceeding a 1 % significance level) with a decadal timescale for 1970–1990 (Figure 4.8a). It is worth noting that the AL intensity is related to an occurrence of El Nino-Southern Oscillation (ENSO) events especially before 1980s and after

2000s (Figure 4.7d), supporting Sugimoto et al. (2009).

The net Kuroshio transport changes its predominant timescale with time (Figure 4.5). It is therefore expected that the dominant forcing field on the Kuroshio would change with time. We investigate relationships between the winter WSC in the forcing region and the first two leading EOF modes by performing a running correlation analysis (Figures 4.7c and 4.7f). The WSC is significantly correlated with the second mode throughout the whole period. Especially, during a period around 1970–1990 when the AL intensity fluctuates on a decadal timescale, the high correlation coefficients are obtained. Also, around 2000s when the AL intensity shows sharp positive and negative peaks corresponding to an occurrence of ENSO events, significant correlation coefficients are detected. The WSC reflects the first mode for a specific period around 1970s and 2000s when, meridional position changes of the AL show an inter-annual timescale. The WSC variations in the forcing region associated with the two types of AL variations result in the net Kuroshio transport variations. A close look of Figures 4.8a and 4.8b indicates an inter-annual timescale variation of the AL is not significant after 2000 when significant inter-annual-scale signals are detected in the net Kuroshio transport. The NPSH is distributed in the region southeast of the AL, the latitudinal band of which is consistent with the Kuroshio region. The winter NPSH intensity clearly shows decadal timescale before 2000 and inter-annual timescale after 2000 (Figure 4.8c). This NPSH intensity fluctuation is not linked to a meridional movement of the AL (r = 0.02). Furthermore, we found that the NPSH intensity is significantly correlated to the first EOF mode of winter WSC especially after 1970 (r = 0.57, exceeding a 1% significance level) (see Figure 4.7a). Therefore, we strongly suggest that the NPSH intensity would play an important role on the net Kuroshio transport through modulation of the WSC in the forcing region by shifting westerlies meridionally.

4.5 Summary and discussions

We produced a gridded dataset of repeated hydrographic sections along 137ºE based on an OI method, and then investigated net Kuroshio transport for 1972−2018. The net Kuroshio transport indicated two marked timescales with a period dependency; an inter-annual variation before 1990 and after 2000 and a decadal variation before 2000. Such dominant timescale changes in the net Kuroshio transport are never previously reported. We further showed that the net Kuroshio transport variation resulted from a combination of the meridional movements of the AL, intensity fluctuations of the AL, and intensity fluctuations of the NPSH. The AL meridional movements and NPSH intensity

fluctuations (AL intensity fluctuations) are responsible for an inter-annual (decadal) net Kuroshio transport variation: such atmospheric variations are reflected to the winter WSC in the central North Pacific and result in the net Kuroshio transport variation with a lag of 2 years through a westward propagation of oceanic Rossby waves from the central North Pacific to the Kuroshio region south of Japan. Numerous studies have demonstrated impacts of the AL activities on the Kuroshio and wind-driven North Pacific subtropical gyre (e.g., Sugimoto et al., 2010), but those of the NPSH variations have been less understood yet. One important contribution of this paper is indicating a possible link between the net Kuroshio transport variation and NPSH intensity fluctuation. A relationship between NPSH variations and the Kuroshio and large-scale ocean circulation should be further investigated in future work. Since the NPSH dominates the North Pacific in a warm season, to evaluate the NPSH influence on the Kuroshio, summer atmospheric forcing may also need to be considered.

As previously pointed out (e.g., Sugimoto and Hanawa, 2009), the AL intensity exhibits a bi-decadal-scale variation with positive peaks around 1970, 1990, and 2010 and negative peaks around 1980 and 2000 (Figure 4.8a) while the bi-decadal-scale signals are mainly within a cone of influence in a wavelet analysis. Interestingly, the bi-decadal feature is also detectable in the net Kuroshio transport throughout the analysis period (Figure 4.5) with negative peaks around 1975, 1995, and 2015 and positive peaks around 1985 and 2005, although this is also within a cone of influence. These imply a possible link between the net Kuroshio transport and AL intensity on a bi-decadal timescale. Further accumulation of observational data will enable us to investigate the bi-decadal variation of net Kuroshio transport in the future.

It should be noted that changes in a Kuroshio path can affect the Kuroshio transport estimated by our method (i.e., an integration of zonal velocity): the transport can be underestimated when the Kuroshio takes a meander path and crosses the 137ºE section with a slanted angle. To examine the influence of a Kuroshio path on the transport, we investigated absolute and zonal velocity for 1993–2018 based on satellite measurements (Copernicus Marine Environment Monitoring Service; marine.copernicus.eu). We found that the zonal velocity is mostly consistent with the absolute velocity (Figure 4.9) whereas their difference becomes large reaching 20% in 2017–2018 of the latest Kuroshio large meander event, implying an underestimate of the transport. However, a horizontal resolution of satellite-derived surface current data is 1/4º (longitude) ×1/4º (latitude), which is not sufficient to resolve the Kuroshio. Eddy-resolving ocean general circulation models would be useful for more accurate estimation of the Kuroshio transport and investigation of its variability.

The Kuroshio plays an important role for heat transport from low- to mid-latitude North Pacific, and would modulate SST in the western boundary region. A composite map represents that an increase of late-winter (February−March) SST in the Kuroshio/KE region associated with large net Kuroshio transport, and then, the vigorous heat is released from the ocean to atmosphere (Figures 4.10a, 4.10b, and 4.10c). These features are clearly observed in recently developed high-resolution dataset of ERA5 (Copernicus Climate Change Service, 2017) (Figures 4.10d, 4.10e, and 4.10f). These results indicate active influence of the Kuroshio on the overlying atmosphere. We suggest that the Kuroshio transport is a key factor for the establishment of air-sea interaction framework. Previously, influences of current path variations such as the Kuroshio large meander and KE dynamic state changes on SST and overlying atmosphere are well discussed (e.g., Qiu et al., 2020; Sugimoto et al., 2020, 2021). In future work, in addition to such current path changes, impacts of the net Kuroshio transport variation should be focused.

Table 4.1

Observational data used to construct a grid dataset of the 137ºE hydrographic section. Before 1990, temperature was mainly measured by a reversing thermometer and water samples were obtained from Nansen bottles at standard depths. The vertical interval of the measurement becomes larger with a depth from about 10 m around the sea surface to 250 m at the maximum in deep layers. Since 1990, the observation has been conducted by using a CTD profiler with Niskin bottles. The vertical resolution of the *T*/*S* profiles is 1 dbar

Observation	Period
Reversing thermometer, Nansen bottle	1967–1989
CTD (JMA)	1990–
CTD (FRA)	Summer of 2009
Argo float	Summer of 2009
XBT (T-5) (− 1830 m)	1993–1996
XBT (T-6) (− 460 m)	1997–1999
XBT (T-7) (− 760 m)	1990, 2000–
XCTD (− 1100 m)	1999–2010
DBT (− 900 m)	1986–1989

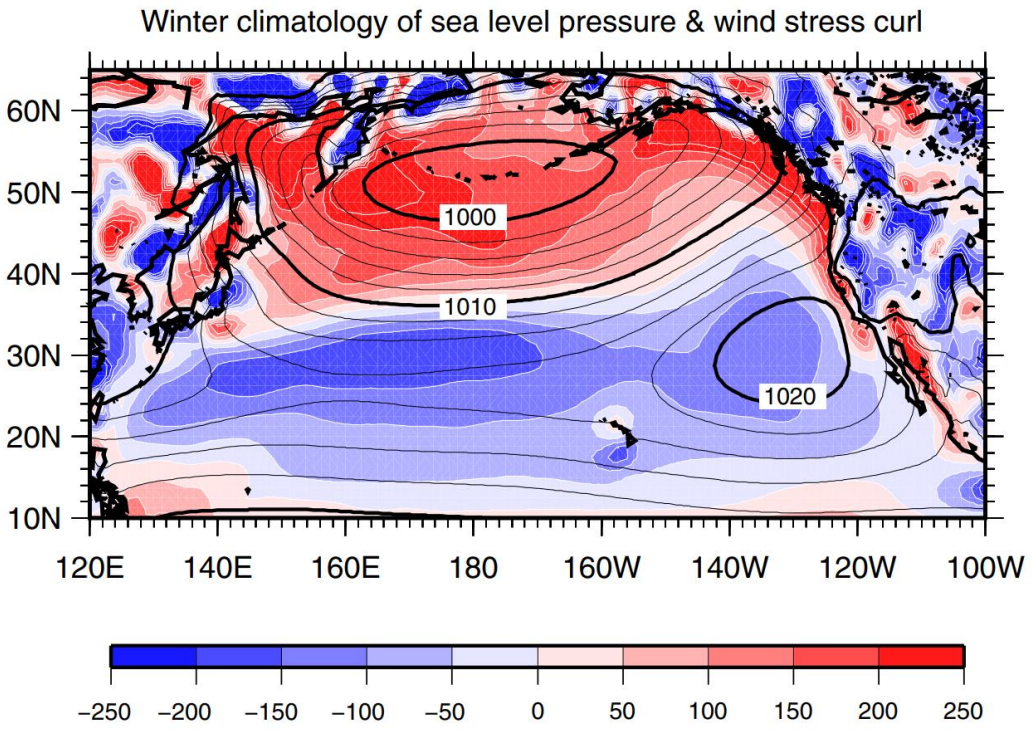

Figure 4.1

Winter (December–February) climatology (1959–2018) of sea level pressure [hPa] (contour) and wind stress curl [$\times 10^{-9}$ kg m^{-2} s^{-2}] (color) over the North Pacific from Japanese 55-year Reanalysis (see section 2 for detail).

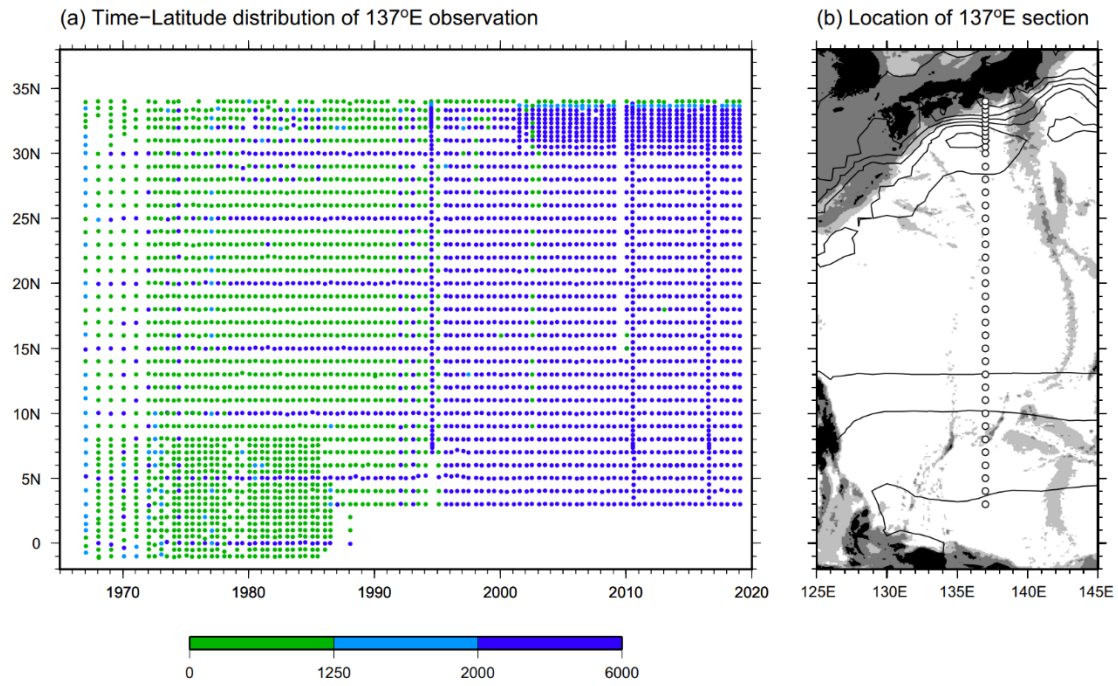

Figure 4.2

(a) Time-latitude diagram of hydrographic observations along the 137ºE section. Color indicates the maximum depth [m] of each observation. (b) Geographical location of the 137ºE section. Open circles are drawn at grid points of an optimally interpolated dataset of the 137ºE section (see text). Regions with dark (light) gray shading are shallower than 1500 m (3000 m). Contour denotes average sea surface height [cm] for 1993−2012 from Archiving, Validation, and Interpolation of Satellite Oceanographic data (AVISO: www.aviso.oceanobs.com). The contour interval is 20 cm

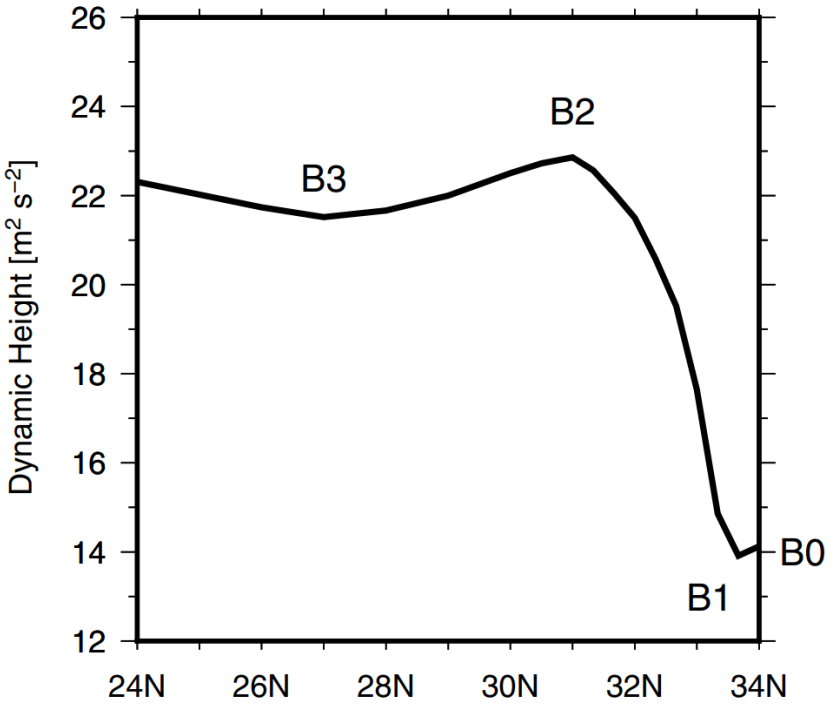

Figure 4.3

Schematic diagram of surface dynamic height [m^2 s^{-2}] relative to 1000 dbar along the 137ºE section. The regions of westward flow by the cold-core eddy, Kuroshio, and KCC are defined as regions between B0 and B1, between B1 and B2, and between B2 and B3, respectively.

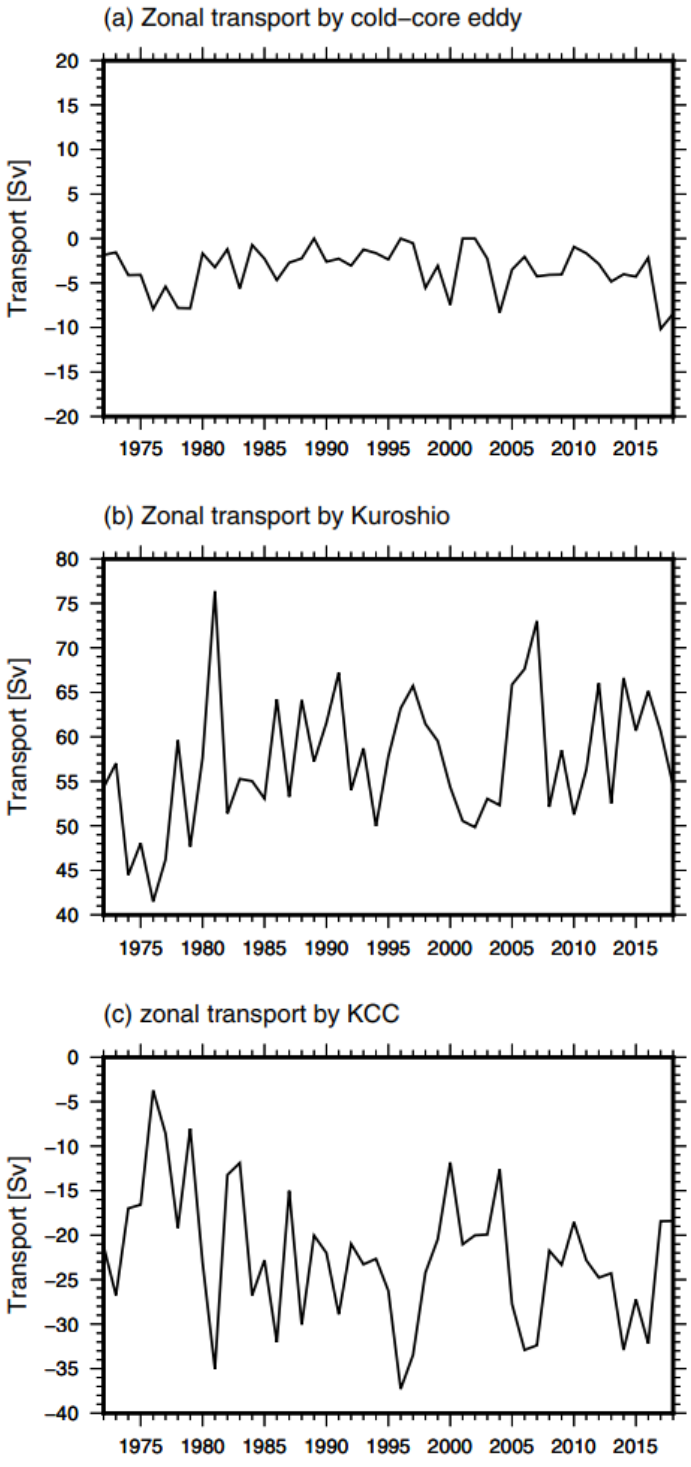

Figure 4.4

Time series of annual-mean (a) cold-core eddy transport [Sv; 1 Sv = 10^6 m^3 s^{-1}], (b) Kuroshio transport [Sv], and (c) KCC transport [Sv]. Positive values mean eastward transport

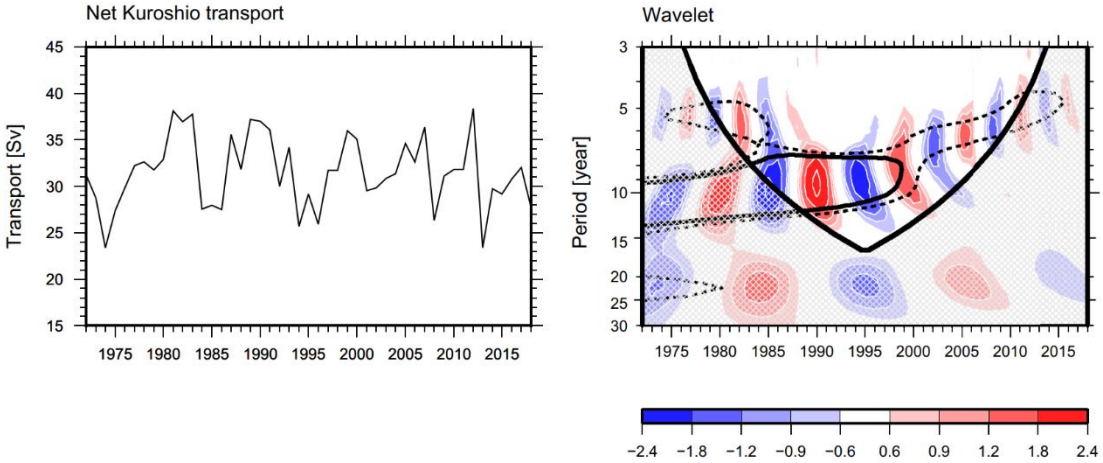

Figure 4.5

(left) Time series of annual-mean net Kuroshio transport [Sv] across the 137ºE section. (right) The Morlet wavelet transform coefficient for the normalized annual-mean net Kuroshio transport time series. Shading indicates an amplitude of the real part of the wavelet coefficient. The solid and dashed line represents that the local wavelet spectra defined as the square of the absolute wavelet transform coefficient are at a 10% and 20% significance level, respectively. The significance level is evaluated using Monte Carlo simulation based on a red noise model for the observed lag-1 correlation coefficient using a 10000-point surrogate time series. The curved line represents a cone of influence

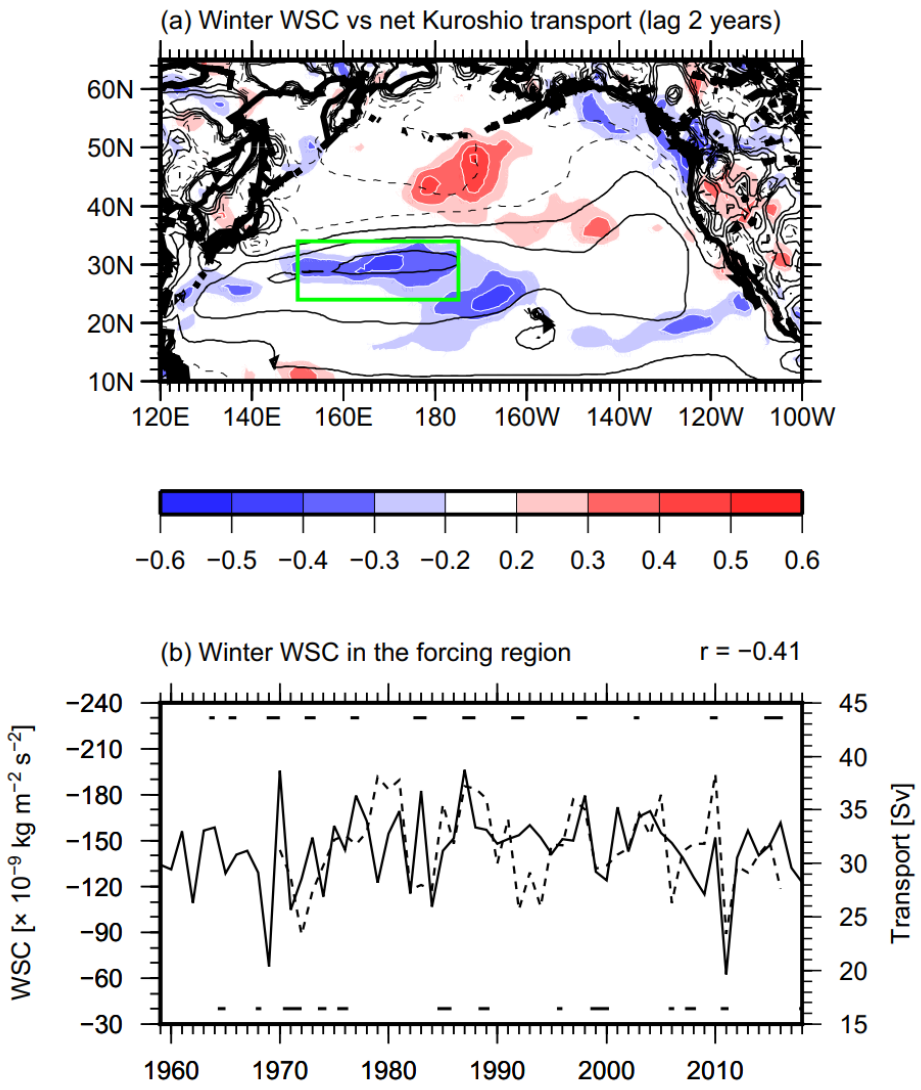

Figure 4.6

(a) Distribution of correlation coefficients between the annual-mean net Kuroshio transport and winter WSC with a lead lag of 2 years (i.e., WSC leads the net Kuroshio transport by 2 years). Contour denotes winter WSC climatology (1959–2018) with intervals of 90 × 10^{-9} kg m^{-2} s^{-2} (solid and dashed contours represent negative and positive values, repectively). The green rectangle indicates the forcing region (24–34ºN, 150ºE–175ºW). (b) Time series of winter WSC [× 10^{-9} kg m^{-2} s^{-2}] averaged in the forcing region. The dashed line shows the annual-mean net Kuroshio transport [Sv] forward by 2 years. The value on the right corner of the panel indicates the correlation coefficient (r) between the two time series. Bars at top (bottom) of the panel mean periods of El Nino (La Nina) defined by the JMA

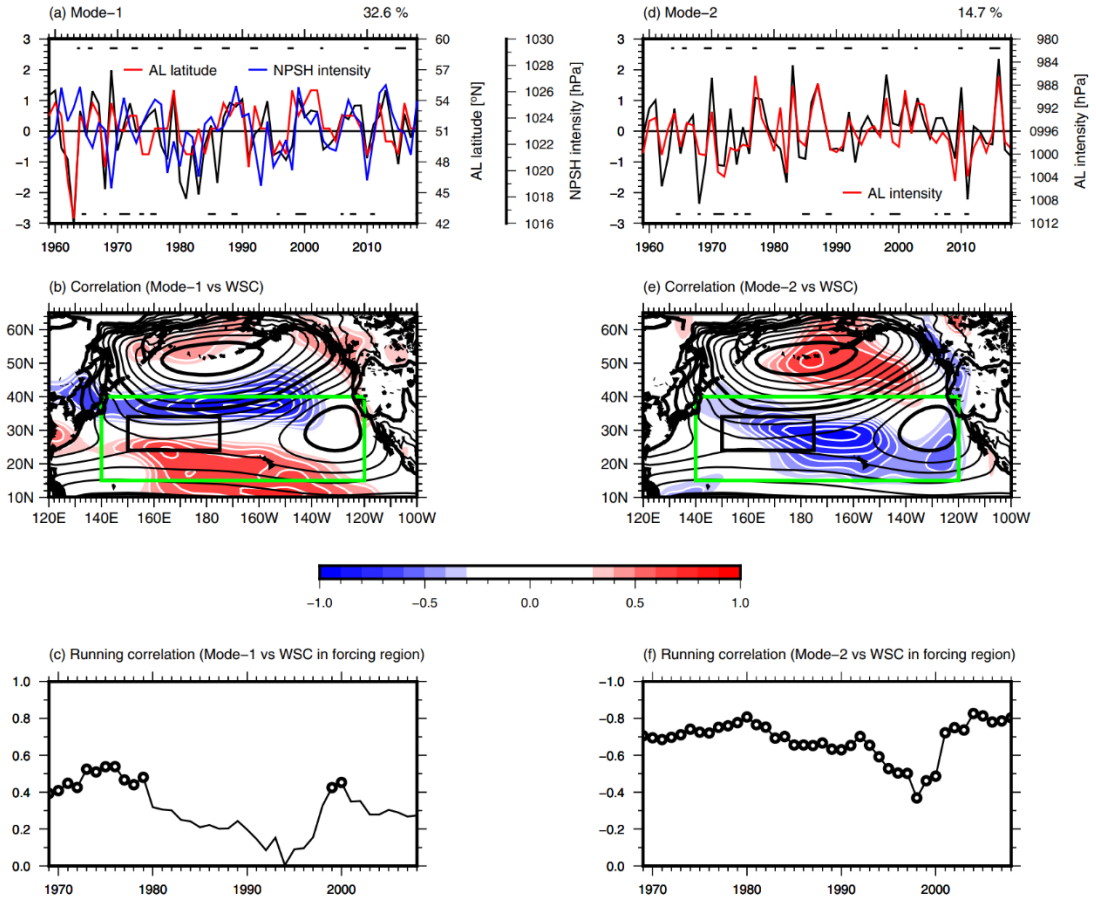

Figure 4.7

(a) Time coefficient (black line) of the first EOF mode extracted for winter WSC in the subtropical North Pacific (15–40ºN, 140ºE–120ºW, green rectangle in (b)) with the percentage of explained variance over the panel. The red and blue lines indicate the latitudinal position of the AL [ºN] and the NPSH intensity [hPa], respectively. Bars at top (bottom) of the panel mean periods of El Nino (La Nina) defined by the JMA. (b) Distribution of correlation coefficients between the time coefficient of the first EOF mode and winter WSC field (shading). Black contour represents the winter SLP climatology (1959–2018) (contour interval is 2 hPa with thick contours of 1000, 1010, and 1020 hPa). The Black rectangle shows the forcing region displayed in Figure 4.6a. (c) Time series obtained by running correlation analysis of winter WSC in the forcing region vs. first EOF mode (black line in (a)), using a window of 21 years. The correlation coefficient for a given year is calculated, for instance, the value at 2000 means a correlation coefficient for 1990–2010. Open circles represent significant values exceeding a 10% significance level. (d), (e), (f) Same as (a), (b), and (c), but for the second EOF mode. The red line in (d) indicates the intensity of the AL [hPa]

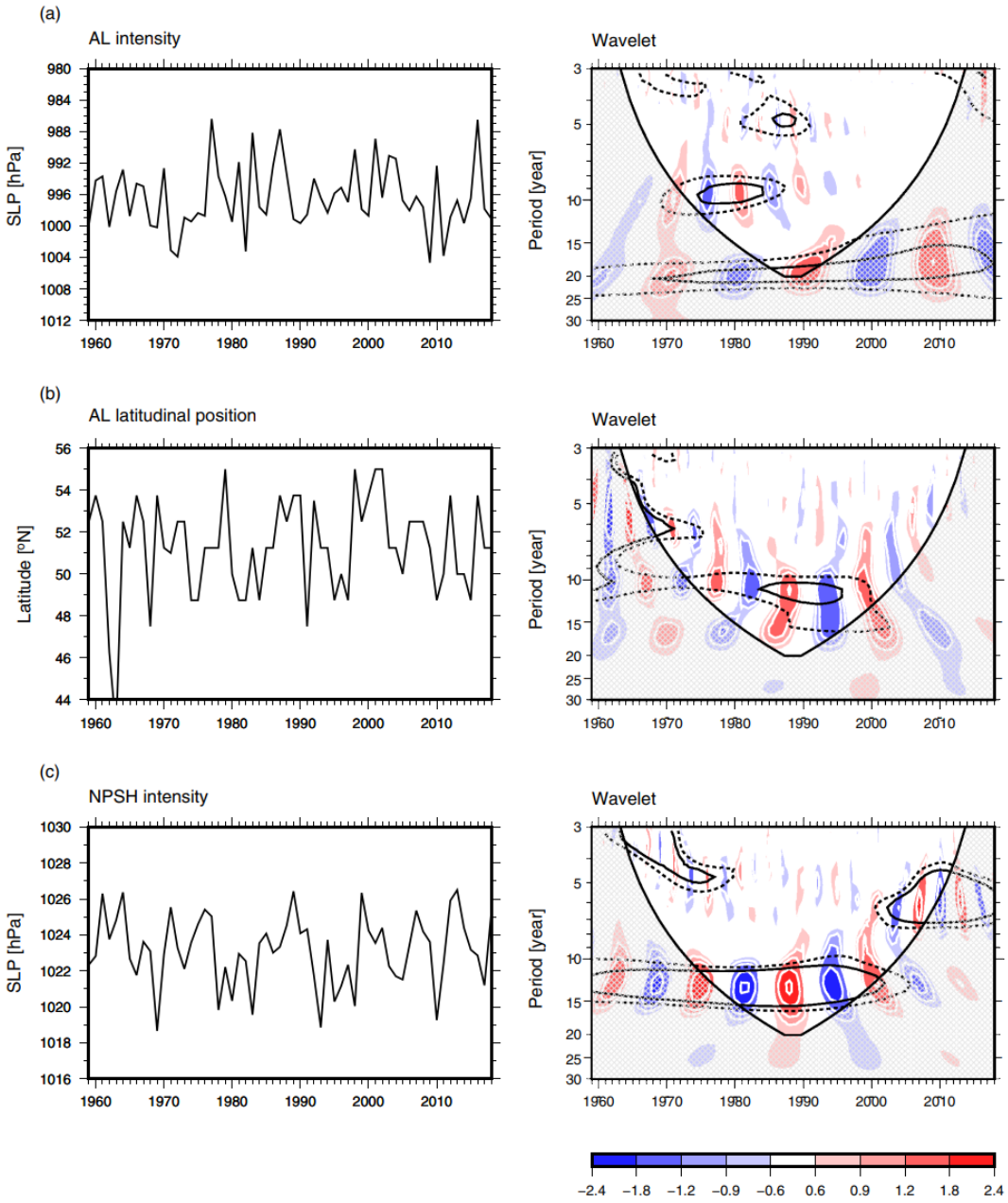

Figure 4.8

Same as Figure 4.5, but for the AL intensity [hPa] for (a), for the AL latitude [ºN] for (b), and for the NPSH intensity [hPa] for (c)

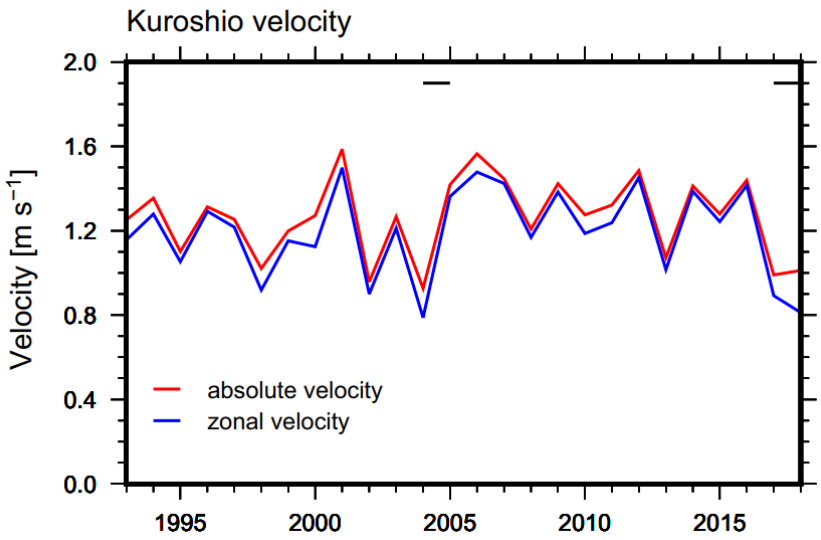

Figure 4.9

Satellite-derived annual mean Kuroshio velocity [m s^{-1}] at 137ºE. Red and blue lines indicate absolute and zonal Kuroshio velocity, respectively. The Kuroshio velocity is defined as the maximum velocity at 137ºE. Annual mean values are calculated by averaging the velocity data in January and July as well as in the case of 137ºE repeat observations. Horizontal bars at top of the panel represent periods of the Kuroshio large meander events.

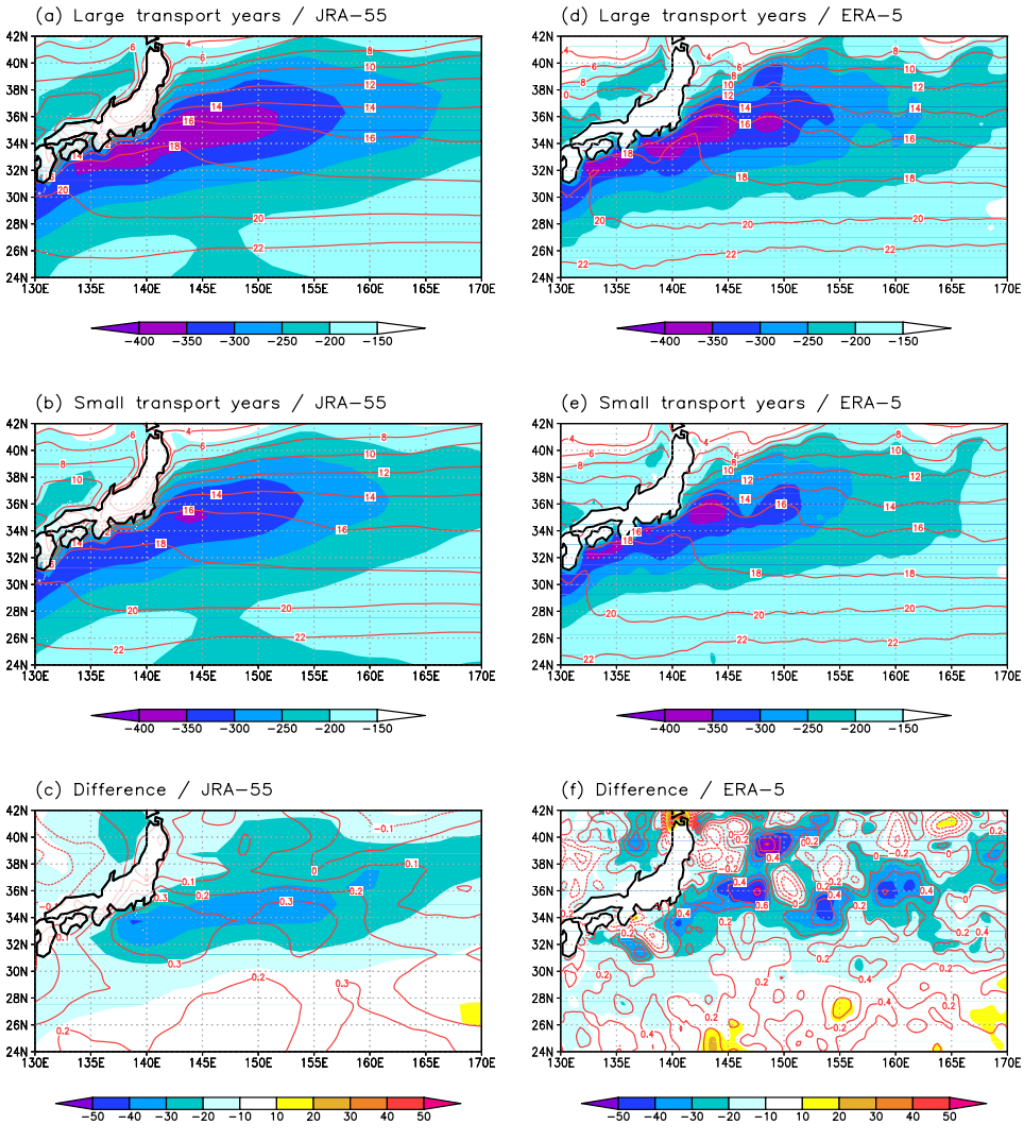

Figure 4.10

Late-winter SST [℃] (contour) and turbulent heat flux (a sum of latent and sensible heat fluxes) [W m^{-2}] (color) from JRA-55 averaged for the following years of (a) large and (b) small net Kuroshio transport years. Contour interval is 2 ℃. Upward heat flux is displayed as negative values. The large (small) transport years are determined as years when the annual-mean net Kuroshio transport is larger (smaller) than the average +0.7 (–0.7) standard deviation. SST in the JRA-55 is based on Centennial In Situ Observation-based Estimates of the Variability of SSTs and Marine Meteorological Variables (COBE-SST; Ishii et al., 2005). (c) Difference between (a) and (b) with a contour interval of 0.1℃. (d), (e), (f) Same as (a), (b), and (c) but SST and turbulent heat flux from ERA5.

Chapter 5

Cold- versus warm-season-forced variability of the Kuroshio and North Pacific subtropical mode water

5.1 Introduction

Temporal changes in atmospheric conditions such as sea surface winds, surface air temperature, and surface air humidity result in upper ocean variability through modulation of momentum and heat exchanges between atmosphere and ocean. In the North Pacific, atmospheric fields largely differ between cold and warm seasons. In a cold season, the Aleutian Low (AL) in the northern North Pacific becomes dominant, resulting in strong sea surface winds and then intense sea surface cooling (e.g., Trenberth and Hurrell, 1994). On the other hand, in a warm season, the North Pacific subtropical high (NPSH) centered at the eastern North Pacific covers the North Pacific widely, being relatively calm situations.

In the western North Pacific subtropical gyre, the Kuroshio flows poleward as the western boundary current, and North Pacific subtropical mode water (STMW; Masuzawa, 1969; see a review paper of Oka and Qiu, 2012) originated from deep winter mixed layer south of the Kuroshio Extension (KE) is distributed widely (Figure 5.1). Since the Kuroshio transports northward large amounts of seawater with heat and STMW has huge volume in upper ocean, they are considered as keys to understand 3-dimensional temperature/salinity (*T*/*S*) distributions in the western North Pacific subtropical gyre. Many authors have examined temporal variations of Kuroshio transport (e.g., Qiu and Joyce, 1992; Sugimoto et al., 2010; Chapter 4) and STMW distribution/temperature (e.g., Qiu and Chen, 2006; Oka et al., 2019). On the Kuroshio transport, influences of atmospheric forcing in a cold season have been well discussed (e.g., Deser et al., 1999; Yasuda and Kitamura, 2003). It has been pointed out that wind stress curl (WSC) variations in the central North Pacific associated with AL activities (e.g., Sugimoto and Hanawa, 2009; Chapter 4) and with NPSH variations (Chapter 4) have significant impacts on Kuroshio transport through oceanic baroclinic responses. On STMW, many studies revealed that sea surface cooling in a cold season is important factor for STMW formation (e.g., Suga and Hanawa, 1995a; Yasuda and Hanawa, 1999). Variations of wind stress fields in a cold season associated with AL activities also influence STMW formation by modulating KE path states (Qiu and Chen, 2006; Oka et al., 2019) and upper ocean stratification (Sugimoto and Kako, 2016). STMW temperature is determined by a combination of sea surface cooling (Suga and Hanawa, 1995a)

and entrainment of lower cold water into the mixed layer associated with mixed layer deepening (Sugimoto and Kako, 2016) in a cold season. Impacts of warm season atmospheric forcing on the Kuroshio and STMW have been also discussed. Akitomo et al. (1997) implied influences of warm season atmospheric forcing on Kuroshio transport by showing that Kuroshio transport fluctuates in response to annual-mean WSC variations over the North Pacific. Kako and Kubota (2007) pointed out that in 2005, sea surface heating in a warm season formed anomalously strong surface ocean stratification in the northwestern North Pacific subtropical gyre and inhibited the deepening of mixed layer in the following winter (i.e., STMW formation).

Due to strong sea surface winds and its-related intense surface cooling in a cold season, many authors have tended to attribute Kuroshio and STMW variability to atmospheric forcing in a cold season. However, it has been unclear whether or not atmospheric forcing in a warm season affects their variability. It remains possible that WSC variations associated with NPSH variations in a warm season influence Kuroshio transport and sea surface heating in a warm season affects STMW formation/temperature through modulation of preexisting upper ocean conditions. In this study, to obtain a perspective on a relationship between upper ocean variability and atmospheric variations, we investigate which season is responsible for the variability of Kuroshio transport and STMW distribution/temperature by performing numerical experiments with an eddy-resolving ocean general circulation model.

5.2 Model experiment and observational data

5.2.1 Model experiment

We perform numerical simulations with the North Pacific model (NP model; Sakamoto et al., 2019; Nakano et al., 2021) developed in the Japan Meteorological Agency (JMA)/Meteorological Research Institute (MRI). This model is based on MRI Community Ocean Model (MRI.COM; Tsujino et al., 2017), which is one of the standard ocean general circulation models in the international intercomparison project (OMIP2; Tsujino et al., 2020). The MRI.COM solves primitive equations under Boussinesq and hydrostatic approximations, and adopts a vertically re-scaled height coordinate system in which sea level undulations are reflected throughout the water column (Adcroft and Campin, 2004). The domain of the NP model is 15ºS–63ºN and 99ºE–75ºW (Figure 5.2). The horizontal resolution is 1/11º (longitude) × 1/10º (latitude). There are 60 vertical levels, and the layer thickness becomes larger with a depth from 2 m at the top layer to 700 m for the lowest layer. The NP model is

nested in a global ocean model with a horizontal resolution of 1º (longitude) × 1/2º (latitude) (GONDOLA_100; Urakawa et al., 2020) using a 2-way nesting method. The configuration of the NP model is the same as that of Sakamoto et al. (2019) and Nakano et al. (2021).

The atmospheric forcing used in this study (surface shortwave and longwave radiation fluxes, zonal and meridional wind speed at 10 m height, sea level pressure, precipitation, and air temperature and specific humidity at 10 m height) is 3-hourly JRA55-do dataset (Tsujino et al., 2018). Surface wind stress, latent and sensible heat fluxes, and evaporation are calculated using bulk formula (Large and Yeager, 2004, 2009). The initial conditions are created by driving GONDOLA_100 from World Ocean Atlas 2013 climatology (Levitus et al., 2014) with the JRA55-do dataset (1959–2013) repeatedly for 5 cycles: the restart at 00UTC on 1 January 1978 at 5th cycle is used as the initial conditions. The period of model experiments is 36 years during 1978–2013 (CTRL run).

To examine influences of the atmospheric forcings in cold and warm seasons on Kuroshio transport and STMW distribution/temperature, we conduct two sets of experiments by imposing different atmospheric conditions as summarized in Table 5.1. Here, cold and warm seasons are defined as October–March and April–September, respectively. The first experiment (COLD run) is conducted with raw 3-hourly JRA55-do forcing during a cold season and with 3-hourly climatological forcing during a warm season (30-year average for 1981–2010). The second experiment (WARM run) is performed in a similar manner as COLD run, with raw JRA55-do forcing in a warm season and with climatological forcing in a cold season.

5.2.2 Observational data

To validate model results, we use net Kuroshio transport timeseries calculated from optimally-interpolated (OI) *T*/*S* grided dataset of a repeated hydrographic section along 137ºE maintained by the JMA. The 137ºE OI dataset is constructed from *T*/*S* profiles taken by a reversing thermometer, Nansen bottles, conductivity-temperature-depth (CTD) profiler with Niskin bottles, expendable bathythermographs (XBT), expendable CTD (XCTD), and digital bathythermograph (DBT). A horizontal interval of grid points is 1/3º for 31–34ºN, 1/2º for 30–31ºN, and 1º for 3–30ºN (see Figure 5.1), and a vertical interval is 1 dbar. Winter (mainly January) and summer (mainly July–August) cruise data are available since 1967 and 1972, respectively. The OI dataset is available from JMA website (http://www.data.jma.go.jp/gmd/kaiyou/db/mar_env/results/OI/137E_OI_e.html). See Chapter 4 for details of this dataset and calculation of net Kuroshio transport.

We also use satellite-derived daily sea surface height (SSH) and surface current velocity data from Copernicus Marine Environment Monitoring Service (https://marine.copernicus.eu/). The horizontal resolution of these data is 1/4º (longitude) × 1/4º (latitude). These SSH and surface current velocity data are available from 1993.

5.3 Results

5.3.1 Reproducibility of the NP model

The NP model well reproduces winter mixed layer and water masses including STMW (Nakano et al., 2021). Here we specifically check reproducibility of the Kuroshio and KE in the NP model. Generally, the realistic simulation of the Kuroshio and KE requires the high-resolution settings (e.g., Liu et al., 2016; Kiss et al., 2020). The CTRL run successfully reproduces spatial distributions of mean SSH and surface current velocity in the northwestern North Pacific subtropical gyre (Figures 5.3a and 5.3b): the mean position and current speed of the Kuroshio, KE, and Kuroshio recirculation south of Japan are similar between satellite measurements and CTRL run. From the simulations, we calculate net Kuroshio transport across 137ºE; the reason why we select the longitudinal position of 137ºE is because long-term Kuroshio transport observations exist there and we can compare simulation results with the observation. The Kuroshio south of Japan is accompanied by two westward flows (see Figure 5.1): one is cold-core eddy transport north of the Kuroshio and the other is the Kuroshio recirculation, i.e., Kuroshio counter current (KCC), south of the Kuroshio. In this study, we calculate annual-mean transports by the cold-core eddy, Kuroshio, and KCC following a method of Sugimoto et al. (2010): northern and southern boundaries of the cold-core eddy, Kuroshio, and KCC are determined based on a SSH distribution (Figure 5.4), and then their transports are calculated by vertical and meridional integration of annual-mean zonal current velocity from the sea surface to 1000 dbar depth within each region. We define net Kuroshio transport as a sum of cold-core eddy transport, Kuroshio transport, and KCC transport. The net Kuroshio transport across 137ºE in CTRL run exhibits a decadal-scale variation with positive peaks around 1980, 1990, 2004, and 2011 and negative peaks around 1985, 1996, and 2008 (Figure 5.3c). Its temporal behavior resembles that from observations: the positive and negative peaks in the simulation are consistent with the observational result except for early 2000s. The observed and modeled net Kuroshio transports have similar amplitudes and almost the same average values.

5.3.2 Kuroshio transport

Based on CTRL run, we examine causes of the net Kuroshio transport variation focusing on a relationship to WSC variations over the North Pacific. In this study, we use annual-mean WSC to take both cold and warm seasons into account. A lag-correlation analysis shows that the net Kuroshio transport responds to the WSC variations in the central North Pacific (32–37ºN, 160ºE–170ºW; hereafter, forcing region) with a 2-year lag (Figure 5.5). Past works concluded that WSC variations in the central North Pacific cause net Kuroshio transport variations through westward propagation of oceanic Rossby waves (e.g., Sugimoto et al., 2010). In the NP model, the propagation speed of baroclinic Rossby waves is estimated as about 2.5–3.5 cm s^{-1} at 30–35ºN (Nakano et al., 2021), which means oceanic Rossby waves reach 137ºE from around 155–172ºE with 2–3 years. That is, the obtained lag of the net Kuroshio transport to the WSC in the forcing region in this study (i.e., 2 years) is explained by the oceanic Rossby wave propagation. To provide evidence for oceanic Rossby waves, we plot a longitude-time diagram of SSH anomalies averaged for 30–35ºN where the Kuroshio and the forcing region are located (Figure 5.6). It is confirmed that most signals propagate westward from the formation region (i.e., forcing region), indicating oceanic Rossby waves.

The net Kuroshio transport in COLD run reproduces well that in CTRL run (correlation coefficient (r) = 0.75, exceeding a 10% significance level) (Figure 5.7). The net Kuroshio transport in COLD run fluctuates on a decadal timescale with almost the same amplitude as that of CTRL run. The transport significantly correlates to WSC in the central North Pacific with a lag of 2 years in COLD run (Figure 5.8), consistent with CTRL run. On the other hand, the net Kuroshio transport in WARM run exhibits a year-to-year variation rather than a decadal variation especially after 1990 (Figure 5.7). Its temporal behavior differs from the net Kuroshio transport variation in CTRL run (r = 0.35, non-significant), and is not related to WSC variations over the North Pacific with lags (see Figure 5.9). Westward propagations of oceanic Rossby waves from the central North Pacific are detectable in COLD run, but not in WARM run (Figure 5.10). In WARM run, oceanic Rossby waves are not generated in the central North Pacific and only small-scale SSH anomalies are detectable in the western region, which might represent the internal variability. These results mean that oceanic Rossby waves that affect the net Kuroshio transport are generated by atmospheric forcing in a cold season. In fact, the WSCs in CTRL and COLD runs have almost the same amplitude (about 15×10^{-9} kg m^{-2} s^{-2}) and are significantly correlated with each other (r = 0.88, exceeding a 10% significance level) (Figure 5.11). On the other hand, the WSC in WARM run is less variable (with the amplitude of 5 ×

10^{-9} kg m^{-2} s^{-2}) and not significantly correlated to that in CTRL run ($r = 0.32$). Our simulations indicate that the WSC variation in a cold season is a dominant driver for the net Kuroshio transport variation. This result is a robust evidence supporting past studies that have focused on cold-season atmospheric forcing as a cause of the net Kuroshio transport variation.

5.3.3 STMW distribution/temperature

STMW in the northwestern North Pacific subtropical gyre is characterized by vertically homogenous layer over the main thermocline and detected as low-potential vorticity (PV) water. Here, PV is calculated as,

$$\mathrm{PV} = -\frac{f}{\rho}\frac{\partial \sigma_\theta}{\partial z} \tag{5.1}$$

where f is the Coriolis parameter, ρ is the density of seawater, σ_θ is the potential density, and z is a vertical coordinate. The relative vorticity is ignored because the STMW distribution region is far from strong currents, near which the relative vorticity is comparable to the planetary vorticity. We firstly examine STMW properties in the NP model using CTRL run. Figure 5.12 displays a climatological meridional-vertical cross section of PV and potential temperature (θ) averaged in 140–150ºE in August after STMW subducts into the subsurface. Low-PV water representing STMW is centered at a depth of around 250 m with θ of 15–19 ℃ and σ_θ of 25.0–25.6 kg m^{-3}. This is consistent with observational results (e.g., Oka, 2009; Oka et al., 2011). In this study, we define STMW as regions north of 20ºN with PV < 1.5×10^{-10} m^{-1} s^{-1} and θ = 15–19 ℃. STMW core temperature is identified as θ at the PV minimum.

We investigate temporal variations of STMW formation focusing on mixed layer depth (MLD) in late winter. We define MLD as a depth at which σ_θ increases by 0.03 kg m^{-3} from its value at the sea surface (similar to Weller and Plueddemann, 1996) and late winter as March. Figure 5.13a shows a climatological distribution of late-winter MLD from CTRL run. The deepest mixed layer is found in the region south of the KE and located within the outcrop regions of the isopycnal surfaces corresponding to STMW (σ_θ = 25.0–25.6 kg m^{-3}). Based on this MLD distribution, we define the STMW formation region as 30–34ºN, 141–155ºE, consistent with observational results (see a review paper of Oka and Qiu, 2012). Figure 5.13b displays temporal variations of late-winter MLD in the STMW formation region. CTRL run simulates a decadal-scale MLD variation with positive peaks around 1984, 1994, and 2003, corresponding to observations (e.g., Qiu and Chen, 2006; Sugimoto and Kako, 2016). Previous studies pointed out that the late-winter MLD is controlled by two factors of net

heat flux (NHF) in winter and preexisting upper ocean stratification (e.g., Iwamaru et al., 2010; Sugimoto and Kako, 2016). It is suggested that the MLD is determined by the NHF before 1990, whereas strength of preexisting upper ocean stratification has large influences on the MLD after 1990. We compute winter (December–February) NHF and preexisting main thermocline depth (MTD), which is an indicator of preexisting upper ocean stratification, in the STMW formation region (Figure 5.14), and then examine their relationship to the late-winter MLD by performing a running correlation analysis with a window of 15 years (Figure 5.15). Here, we define MTD as a depth of 12 °C isotherm because it is located near the center of the main thermocline in the North Pacific subtropical gyre (see Figure 5.12), and use the MTD value in September as preexisting MTD. The running correlation analysis indicates that winter NHF has large influences on the MLD in the early and latter parts of the analysis period (~1993, 1997~), while preexisting MTD becomes important for the MLD towards the end of the analysis period (1995~). All years in the analysis period except for 1994 are included in at least one 15-year window in which winter NHF and/or preexisting MTD significantly correlates to the MLD.

The late-winter MLD in the STMW formation region in COLD run fluctuates on a decadal timescale (Figure 5.13b), the temporal behavior of which is consistent with that in CTRL run ($r = 0.84$, exceeding a 10% significance level). In COLD run, the NHF and MTD are also similarly simulated to NHF and MTD in CTRL run ($r = 0.96$ for NHF and $r = 0.56$ for MTD, exceeding a 10% significance level) (Figure 5.14). On the other hand, WARM run shows a small MLD variation (Figure 5.13b) and the temporal features are different from the MLD variation of CTRL run ($r = –0.23$, non-significant). In WARM run, winter NHF shows similar temporal variations to that of CTRL run ($r = 0.88$, exceeding a 10% significance level), but its amplitude is much smaller (Figure 5.14a). The preexisting MTD in WARM run fluctuates differently from that of CTRL run ($r = 0.30$, non-significant) (Figure 5.14b). It has been reported that the MTD variations in the North Pacific subtropical gyre are attributable to oceanic Rossby waves caused by WSC variations in the central North Pacific (Sugimoto and Kako, 2016). The poor reproducibility of the MTD variation in WARM run would result from the lack of westward propagation of oceanic Rossby waves (Figure 5.10) due to small WSC variations in the central North Pacific (Figure 5.11). These results indicate that late-winter MLD in the STMW formation region is dominantly determined by the atmospheric forcing in a cold season.

Next, we investigate STMW distribution. We calculate STMW area size from a mean meridional-vertical cross section of PV averaged in 140–150ºE in August after STMW subduction.

The STMW area size in CTRL run shows a decadal variation with positive peaks around 1984, 1994, and 2004 (Figure 5.16a), reflecting the decadal variation of late-winter MLD in the STMW formation region (i.e., STMW formation) (Figure 5.13b) ($r = 0.39$ for their raw timeseries as non-significant, but $r = 0.59$ for their low-pass-filtered timeseries by a 1-3-4-3-1 filter exceeding a 10% significance level). The decadal-scale STMW-area-size variation is also seen in COLD run ($r = 0.83$ with the STMW-area-size variation in CTRL run, exceeding a 10% significance level) (Figure 5.16a). On the other hand, a STMW-area-size variation in WARM run is much smaller compared with that in CTRL run, reflecting the small MLD variation. These results indicate that STMW distribution also strongly reflects the atmospheric forcing in a cold season.

We focus on STMW temperature. CTRL run shows that both the late-winter mixed layer temperature (MLT), defined as temperature at 10 m depth in March, in the STMW formation region (Figure 5.13c) and summertime STMW core temperature from a mean meridional-vertical cross section of θ averaged for 140–150ºE (Figure 5.16b) have decadal variations and positive trends (0.038 ℃ year^{-1} for MLT and 0.038 ℃ year^{-1} for STMW core temperature). These features are similar to observational results (e.g., Sugimoto and Kako, 2016; Sugimoto et al., 2017b; Oka et al., 2019). Since STMW core temperature originates from late-winter MLT in the STMW formation region (e.g., Hanawa and Kamada, 2001) and CTRL run reproduces this relationship ($r = 0.65$, exceeding a 10% significance level), we investigate the MLT variation. An observational study by Sugimoto et al. (2017b) suggested that the trend of surface warming around the Kuroshio region where STMW is formed is due to oceanic processes such as heat advection rather than surface heat flux. Consistently, CTRL run shows no significant trend in winter NHF in the STMW formation region (Figure 5.14a). The detrended late-winter MLT is negatively correlated with late-winter MLD ($r = –0.60$, exceeding a 10% significance level) and not correlated with winter NHF ($r = 0.29$, non-significant). This indicates that an entrainment of lower cold water into the mixed layer associated with mixed layer deepening in a cold season plays an important role for the MLT variation as suggested by Sugimoto and Kako (2016). Similar to CTRL run, both MLT and STMW core temperature in COLD run show decadal variations and warming (0.028 ℃ year^{-1} for MLT and 0.025 ℃ year^{-1} for STMW core temperature) (Figures 5.13c and 5.16b). A correlation coefficient between the detrended MLTs (STMW core temperatures) in CTRL and COLD runs is 0.84 (0.61), which exceeds a 10% significance level. On the other hand, WARM run does not fully reproduce the temporal features of the MLT and STMW core temperature in CTRL run: the positive trends are reproduced (0.030 ℃ year^{-1} for MLT and 0.037 ℃ year^{-1} for

STMW core temperature), but the decadal variations are not seen (Figures 5.13c and 5.16b). It is therefore suggested that atmospheric forcing in a cold season is crucial for the late-winter MLT in the STMW formation region and its-derived STMW core temperature.

5.4 Summary

Variability of upper oceanic structure has been considered to be attributable to atmospheric forcing in a cold season, but it has not been clarified whether or not atmospheric forcing in a warm season is also important for the upper ocean variability. To address this point, we performed sensitivity experiments to cold and warm season atmospheric forcings using an eddy-resolving ocean general circulation model which satisfactorily reproduces physical fields in the North Pacific.

Our simulations showed that net Kuroshio transport south of Japan is dominantly determined by atmospheric forcing in a cold season. Through westward propagation of oceanic Rossby waves, net Kuroshio transport responds to WSC variations in the central North Pacific which strongly reflect atmospheric conditions in a cold season. Distributions and temperature of STMW also mostly depend on atmospheric conditions in a cold season. Influences of preexisting upper ocean conditions attributable to atmospheric forcing in a warm season on STMW are relatively smaller.

Contribution of this study is to have demonstrated the importance of cold season atmospheric forcing for upper ocean variability in the North Pacific subtropical gyre. Our results suggest that relationships with cold season atmospheric variations are keys to obtain a perspective of large-scale upper ocean variability in the North Pacific subtropical gyre. On the basis of this study, future works would be able to further reveal the mechanism of the upper ocean variability in the North Pacific subtropical gyre. Our approach is also applicable in other subtropical oceans worldwide.

Table 5.1

List of the atmospheric forcings used in model experiments. Climatology means 30-year average for 1981–2010.

Experiment	Forcing
CTRL run	3–hourly raw data
COLD run	3–hourly raw data (OCT–MAR) and 3–hourly climatology (APR–SEP)
WARM run	3–hourly raw data (APR–SEP) and 3–hourly climatology (OCT–MAR)

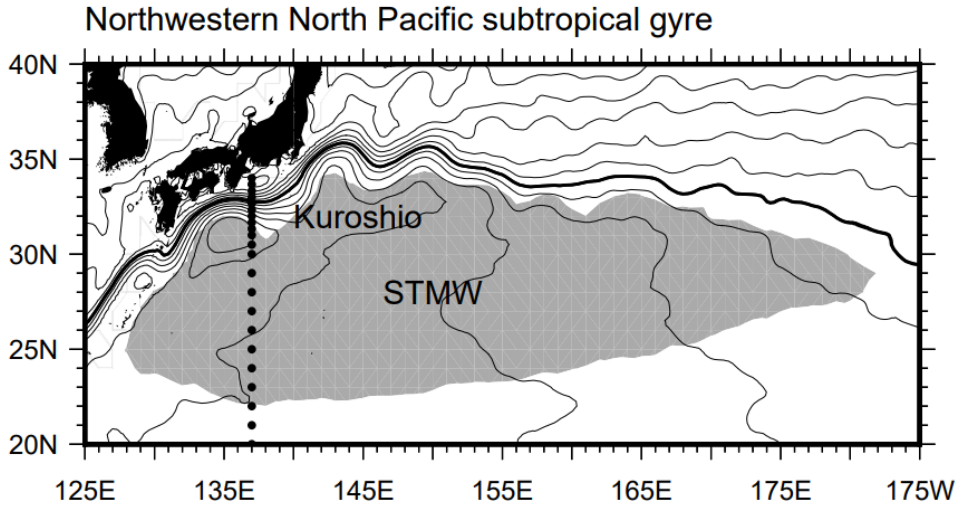

Figure 5.1

The Kuroshio and STMW in the northwestern North Pacific subtropical gyre. Contours mean sea surface height [cm] for 1993–2020 (10 cm interval) (see text for details of dataset). Thick line represents a 100 cm contour which locates near the Kuroshio axis south of Japan. The distribution region of STMW is schematically illustrated with gray shading based on Oka and Qiu (2012). Dots are drawn at grid points of optimally-interpolated gridded dataset of a repeated hydrographic section along 137ºE (see text for details).

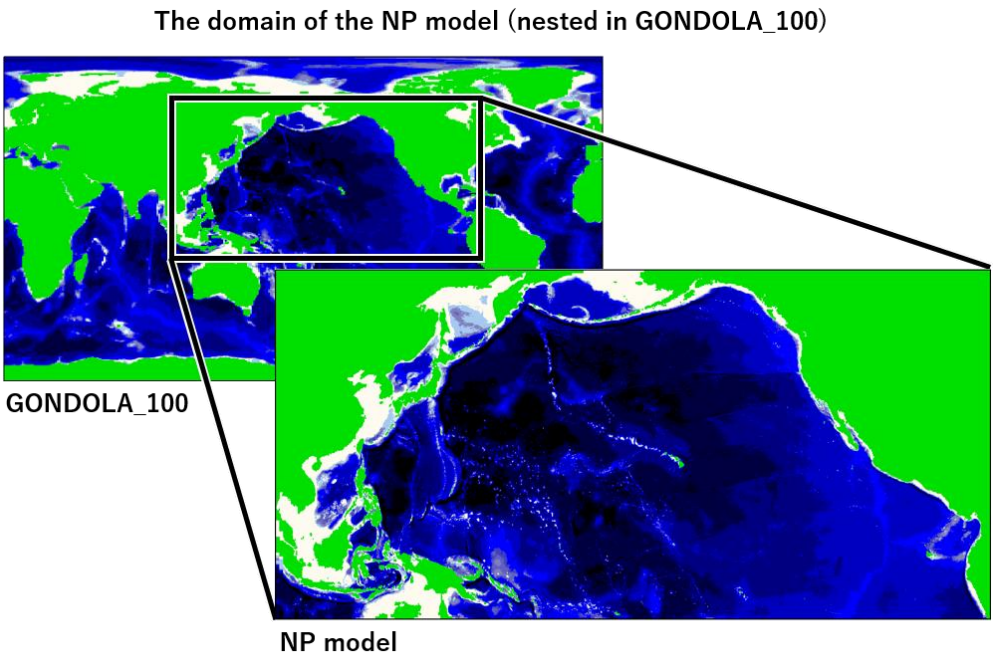

Figure 5.2

The domain of the NP model (lower-right panel; 15ºS–63ºN and 99ºE–75ºW). The NP model is nested in a global model GONDOLA_100 (upper-left panel; Urakawa et al., 2020) with a 2-way nesting method (see text for details).

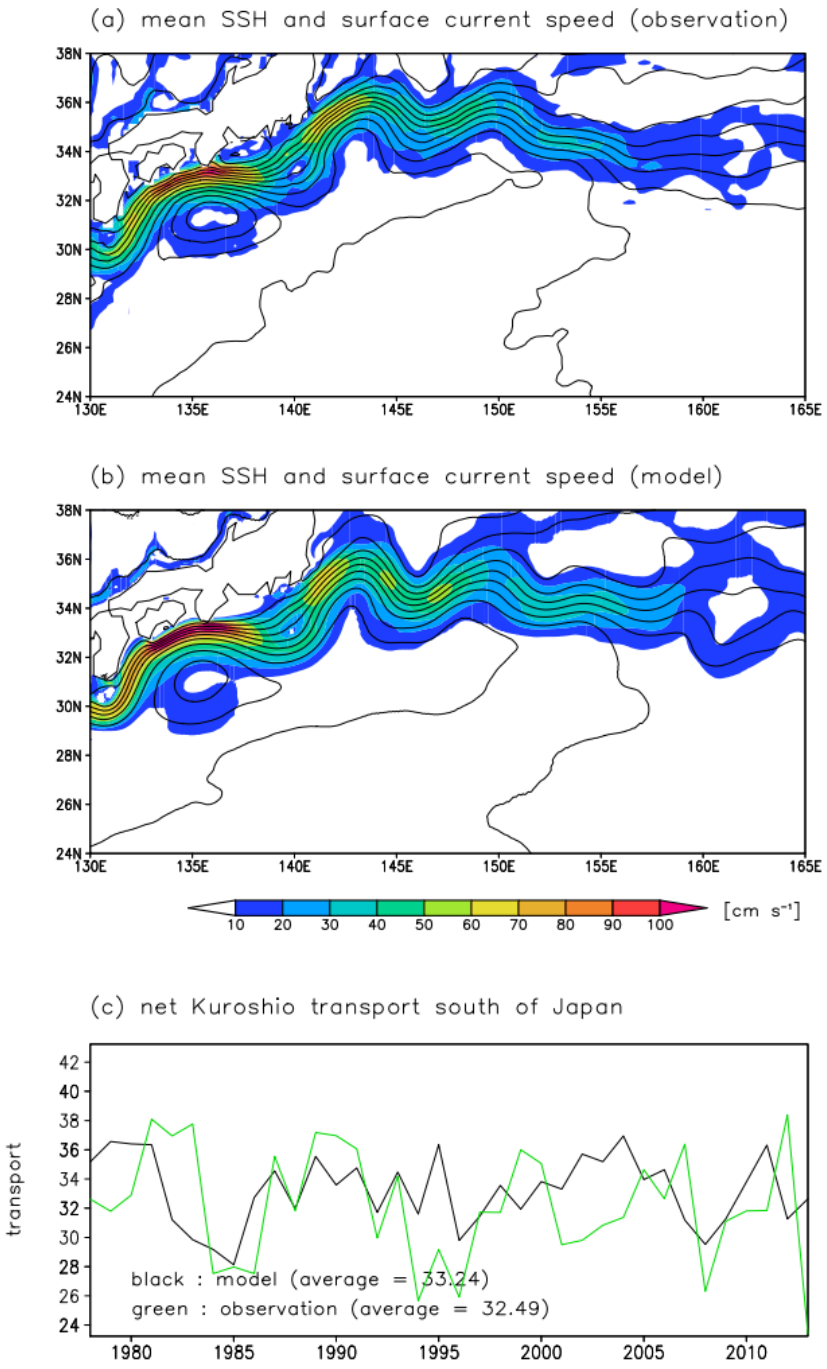

Figure 5.3

SSH [cm] (contour, 10 cm interval) and surface current speed [cm s^{-1}] (shading) from (a) satellite measurements and (b) CTRL run averaged for 1993–2013. (c) Net Kuroshio transport [Sv; 1 Sv = 10^6 m^3 s^{-1}] across 137ºE from hydrographic observations by the JMA (green) and CTRL run (black).

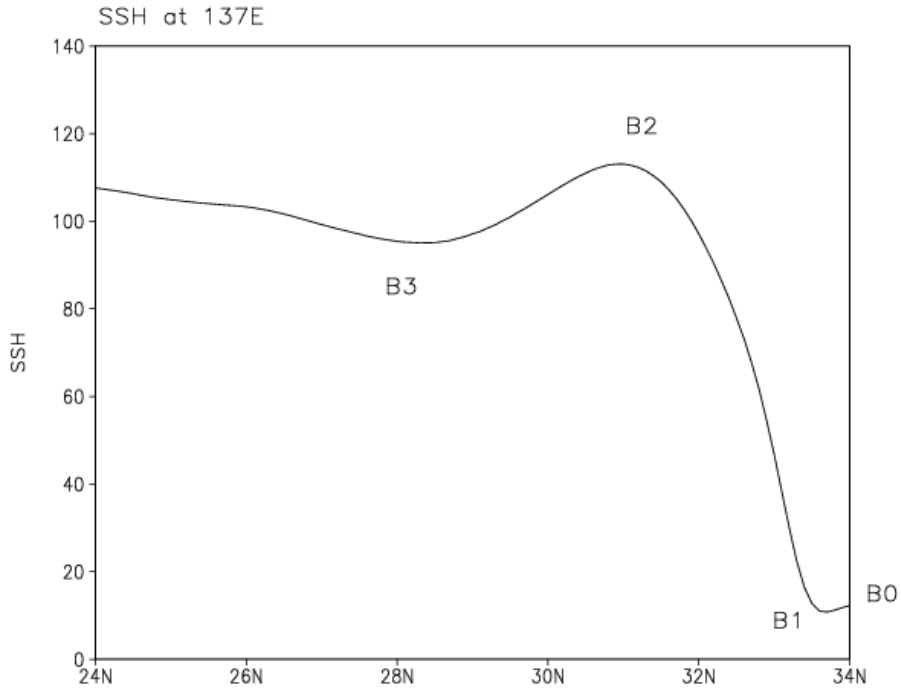

Figure 5.4

Schematic diagram of SSH [cm] along 137ºE. The regions of westward flow by the cold-core eddy, Kuroshio, and KCC are defined as regions between B0 and B1, between B1 and B2, and between B2 and B3, respectively.

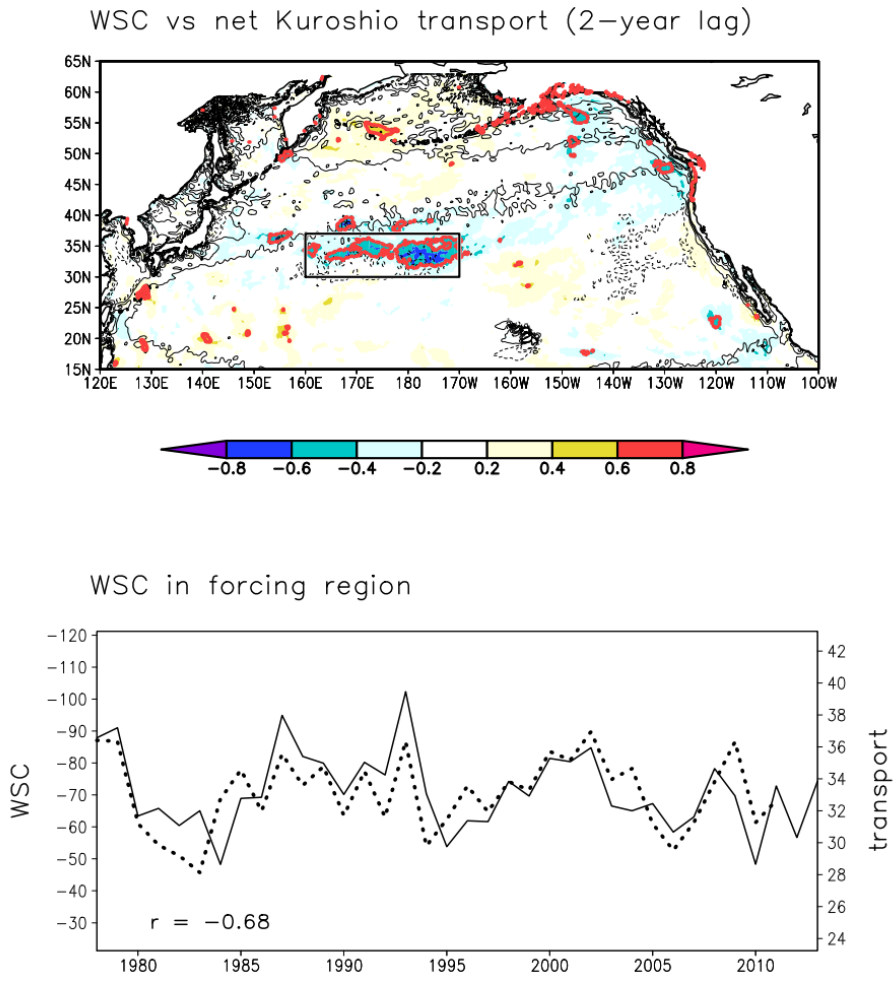

Figure 5.5

(Top) Correlation coefficients between net Kuroshio transport and WSC in CTRL run with a 2-year lag (WSC leads net Kuroshio transport). Red lines indicate the regions with correlation coefficients exceeding a 10% significance level. Contours denote the WSC climatology (1978–2013) with an interval of 90 × 10^{-9} kg m^{-2} s^{-2} (negative values are drawn by dotted contours). Rectangle indicates the forcing region (32–37ºN, 160ºE–170ºW). (Bottom) WSC [10^{-9} kg m^{-2} s^{-2}] (left axis) averaged in the forcing region in CTRL run. Dashed line indicates net Kuroshio transport [Sv] (right axis) in CTRL run forwarded by 2 years. The number in the lower-left corner means a correlation coefficient between the two timeseries in the panel.

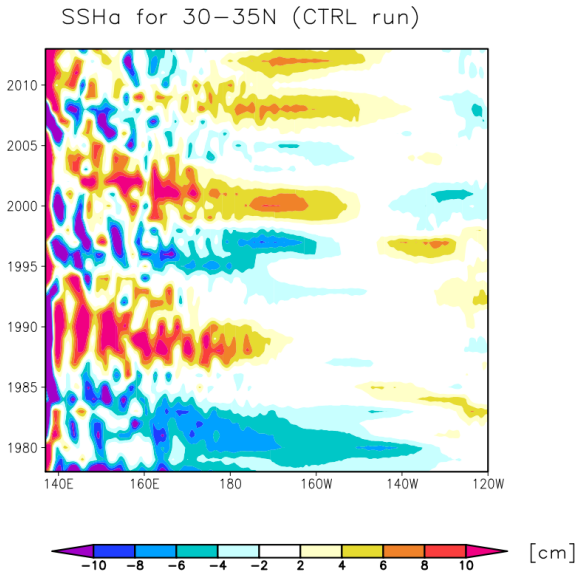

Figure 5.6

Longitude-time diagram of SSH anomalies [cm] averaged for 30–35ºN from CTRL run.

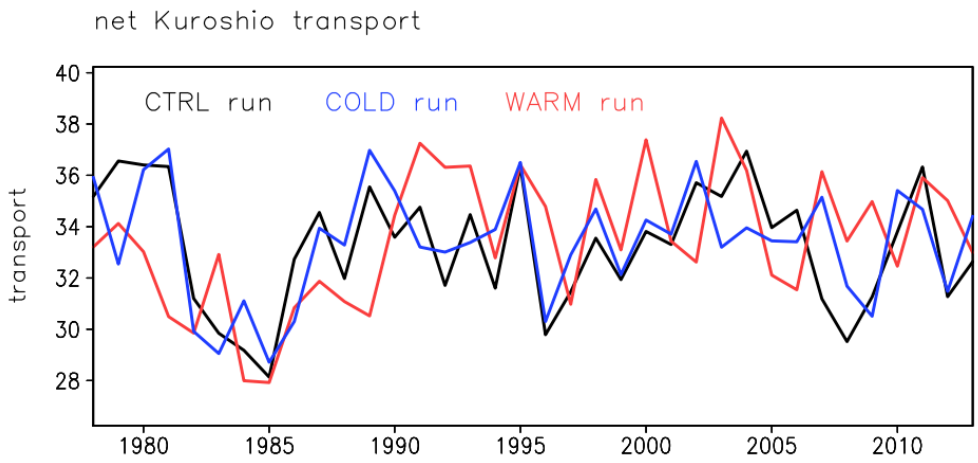

Figure 5.7

Net Kuroshio transport [Sv] across 137ºE in CTRL (black), COLD (blue), and WARM (red) runs.

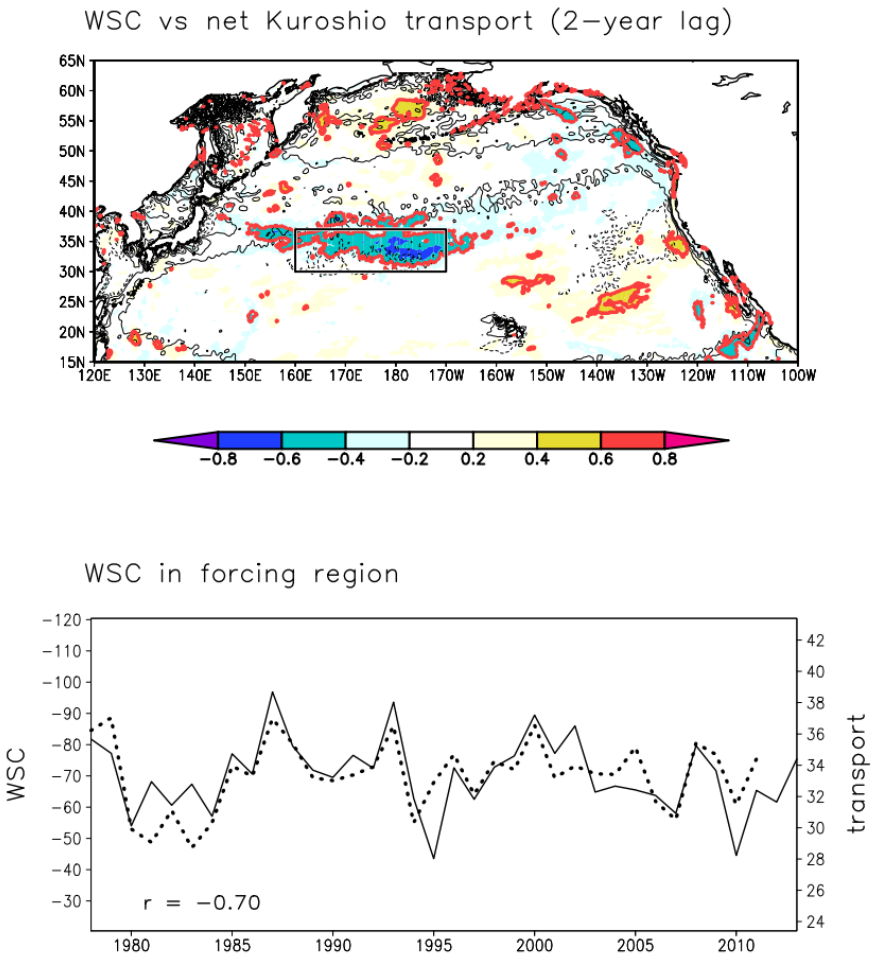

Figure 5.8

Same as Figure 5.5, but for COLD run.

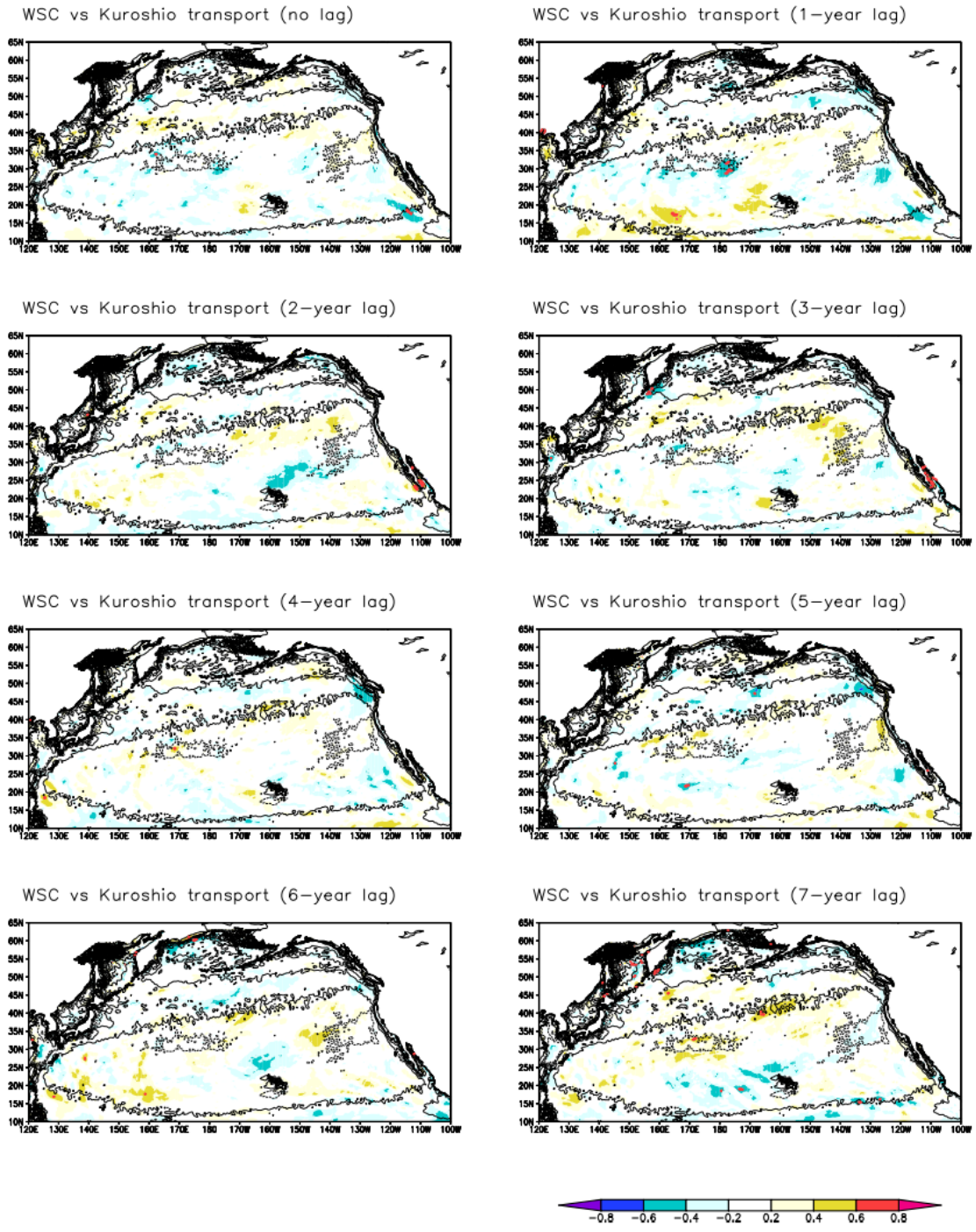

Figure 5.9

Correlation coefficients between net Kuroshio transport and WSC in WARM run with 0–7-year lags (WSC leads net Kuroshio transport). Red lines indicate the regions with correlation coefficients exceeding a 10% significance level. Contours denote the WSC climatology (1978–2013) with an interval of 90×10^{-9} kg m^{-2} s^{-2} (negative values are drawn by dotted contours).

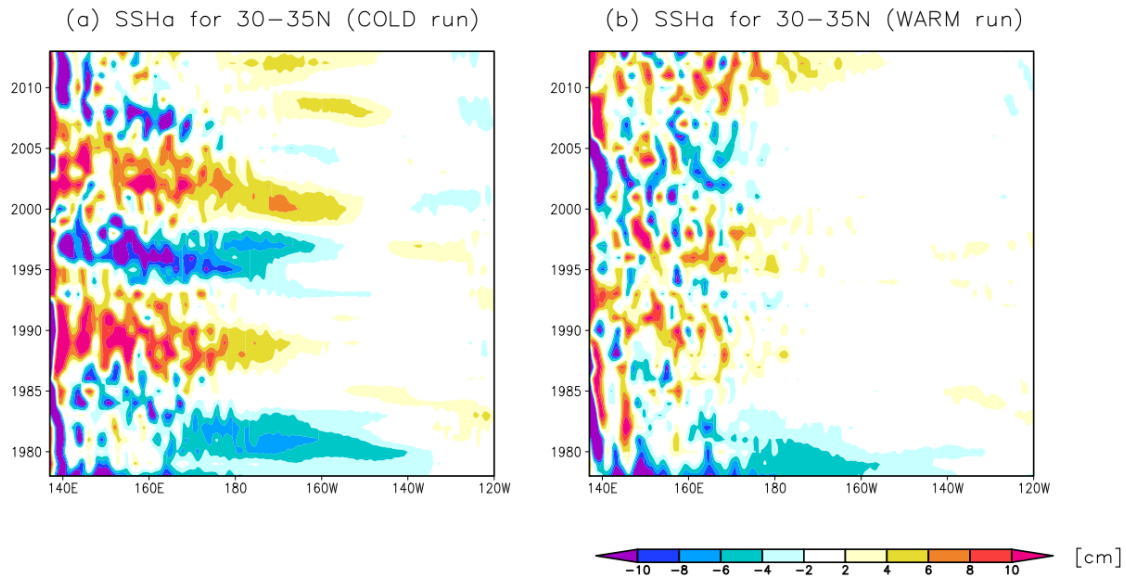

Figure 5.10

Same as Figure 5.6, but for (a) COLD and (b) WARM runs.

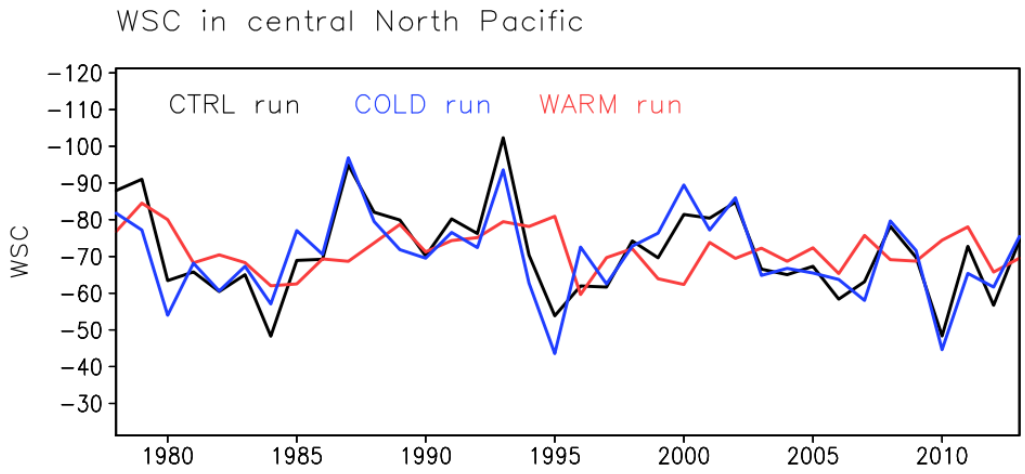

Figure 5.11

WSC [10^{-9} kg m^{-2} s^{-2}] averaged in the central North Pacific (32–37ºN, 160ºE–170ºW) from CTRL (black), COLD (blue), and WARM (red) runs.

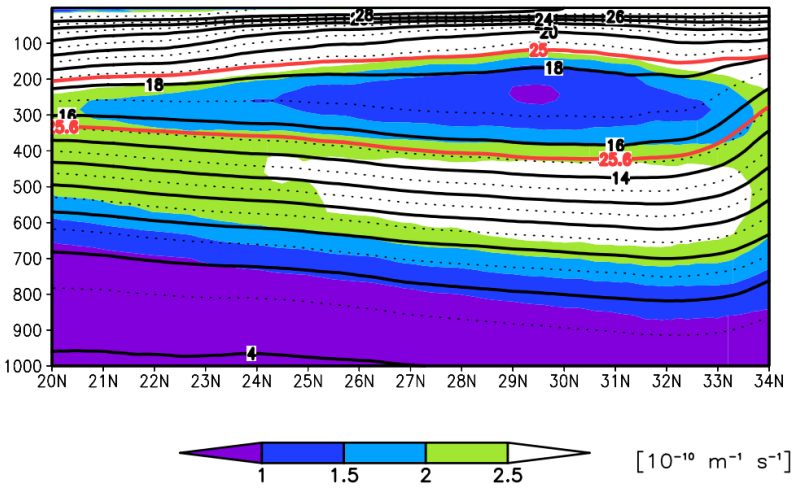

Figure 5.12

Mean meridional-vertical cross section of PV [10^{-10} m^{-1} s^{-1}] (shading) and θ [°C] (contour) in August for 1978–2013 averaged in 140–150ºE from CTRL run. Red lines indicate isopycnal surfaces of σ_θ = 25.0 and 25.6 kg m^{-3}.

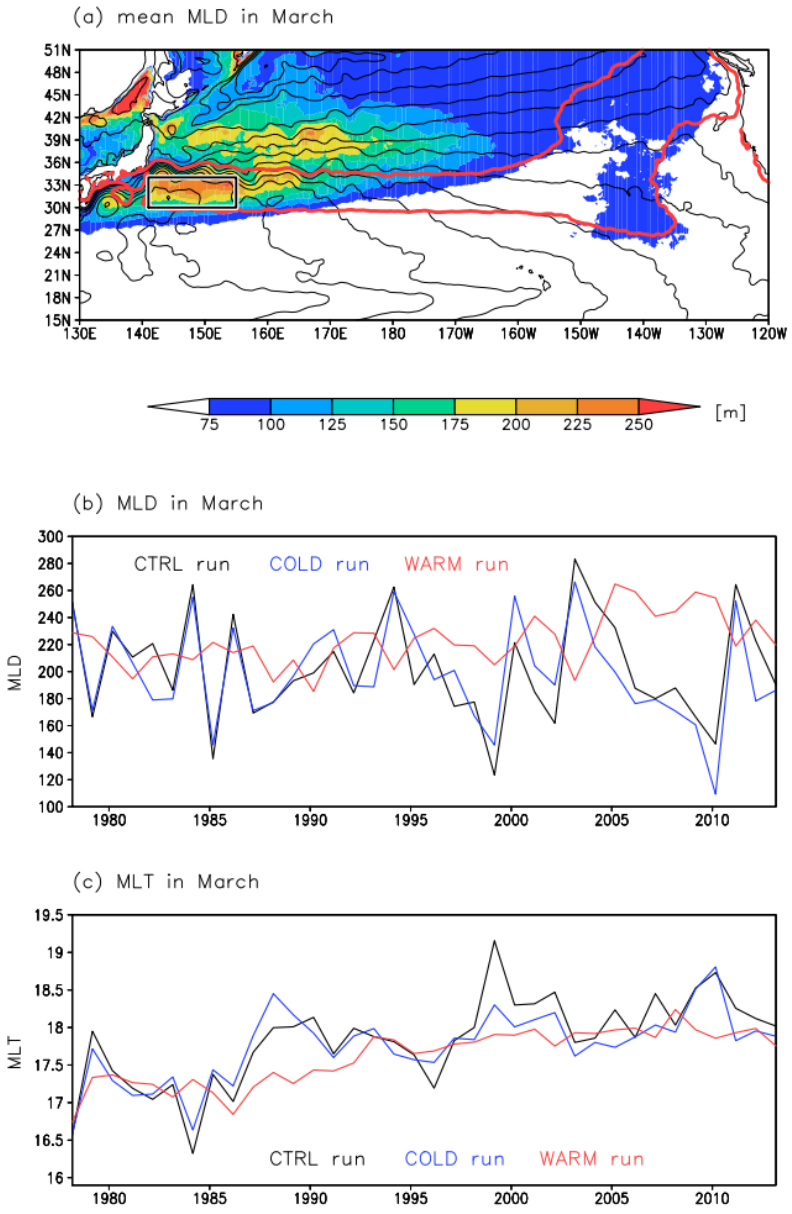

Figure 5.13

(a) Distribution of MLD [m] (shading) and SSH [cm] (contour, 10 cm interval) in March averaged for 1978–2013 from CTRL run. Rectangle indicates the STMW formation region (30–34ºN, 141–155ºE). Red lines indicate the mean position of the isopycnal outcrop regions of σ_θ = 25.0 and 25.6 kg m^{-3} in March for 1978–2013. (b) Timeseries of MLD in March in the STMW formation region. Black, blue, and red lines represent CTRL, COLD, and WARM runs, respectively. (c) Same as (b), but for MLT in March in the STMW formation region.

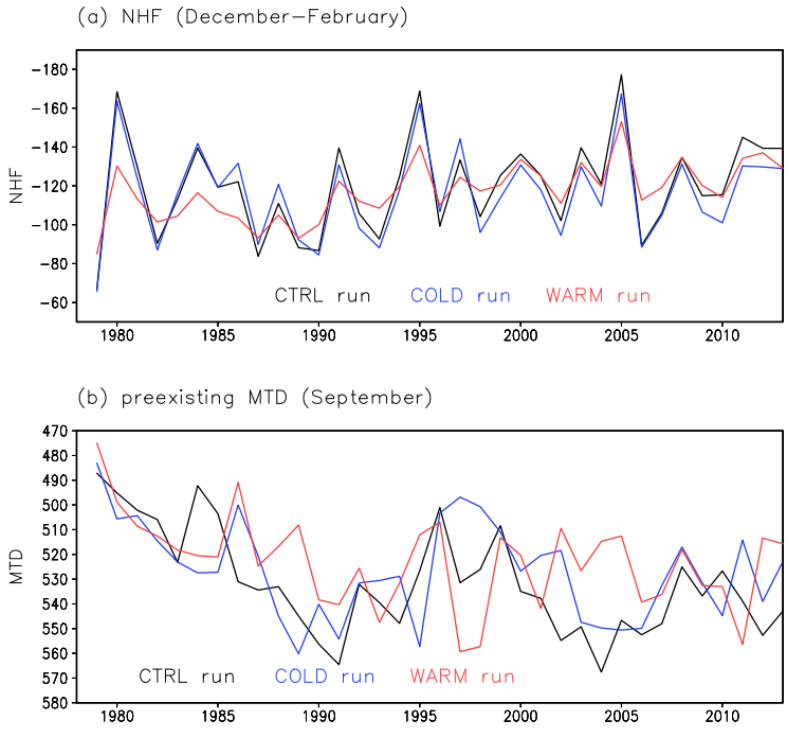

Figure 5.14

Timeseries of (a) mean NHF (negative value means upward) [W m^{-2}] for December–February and (b) MTD [m] in the preceding warm season (September) averaged in the STMW formation region. Black, blue, and red lines indicate CTRL, COLD, and WARM runs, respectively. MTD in the preceding warm season is plotted as the following year, e.g., a value in 1999 September is plotted as the year 2000.

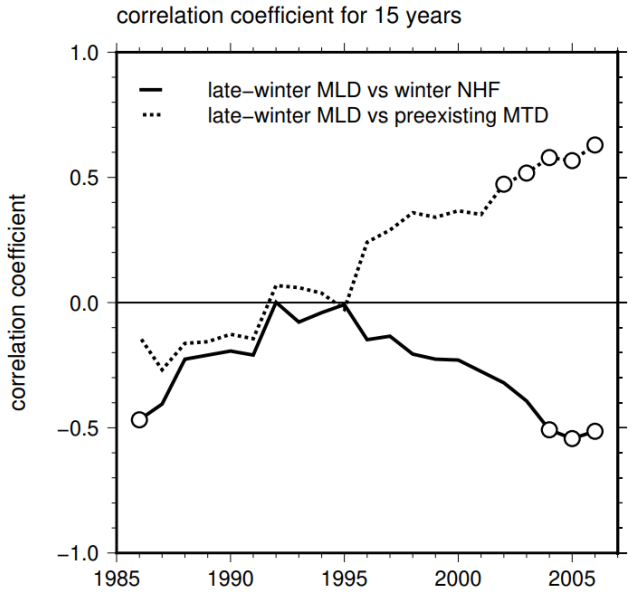

Figure 5.15

Timeseries obtained by a running correlation analysis of late-winter MLD vs winter NHF (negative value means upward) (solid line) and MTD in the preceding warm season (September) (dashed line) in the STMW formation region from CTRL run, using a window of 15 years. The correlation coefficient for a given year is calculated, for instance, the value at 1995 means a correlation coefficient for 1988–2002. Open circles represent significant values exceeding a 10% significance level.

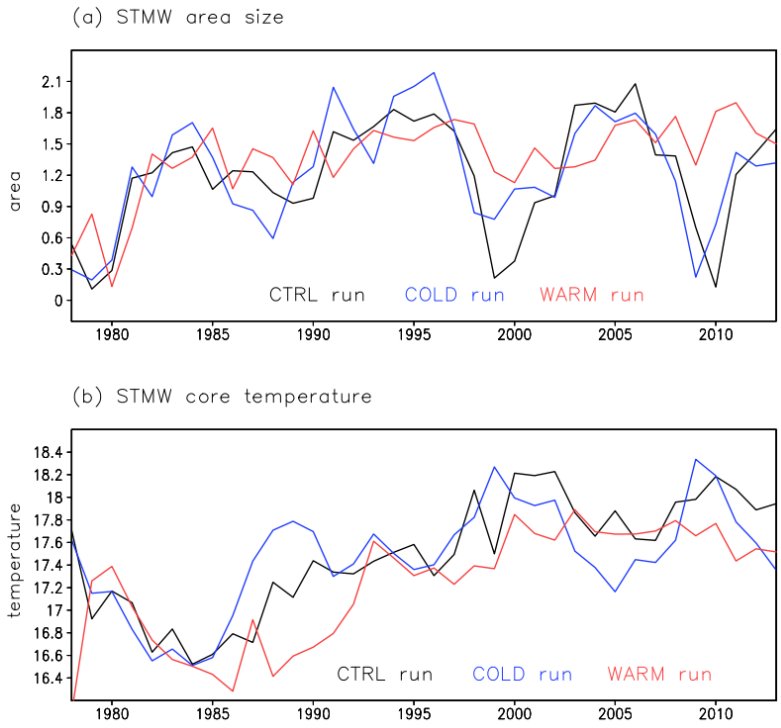

Figure 5.16

Timeseries of (a) STMW area size [10^8 m^2] and (b) STMW core temperature [°C] from a meridional-vertical cross section in August averaged in 140–150ºE. Black, blue, and red lines indicate CTRL, COLD, and WARM runs, respectively.

Chapter 6
Interactions between ocean and successive typhoons in the Kuroshio region

6.1 Introduction

Tropical cyclones (TCs) are extreme mesoscale phenomena characterized by anomalously strong winds and low sea level pressure (SLP), and they often cause disastrous weather events that bring heavy rainfall and windstorms to islands and coastal regions in the low-to-mid latitudes. Abrupt heat and moisture fluxes from the ocean in regions with relatively high sea surface temperatures (SSTs) (e.g., > 26 ℃) can contribute to the development of TCs. The developed TCs decrease SST along their wakes by inducing upwelling of subsurface water, vertical turbulent mixing in the upper ocean, and heat release from the sea surface (e.g., Leipper, 1967; Stramma et al., 1986; Sakaida et al., 1998). Such TC-induced regions of decreased SST are called “cold wakes”. Occasionally, a cold wake affects the intensity of subsequent TCs (e.g., Schade and Emanuel, 1999; Lloyd and Vecchi, 2011; Karnauskas et al., 2021): it generally works to weaken subsequent TCs by reducing heat and moisture supply from the ocean. Thus, feedback from the ocean plays a key role in TC development. Therefore, to improve TC forecasts, it is important to understand the interactive evolution of TCs and the upper ocean, including their heat and freshwater exchanges.

The Kuroshio and Kuroshio Extension (KE) regions of the northwestern North Pacific subtropical gyre are characterized by strong air–sea coupling. In particular, the Kuroshio and KE and their temporal variations significantly influence the atmosphere in winter (e.g., Tanimoto et al., 2011; Nakamura et al., 2012; Sugimoto, 2014; Kuwano-Yoshida and Minobe, 2017) and spring (e.g., Nonaka and Xie, 2003; Miyama et al., 2012; Sasaki et al., 2012). For example, Nakamura et al. (2012) showed that the Kuroshio path state south of Japan controls the tracks of winter extratropical cyclones that pass along the south coast of Japan. In addition, Sugimoto et al. (2020, 2021) have recently reported air–sea coupling in summer in the Kuroshio region. All of these studies have found that coastal warming south of Japan attributable to the Kuroshio large meander causes increases of total precipitable water and air temperature around Japan. In summer, many typhoons pass over the Kuroshio and KE in accordance with the large-scale atmospheric circulation pattern in the western North Pacific. The findings of these studies suggest that it is plausible that feedback from the ocean surface layer to typhoons over the Kuroshio and KE differs from that in other subtropical regions. In fact, significant intensification of typhoons over or near the Kuroshio has been reported (Wada, 2015; Wada et al., 2013; Fujiwara et al., 2020a, 2020b). However, because such typhoon responses to the

Kuroshio are rare, more case studies are needed to advance our knowledge of ocean–typhoon interactions in the Kuroshio and KE region.

Formation of cold wakes behind typhoons has been observed in the western North Pacific (e.g., Zheng et al., 2010; Mrvaljevic et al., 2013; Sun et al., 2015). The question that naturally arises is whether SST in the Kuroshio and KE region decreases following the passage of a typhoon as it does in other regions of the subtropical gyre. Wu et al. (2008) reported that the typhoon-induced SST decrease following typhoon NARI (2001) was smaller in the Kuroshio region than in the surrounding region. In contrast, Wei et al. (2014) suggested on the basis of observations of typhoon MEGI (2014) that SST decrease during the passage of a typhoon can be larger in the Kuroshio region than in the surrounding ocean due to locally enhanced vertical mixing. Thus, greatly differing responses of the Kuroshio and KE to typhoons have been observed, and the reasons for these different responses are not fully understood. Liu and Wei (2015) analyzed observational SST data during 2001–2010 and pointed out that the SST decrease due to the passage of a TC tends to be smaller and recover more rapidly in the Kuroshio region than in other regions. However, how the sustained warmth of the Kuroshio influences subsequent typhoons has not been examined.

Within a period of about 2 weeks from late August to early September 2018, typhoons SOULIK, CIMARON, and JEBI, passed through the northwestern subtropical gyre across the Kuroshio (Figure 6.1). This occurrence of three typhoons within a short time period is suitable for investigating both cold wakes formed behind typhoons and their feedback to subsequent typhoons. In this study, focusing on ocean–typhoon interactions during these successive events, we investigated (1) the SST decrease in the northwestern subtropical gyre, including the Kuroshio region, associated with the passages of SOULIK and CIMARON and (2) the impacts of the resulting SST field on JEBI.

We analyzed the results of atmosphere–ocean coupled model simulations by a coupled model developed by the Meteorological Research Institute (MRI). As a feasibility study, global simulations were conducted to explore the predictability of atmospheric and oceanic phenomena such as typhoons, the Madden-Julian Oscillation, SST variations, tides, and meteo-tsunamis up to about 10 days ahead. Although the coupled model simulations were designed for operational applications, the series of simulations enabled us to investigate various air–sea interactions on weather timescales. In addition, we used a recently developed ultra-high-resolution satellite SST product and atmospheric reanalysis dataset to evaluate the model results. The combination of coupled model simulations with observation-based datasets allowed robust examination of ocean–typhoon interactions in the western

North Pacific.

The remainder of this paper is organized as follows. Section 6.2 outlines the model experiments and observational data used in this study. Section 6.3 examines the SST decrease during the passages of SOULIK and CIMARON, and Section 6.4 examines the influence of the SST fields behind SOULIK and CIMARON on JEBI. Section 6.5 is a summary.

6.2 Model experiment and observational data

6.2.1 Model experiment

We used outputs from a series of atmosphere–ocean coupled model simulations. The atmospheric model used for the simulations was the MRI Atmospheric General Circulation Model (MRI-AGCM) version 4.0. This model is based on a global spectral model (GSM) that was in operational use at the Japan Meteorological Agency (JMA) from May 2017 (GSM1705; Yonehara et al., 2018; JMA, 2019). It adopts a reduced Gaussian grid in the horizontal plane (Miyamoto, 2006) and a hybrid sigma–pressure coordinate system in the vertical plane. The number of vertical layers is 100, with the model top at 0.01 hPa. A dynamical core using a double Fourier series (Yoshimura and Matsumura, 2005; Yoshimura, 2021) can be used in MRI-AGCM4.0 instead of the GSM1705 dynamical core, which uses spherical harmonics. The former enables a more computationally efficient simulation, especially in high-resolution configurations. Although a nonhydrostatic option (Yoshimura 2012; Nakano et al., 2017) for MRI-AGCM4.0 is available, in the current study, the model was used with a hydrostatic dynamical core. The model uses the same physical parameterizations as GSM1705, although other physical parameterization options are also introduced. The oceanic part of the coupled model was the MRI Community Ocean Model (MRI.COM) version 4.7 (Tsujino et al., 2017). This model is one of the standard ocean general circulation models in the international intercomparison project (OMIP2; Tsujino et al., 2020). It consists of primitive equations based on Boussinesq and hydrostatic approximations and a vertically re-scaled height coordinate system in which sea level undulations are reflected throughout the water column (Adcroft and Campin, 2004). The model adopts Murray's (1996) tripolar grid in which two singularity points are set on land, in Siberia and Canada. The number of vertical levels is 60, and the layer thickness increases with depth, from 2 m at the top to 700 m for the lowest layer. The Scup coupler (Yoshimura and Yukimoto, 2008) is used to couple these atmospheric and oceanic models.

For each model, we set two horizontal resolutions: for MRI-AGCM4.0, we set the resolution

to about 10 km (using double Fourier series) or 55 km (using spherical harmonics), and for MRI.COM4.7, we set the resolution to about 10 km or 100 km. Hence, four types of global simulation experiments were performed: Hi (atmospheric)–Hi (oceanic), Hi-Lo, Lo-Hi, and Lo-Lo experiments, where Hi/Lo denotes a relatively high/low horizontal resolution. Note that a horizontal resolution of 10 km for the atmospheric model is still insufficient to fully resolve an inner core structure of TCs (Gentry and Lackmann, 2010): intensity of typhoons is not always well reproduced especially for the case of strong ones. Therefore, we pay close attention to reproducibility of typhoons throughout the analysis. The atmospheric initial conditions were based on JMA 6-hourly global objective analysis data. The oceanic initial conditions were derived from an ocean data assimilation system (Toyoda et al., 2021): for both high- and low-resolution experiments, long-term data assimilative simulations were conducted with assimilated data of in situ temperature and salinity profiles and satellite-derived SST, sea surface salinity, sea surface height (SSH), and sea-ice concentration data and with the 3-hourly JRA55-do (Tsujino et al., 2018) surface boundary conditions. These long-term data assimilative simulations used 10-day assimilation window cycles with 3-dimensional variational method. For realistic predictions on a time scale of a few days with the atmospheric model, further adjustment is needed, in particular, by reflecting observed daily SST variations. Accordingly, additional simulations were conducted, which used 1-day assimilation windows during about 15 days (depending on the number of days in the month) from the above 10-day window outputs, and the results from the last 10 days were provided to the coupled simulations as the oceanic initial conditions. This approach allowed the oceanic initial conditions to represent the daily SST and sea-ice concentration variability similar to the observational data (near-real-time version of MGDSST; Kurihara et al., 2006). The integration period of the coupled model simulations was 11 days.

Predictions with an initial time of 00 UTC on 19 August were analyzed to examine SST changes caused by SOULIK and CIMARON, and predictions with an initial time of 00 UTC on 1 September were used to explore the influences of the SST field remaining behind SOULIK and CIMARON on JEBI. Here, we mainly describe the results of the Hi-Hi experiment, because they provide the best match with the observational data, but we confirmed that the results of the other experiments were qualitatively similar.

6.2.2 Mixed layer heat budget analysis

We quantitatively examined the SST decrease due to typhoon forcing by performing a mixed

layer heat budget analysis. For this purpose, we developed an analytical routine for a mixed layer heat budget analysis in MRI.COM.

If the mixed-layer mean of a variable A is denoted as [A], and, for clarity, only one vertical dimension is considered, then the mixed layer temperature (MLT), defined as the mean temperature in the mixed layer, can be expressed in terms of the mixed layer depth $h(t)$ and sea surface undulation $\eta(t)$ as follows:

$$[T](t) = \frac{1}{h(t)+\eta(t)} \int_{-h(t)}^{\eta(t)} T(z,t)\, dz, \tag{6.1}$$

where $T(z,t)$ is the vertical temperature profile. By taking the time differential of equation (6.1), we obtain its temporal evolution

$$\frac{\partial [T](t)}{\partial t} = \frac{1}{h(t)+\eta(t)} \left(\int_{-h(t)}^{\eta(t)} \frac{\partial T(z,t)}{\partial t} dz + \frac{d\eta(t)}{dt} \big(T_\eta(t) - [T](t) \big) + \frac{dh(t)}{dt} \big(T_h(t) - [T](t) \big) \right), \tag{6.2}$$

by applying the Leibniz integral rule:

$$\frac{d}{dt}\Psi(t) = \int_{x_1(t)}^{x_2(t)} \frac{\partial \varphi(x,t)}{\partial t} dx + \frac{dx_2}{dt}\varphi(x_2,t) - \frac{dx_1}{dt}\varphi(x_1,t), \tag{6.3}$$

where

$$\Psi(t) = \int_{x_1(t)}^{x_2(t)} \varphi(x,t)\, dx. \tag{6.4}$$

Here, $T_\eta(t)$ and $T_h(t)$ are temperature at $z=\eta(t)$ and $z=-h(t)$, respectively. The first term within the parentheses on the right-hand side of equation (6.2) is the temperature tendency in the mixed layer; the second term shows the change of surface elevation; and the third term is an entrainment term.

In MRI.COM, the temporal evolution of temperature in a given 3-dimensional grid is determined by total advection (the sum of horizontal and vertical advection), horizontal and vertical diffusion, and the surface heat flux:

$$\frac{\partial T(t)}{\partial t} = ADV_t(t) + DIF_h(t) + DIF_v(t) + FLUX(t), \tag{6.5}$$

where

$$ADV_t(t) = ADV_h(t) + ADV_v(t). \tag{6.6}$$

Here, ADV_t, ADV_h, and ADV_v are total, horizontal, and vertical advection, respectively; DIF_h and DIF_v are diffusion in the horizontal and vertical directions, respectively; and $FLUX$ is the surface heat flux. By averaging equation (6.5) vertically in the mixed layer, we obtain the following equation

in each horizontal grid:

$$\frac{1}{h(t)+\eta(t)}\int_{h(t)}^{\eta(t)}\frac{\partial T(z,t)}{\partial t}dz = [ADV_t](t) + [DIF_h](t) + [DIF_v](t) + [FLUX](t). \quad (6.7)$$

Then, by combining equations (6.2) and (6.7), we finally obtain the following mixed layer heat budget equation:

$$\frac{\partial [T](t)}{\partial t} = [ADV_t](t) + [DIF_h](t) + [DIF_v](t) + [FLUX](t) + ENT(t), \quad (6.8)$$

where

$$ENT(t) = \frac{1}{h(t)+\eta(t)}\frac{d\eta(t)}{dt}\big(T_\eta(t) - [T](t)\big) + \frac{1}{h(t)+\eta(t)}\frac{dh(t)}{dt}\big(T_h(t) - [T](t)\big). \quad (6.9)$$

Here the first term on the right-hand side of equation (6.9) is usually so small as to be negligible. In our routine, the left-hand side of equation (6.8) and the first four terms on the right-hand side are directly calculated, and the last term on the right-hand side (i.e., the entrainment term) is estimated as the residual. Vertical advection is estimated from the vertical velocity at the mixed layer base $w_h(t)$ (where positive values mean upward velocity),

$$[ADV_v](t) = -\frac{w_h(t)}{h(t)}([T](t) - T_h(t)), \quad (6.10)$$

and the horizontal advection term is estimated by subtracting the vertical advection from the total advection.

In this study, the mixed layer depth is defined as the depth at which potential density increases by 0.125 kg m^{-3} from its value at the sea surface. All terms in equation (6.8) were diagnosed online. As is clear from the above calculation procedure, the term on the left-hand side of equation (6.8) (i.e., MLT tendency term) is equal to the sum of the terms on the right-hand side at any time step in every horizontal grid.

6.2.3 Observational data

To validate the model results, we used the daily MURSST product (Chin et al., 2017), derived from satellite and in situ SST observations on a 1/100º (longitude) × 1/100º (latitude) grid, and the daily SSH product based on satellite altimetry measurements from the Copernicus Marine Environment Monitoring Service (CMEMS; marine.copernicus.eu) on a 1/4º (longitude) × 1/4º (latitude) grid. MURSST has been previously used for research on coastal upwelling and warming (Vazquez-Cuervo et al., 2013; Gentemann et al., 2017; Sugimoto et al., 2020, 2021). Hourly latent heat flux, sensible heat flux, and total precipitation data from ERA5 (Copernicus Climate Change

Service, 2017) with a horizontal resolution of 1/4º (longitude) × 1/4º (latitude) were also used. We obtained typhoon intensities and tracks from the best track data of Regional Specialized Meteorological Centre Tokyo Typhoon Center (RSMC Tokyo Typhoon Center; http://www.jma.go.jp/jma/jma-eng/jma-center/rsmc-hp-pub-eg/besttrack.html). The typhoon intensity, which is represented by the minimum SLP and maximum sustained wind speed (WSP), is estimated by using in situ observations and by the Dvorak (1975) method, which uses satellite observations.

6.3 Oceanic responses to SOULIK and CIMARON

6.3.1 SST decrease caused by SOULIK and CIMARON

In this section, we examine SST changes before and after the passages of SOULIK and CIMARON. The two typhoons moved northwestward in the northwestern subtropical gyre (22–36ºN, 125–140ºE) during 19–23 August 2018 (Figure 6.2). Their tracks are well reproduced in the simulation (Figures 6.1 and 6.2), although the simulated SOULIK passes through the East China Sea a little faster, and the simulated CIMARON travels south of Japan a little slower than they do in the best track data. In contrast, there are discrepancies between the simulated SOULIK and CIMARON intensities and the best track data (Figure 6.3). A remarkable weakening of SOULIK in the East China Sea (30–36ºN) is seen in the best track data, but not in the simulation. This discrepancy may reflect the faster passage of the simulated SOULIK, compared with the observed SOULIK, in the East China Sea: as a result, feedback from the self-induced SST decrease would be larger in reality (Park et al., 2019) than in the simulation. We consider this difference to have little influence on our conclusions, because the East China Sea is not an area of interest in this study. The simulation also does not reproduce well the observed intensity of CIMARON, especially north of 25ºN. The low SST around 25ºN caused by the earlier passage of SOULIK (Figure 6.2, which is well reproduced in the simulation) might have greater influence in the simulation than in reality because of the slow northward migration of the simulated CIMARON.

Figure 6.4 shows simulated and observed SST in the northwestern subtropical gyre on 19 and 24 August 2018 (before and after the passages of SOULIK and CIMARON). Remarkably, SST decreased by up to 3 ℃ along the paths of SOULIK and CIMARON after they passed. Similar to TC-induced sea surface cooling reported previously (e.g., Price, 1981; Lin et al., 2003; D'Asaro et al., 2007), the SST decrease is greatest on the eastern side of the typhoon tracks. According to Price (1981), this rightward bias results from asymmetry of an oceanic response to TCs: TCs generate the upper

ocean current, shear, and then mixing efficiently on their right-hand side where the direction of wind stress changes anti-cyclonically with time in resonance with the near-inertially rotating TC-induced ocean current. Interestingly, where the paths cross the Kuroshio, the SST decrease is quite small (about 1.5 ℃ or less): the Kuroshio is clearly captured as a warm region even after the passages of the two typhoons, and these features are also seen in the satellite SST product (Figure 6.4). The consistency of the SST decrease in both spatial pattern and amplitude between the simulation and observation leads us to suggest that it should be helpful to use the simulations to examine the cause of the smaller SST decrease in the Kuroshio area. Here, the intensity of the two typhoons was substantial as they approached the Kuroshio (Figure 6.3), and they crossed the Kuroshio at almost the same translation speed as the southern regions (Figures 6.1, 6.2, and 6.4). We therefore inferred that the sustained high SST along the Kuroshio is attributable to oceanic structures and processes rather than to changes in intensity and translation speed of the typhoons.

6.3.2 Heat budget analysis during the passage of SOULIK and CIMARON

We examined the cause of the small SST decrease in the Kuroshio region by focusing on the forcing by SOULIK and CIMARON and oceanic conditions in the Kuroshio region. To evaluate their effects on SST quantitatively, we performed a mixed layer heat budget analysis during 19–24 August 2018, as outlined in Section 6.2.2.

During the passages of SOULIK and CIMARON, the vertical diffusion term, which represents the effect of vertical mixing, shows a dominant impact on mixed layer temperature (MLT) (Figures 6.5a and 6.5e). This term explains most of the surface cooling in the western North Pacific subtropical gyre during this period. Although upwelling is detected along the paths of SOULIK and CIMARON, its contribution to the MLT changes, as represented by the vertical advection term, is limited (Figure 6.5c). According to Yablonsky and Ginis (2009), upwelling-induced surface cooling by typhoons with slow translation (< 5 m s^{-1}) cannot be neglected, but here, the translation speeds of simulated SOULIK and CIMARON are greater than 5 m s^{-1} in the analysis region (5.5 m s^{-1} for SOULIK and 8.3 m s^{-1} for CIMARON on average). Therefore, the limited impact of upwelling on MLT in our results is consistent with Yablonsky and Ginis (2009). From 140ºE to 135ºE, however, SOULIK migrates relatively slowly (with a translation speed of 3.9 m s^{-1} on average) and causes a small MLT decrease there through upwelling (Figure 6.5c). The horizontal advection term influences MLT around the maximum cooling region (Figures 6.5a and 6.5b), where a large horizontal MLT

gradient occurred in association with cold wake formation. The broad distribution of positive horizontal advection values is worth noting. This feature may imply that horizontal heat transport plays a role in the surface temperature recovery after the passage of a typhoon. In contrast, the influences of horizontal diffusion, surface heat flux, and entrainment (Figures 6.5d, 6.5f, and 6.5g) are relatively small over the western North Pacific during the averaging period (between 19 and 24 August).

Interestingly, the vertical diffusion term is damped in the Kuroshio region, with the result that the SST decrease is smaller there (Figures 6.5a and 6.5e). We examine this feature from the viewpoint of upper ocean structure. Along the Kuroshio, the mixed layer is deeper, and the vertical gradient of potential temperature around its base is smaller compared with those variables in the surrounding ocean (Figures 6.6 and 6.7). Such temperature structure along the Kuroshio is consistent with an observational result (not shown): we obtained the similar features from optimally interpolated grid dataset of hydrographic observations along 137°E across the Kuroshio (Chapter 4). These oceanic conditions in the Kuroshio region are unfavorable for surface cooling by vertical mixing because the deep mixed layer has large thermal inertia, and the magnitude of mixed layer cooling by vertical mixing increases as the vertical gradient of potential temperature increases around the mixed layer base. Thus, the Kuroshio is less sensitive to typhoon forcing because of its characteristic upper thermal structure. This interpretation is supported by previous studies, in which it is well established that upper oceanic stratification has an impact on oceanic responses to TCs (e.g., Lin et al., 2008, 2009; Yablonsky and Ginis, 2009; Lloyd and Vecchi, 2011; Vincent et al., 2012; Potter and Rudzin, 2021). In particular, according to Vincent et al. (2012), who examined oceanic control on the amplitude of surface cooling with vertical mixing during TC passages using a cooling inhibition index (CI) based on subsurface stratification, the Kuroshio region is more resistant to typhoon forcing (i.e., characterized by a larger CI) than other subtropical regions in the North Pacific. Our results provide quantitative evidence of ocean stratification effects on the oceanic response to TC forcing from a heat budget viewpoint.

To highlight differences in the oceanic response to typhoons in the Kuroshio and other ocean regions, we further examined the temporal evolution of each term in the mixed layer heat budget equation in four regions (Figure 6.8): regions S1 and C1 are in the Kuroshio region near the tracks of SOULIK and CIMARON, respectively, and regions S2 and C2 are located to the south of S1 and C1, respectively (see Figure 6.5a). In regions S1 and S2, MLT decreases during the passage of SOULIK by enhanced vertical mixing (Figures 6.8a and 6.8b). The amplitude of the vertical diffusion term in

S2 is about four times that in S1 during the passage. Surface heat flux during SOULIK's passage exerts a slight cooling effect in both S1 and S2. In contrast, horizontal advection works differently in S1 and S2. In S1, horizontal advection decreases MLT through cool water intrusion from the East China Sea along the Kuroshio (see also Figures 6.4, ,6.5a and 6.5b), whereas in S2, the mixed layer is warmed by horizontal advection just after the maximum total cooling. Upwelling makes a small contribution to the MLT decrease only in S2 because upper stratification is strong (see Figures 6.6 and 6.7). After SOULIK's passage, regions S1 and S2 are warmed by diurnal radiative heating (i.e., the surface flux term). The daily cycle of the horizontal advection term likely reflects heat advection associated with inertial oscillation: the inertial period is $2\pi/f$, that is, 1 cycle day^{-1} at 30ºN. Its amplitude becomes larger during the period of maximum total cooling than during other time periods because of the enhanced horizontal MLT gradient around the cold wake. Similarly, during the passage of CIMARON, region C2 experiences surface cooling through a combination of elevated vertical diffusion, which is about twice as large as in region C1, surface heat flux, and vertical advection, whereas the MLT decrease in region C1 is caused by a combination of vertical diffusion, surface heat flux, and horizontal advection.

Surprisingly, horizontal heat advection by the Kuroshio neither warms the ocean surface layer nor mitigates the SST decrease during the typhoon passages (Figures 6.5b, 6.8a, and 6.8c). In fact, in the case of SOULIK, horizontal advection along the Kuroshio leads to a considerable MLT decrease through the transport of cool water from the East China Sea (S1 region, see Figures 6.5b and 6.8a). However, given the enormous horizontal heat transport by the Kuroshio, it is reasonable to expect that horizontal heat advection in the Kuroshio region has some influence on typhoon-induced SST changes. Liu and Wei (2015) pointed out that SST recovers rapidly in the Kuroshio region after typhoon-induced surface cooling. Therefore, we next investigate the role of Kuroshio heat transport on SST recovery.

To capture the mean change of surface temperature after a typhoon's passage and its cause, we temporally integrate each term of the mixed layer heat budget equation in regions S1, S2, C1, and C2 over the three days just after the passage of SOULIK and CIMARON (22–24 August for regions S1 and S2, and 24–26 August for regions C1 and C2) (Figure 6.9). The result clearly shows that in regions S1 and C1 (i.e., the Kuroshio region), horizontal heat advection is the leading factor leading to warming after the typhoon passage, whereas in regions S2 and C2 (south of the Kuroshio), surface heat flux is the greatest contributor to the warming. These findings suggest that horizontal Kuroshio heat transport plays an important role in the post-typhoon surface temperature recovery in the

Kuroshio region. In the cases of SOULIK and CIMARON 2018, the amplitudes of post-typhoon warming (i.e., MLT recovery) do not differ significantly between the Kuroshio region and the region to its south despite horizontal heat advection is large only in the Kuroshio region. In contrast to the Kuroshio region warmed by horizontal heat transport, in the region to the south of the Kuroshio, the surface temperature recovery is led by a larger response to radiative heating (Figure 6.9) because of the shallower mixed layer (Figure 6.7a) and smaller thermal inertia compared to those in the Kuroshio region.

6.3.3 Dependency of cold wake reproducibility on model resolution

It is noteworthy that the Hi-Lo, Lo-Hi, and Lo-Lo experiments (see section 6.2.1 for details) also reproduced a SST decrease during the passages of SOULIK and CIMARON that is smaller in the Kuroshio region than in other regions (Figure 6.10). Detailed analysis indicated that this smaller decrease is mostly attributable to damped surface cooling with vertical mixing in the Kuroshio region. The consistency of the Kuroshio's response to typhoon forcing among the four simulation types (and observations) supports the reliability of our results.

Comparison of the SST decrease among the four experiment types and the satellite SST product reveals that its amplitude depends mainly on the horizontal resolution of the atmosphere model, whereas its spatial pattern depends mainly on the horizontal resolution of the ocean model. The amplitude of the SST decrease simulated with the low-resolution MRI-AGCM (about 55 km) is only about half of that simulated with the high-resolution MRI-AGCM (about 10 km): the maximum simulated SST decrease is about 1.5 ℃ in the Lo-Lo and Lo-Hi experiments and about 3 ℃ or more in the Hi-Lo and Hi-Hi experiments. The low-resolution MRI.COM (about 100 km) simulates a broadened Kuroshio with a width of about 200–400 km and makes the contrast in the cold wake amplitude between the Kuroshio region and other regions less clear, whereas the high-resolution MRI.COM (about 10 km) clearly shows the Kuroshio as a sharp structure (about 100 km wide) with a unique response to the typhoon forcing. Our four simulation types with different horizontal resolutions suggest that realistic representation of the cold wake after the passage of a typhoon (or TC) requires that both the atmosphere and ocean models have a high horizontal resolution. In the context of the present study, it should again be emphasized that only by using a high-resolution ocean model (10 km or finer) enables the Kuroshio's response to typhoon forcing and feedback to subsequent typhoons to be investigated.

6.4 Influence of SST anomalies behind SOULIK and CIMARON on JEBI

In this section, we discuss the influences of the SST field remaining behind SOULIK and CIMARON on JEBI. JEBI migrated northward in the northwestern subtropical gyre during 1–4 September 2018 (Figure 6.1). In this region, the footprints of SOULIK and CIMARON are detectable in SST until early September. Figure 6.11a shows observed SST changes from 19 August to 1 September. The SST decreases indicate that the influence of SOULIK and CIMARON remains until early September after their passages during 19–23 August. For example, on the track of JEBI, SOULIK-induced negative SST anomalies with a magnitude of –0.9 ℃ at the maximum are located around 28ºN, 133ºE.

The simulation results also represent the footprints of SOULIK and CIMARON (Figure 6.11b). Here, the simulated SST anomalies are calculated by using the two simulations starting from 19 August and 1 September, because each simulation is 11 days long and does not cover the entire period of SOULIK, CIMARON, and JEBI passages. It should be noted that the amplitude of the cold wakes is excessive overall in the simulation: the magnitude of simulated negative SST anomalies is twice as large as that from observations. This is because the SST data (i.e., MGDSST) used for the initialization of the simulation starting from 1 September have a post-typhoon negative bias: As recently reported by Ito (2021), the low-pass filtering adopted for the MGDSST tends to smooth a signal of relatively rapid SST recovery from SST decreases associated with a typhoon passage, leading to broad and relatively uniform cold biases within more than 500 km from the typhoon track after about one or two weeks of the typhoon passage.

In this study, we focus on the different oceanic responses to typhoons in the Kuroshio and other regions. The contrast of SST changes during SOULIK and CIMARON between the Kuroshio region and its surroundings may influence JEBI. Here, we compared the simulated and observed spatial pattern of the SST anomalies. In order to remove an influence of the broad negative SST bias in the simulation described above (Figures 6.11a and 6.11b), we investigate deviations from their area averaged value within a region near SOULIK cold wake (Figures 6.11c and 6.11d). The result indicates that a spatial pattern of the SST anomalies (i.e., contrast of SST changes) in the simulation is consistent with an observational result: negative SST anomalies are relatively large around 28ºN, 133ºE on the track of JEBI, and become smaller or not found along the Kuroshio south of Kyushu. This means that our simulation basically reproduces the influence of SOULIK and CIMARON on the SST field despite

the broad negative SST biases. Therefore, influence of the pre-existing cold wakes on JEBI can be discussed from simulations at least qualitatively. Note that the simulated JEBI track is consistent with observations, although the simulated northward migration of JEBI is a little slower than that in the best track data (Figures 6.1 and 6.12): JEBI passes over the decreased SST region and the Kuroshio causing a cold wake. It is notable that also in the case of JEBI, the amplitude of the SST decrease is smaller along the Kuroshio than in other regions.

6.4.1 Atmospheric response around JEBI to the SST field behind SOULIK and CIMARON

We examined atmospheric responses around JEBI to the SST field caused by SOULIK and CIMARON. We found the turbulent heat flux (THF, the sum of the latent and sensible heat fluxes) around JEBI to be modulated by the SST field (Figures 6.11, 6.12 and 6.13). Here, it is worth noting that the latent heat flux, which is much larger than the sensible heat flux, is responsible for the THF around JEBI (not shown). In the simulation, THF around JEBI is reduced in the region with the decreased SST. Since the remaining SST anomalies caused by SOULIK and CIMARON are comparable to cold wakes generated by JEBI itself during 1–3 September when JEBI arrives at the cold wakes (e.g., within 26–28ºN and 131–134ºE, the former is –0.88 ℃ and the latter is –0.38 ℃ in average respectively, Figures 6.11b and 6.12), it is suggested that the THF around JEBI is influenced by SOULIK and CIMARON to some extent. On the other hand, THF becomes large again over the Kuroshio with relatively high SST, implying the influence of the sustained warmth along the Kuroshio on air-sea heat exchanges around JEBI.

Note that this THF change may include an effect of a change in WSP around JEBI during its northward translation from the region with decreased SST to the Kuroshio region (from 27ºN to 29ºN; also see Section 6.4.2 and Figure 6.16): the maximum WSP of JEBI increases a little from 35 m s^{-1} to 38 m s^{-1}. However, temporal changes of WSP distribution during 00–18UTC on 3 September indicate that the increase of the maximum WSP reflects wind intensification on the eastern side of JEBI where is the outside of the Kuroshio region south of Kyushu (Figure 6.14). It is therefore suggested that the THF changes are attributable to the SST contrast between the Kuroshio and its southern regions.

The above results are supported by observations: reduced THF in the cold wakes and enhanced THF over the Kuroshio can be seen in reanalysis data (Figures 6.11 and 6.13), despite the magnitude smaller than the simulation. Previous studies have demonstrated the role of the latent heat flux in the Kuroshio region in typhoon intensification: for instance, the rapid intensification of typhoon

Man-yi (2013) over the Kuroshio (Wada, 2015) and the development of typhoon Chaba (2010) in the south of the Kuroshio by about 500 km (Fujiwara et al., 2020a, 2020b) have been attributed to the latent heat flux in the Kuroshio region. These findings suggest that the sustained high SST in the Kuroshio region during the passages of SOULIK and CIMARON could potentially influence JEBI through the release of latent heat, although in the case of JEBI, no impact on the typhoon intensity was identified (see Section 6.4.2). In future investigations of other typhoons, it may be possible to detect a significant impact of the sustained warmth of the Kuroshio following the passage of a typhoon on subsequent typhoons.

As with THF, simulated precipitation around JEBI decreases when JEBI is located in the region with decreased SST and increases when JEBI is near the Kuroshio (Figures 6.12 and 6.15). This result suggests that the large heat release in the warm Kuroshio region has a substantial impact on JEBI-related precipitation. The reanalysis data show a distribution of precipitation similar to the simulated precipitation (Figure 6.15). More case studies examining the relationship between sustained warmth of the Kuroshio during typhoon passages and precipitation around subsequent typhoons would contribute to better understandings of ocean–typhoon interactions in the North Pacific subtropical gyre and be very useful for preventing disasters in Japan and other countries in Southeast and East Asia. To assess the effect of the sustained warmth of the Kuroshio on precipitation around typhoons in future work, SST sensitivity experiments should be conducted with high-resolution models. SST around Japan, including in the Kuroshio region, is projected to increase rapidly, at a much higher rate than the global average rate, toward the end of the 21st century (Yamanaka et al., 2021). The evaluation of typhoon and their ambient atmospheric responses to the ocean around Japan will thus become increasingly important.

6.4.2 Influence of the SST field resulted from SOULIK and CIMARON on JEBI intensity

We further examined the influences of the cold wakes remaining behind SOULIK and CIMARON and the sustained warmth of the Kuroshio on JEBI intensity. We expected that an enhanced heat release over the Kuroshio would intensify typhoons, whereas a reduced heat release over the cold wake would weaken typhoons. However, the relationship between SST and JEBI intensity was unclear in the present study. No significant impact of the preexisting region of decreased SST and the warm Kuroshio region on JEBI intensity can be inferred from the best track data (Figure 6.16): JEBI weakened monotonically as it migrated northward of 20ºN. Unfortunately, the observed maximum

intensity of JEBI (SLP 915 hPa and WSP 54 m s^{-1}) is not reproduced in the simulation: in our model, JEBI intensity differs from the best track data throughout the simulation (Figure 6.16). This difference is probably due to the insufficient horizontal resolution of the atmospheric model and the initial condition. According to Gentry and Lackmann (2010), a horizontal resolution of about 4 km is needed to reproduce the inner core structure and significant intensification of some TCs. Influences of the SST field on JEBI intensity should thus be examined in simulations with a much higher horizontal resolution than our resolution. In addition, the negative bias of the initial SST in our simulation would also be a factor causing the poor representation of JEBI intensification. To obtain the robust results, improvement of the oceanic initial condition is also needed.

6.5 Summary

We examined ocean–typhoon interactions in the northwestern North Pacific subtropical gyre using atmosphere–ocean coupled model simulations. We especially focused on whether SST in the Kuroshio region decreases following passages of typhoons as it does in other regions of the western North Pacific or not, which has not been fully understood yet. In late August and early September 2018, three successive typhoons, SOULIK, CIMARON, and JEBI, passed through the northwestern subtropical gyre across the Kuroshio. Both the simulations and observations showed that a large SST decrease up to 3 ℃ occurred along the paths of SOULIK and CIMARON (and also JEBI) except in the Kuroshio region: the Kuroshio remained warm even after the passages of the typhoons. A mixed layer heat budget analysis conducted with the simulations quantitatively revealed that the enhanced vertical mixing in the upper ocean by SOULIK and CIMARON was a dominant factor in the surface cooling, and that upwelling behind the two typhoons had limited impact on SST because of their fast translation speed. In addition, cooling through vertical mixing was not effective in the Kuroshio region because of the deep mixed layer with large thermal inertia and small vertical gradient of potential temperature around the mixed layer base; as a result, the SST decrease was relatively small in the Kuroshio region. Heat transport (horizontal advection) by the Kuroshio does not work to mitigate the surface cooling but plays an important role in the SST recovery after a typhoon's passage. These results are consistent with previous findings. By analyzing specific typhoon cases in detail, we were able to provide real-world examples of the effects of upper ocean stratification on the oceanic response to typhoons, which had been investigated previously by statistical and modeling studies.

We also discussed the influences of the SST field remaining behind SOULIK and

CIMARON on JEBI. We detected no significant impacts on JEBI intensity (minimum SLP and maximum WSP). Our simulation suggested that THF around JEBI was modulated by the SST field. THF was reduced in the decreased SST region and enhanced in the warm Kuroshio region; these changes imply that during the passages of SOULIK and CIMARON, SST remained warm along the Kuroshio and thus retained its potential to influence JEBI. In addition, we demonstrated that the large THF release over the Kuroshio affected JEBI-associated precipitation around Japan. Such feedback from the Kuroshio has not been examined previously. However, our simulation overestimated the negative SST anomalies caused by SOULIK and CIMARON on early September. Therefore, further investigation with improved initialization and for other events is needed to quantify the feedback effects from the ocean over the Kuroshio and the other regions. In the future, Kuroshio–typhoon interactions during the passages of successive typhoons should be explored further.

TCs (typhoons) in the western North Pacific can cause serious disasters such as heavy rainfall and windstorms. To reduce associated damages, many scientists and meteorologists around the world seek to improve the accuracy of TC forecasts. Because TCs derive energy from the ocean, understanding ocean–TC interactions is a key to improving TC forecasts, and future studies should investigate ocean–TC interactions further. The results of the present study suggest that the Kuroshio region, as one of the most important areas of ocean–typhoon interactions in the subtropical North Pacific, is an important region for investigations of atmospheric phenomena associated with typhoons and for improving typhoon forecasting. Our analysis method can be applied in other western boundary current regions such as the Gulf stream, the Agulhas current, the East Australian current, and the Brazil current, and thus can be used to improve TC forecasting worldwide.

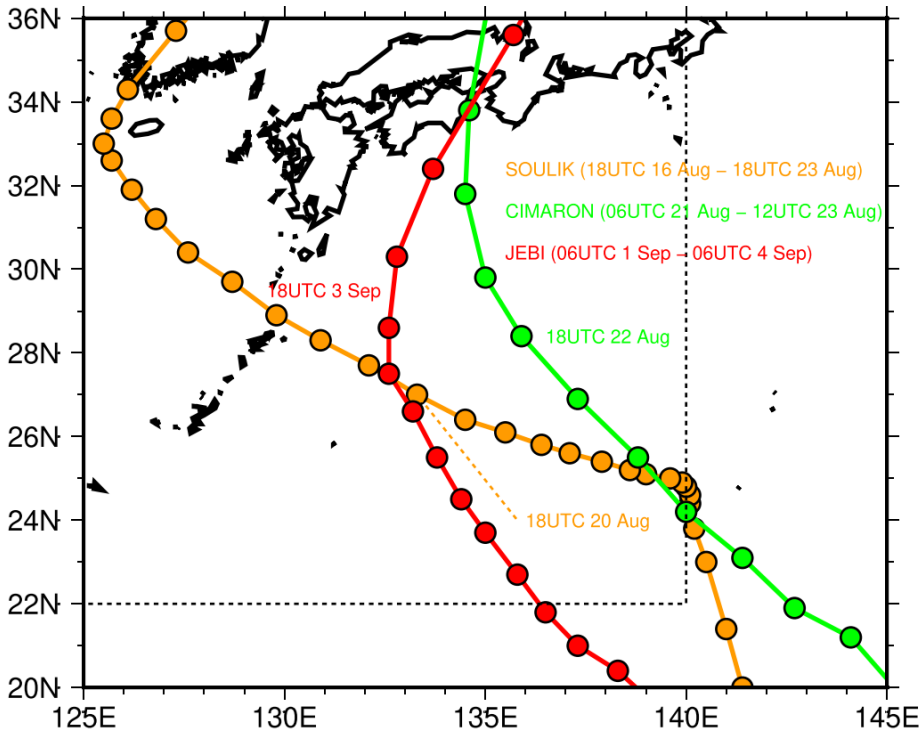

Figure 6.1

Tracks of SOULIK (orange), CIMARON (green), and JEBI (red) at 6-h intervals, based on observations (best track data; see section 6.2.3 for details). The dotted square indicates the analysis region. The time period when each typhoon was located within 20–36ºN, 125–145ºE is also shown.

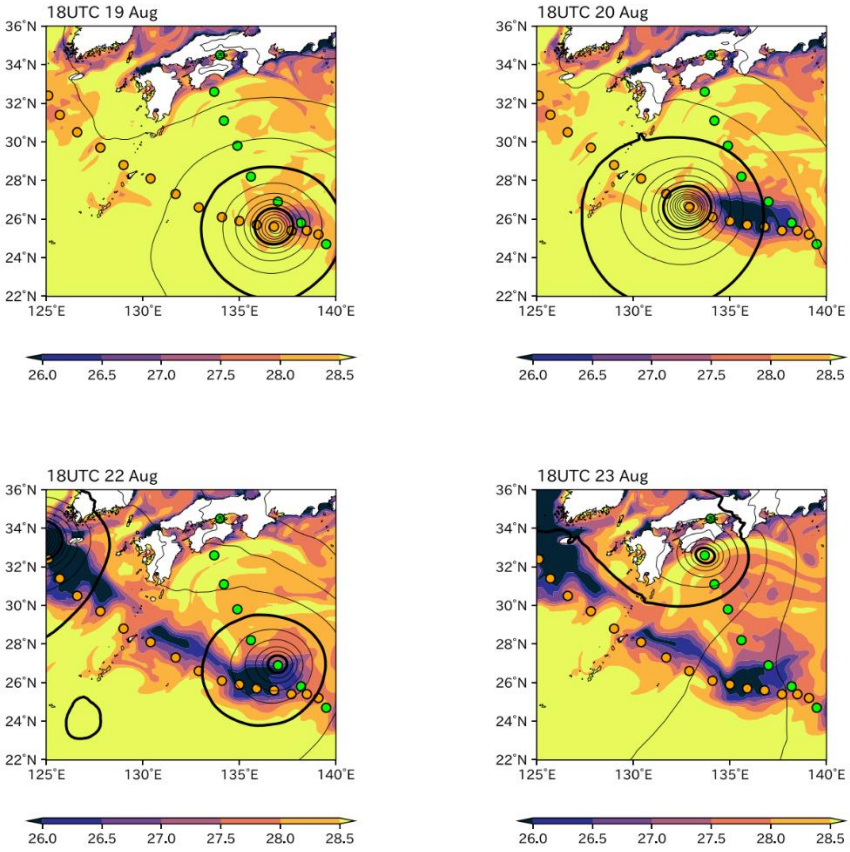

Figure 6.2

Simulated SLP [hPa] (contours, interval 4 hPa) and SST [℃] (color scale) from the Hi-Hi experiment at 18 UTC on 19 August, 18 UTC on 20 August, 18 UTC on 22 August, and 18 UTC on 23 August 2018. The thick contours denote 980 and 1000 hPa. Orange and green dots indicate the simulated tracks of SOULIK and CIMARON, respectively, at 6-h time intervals.

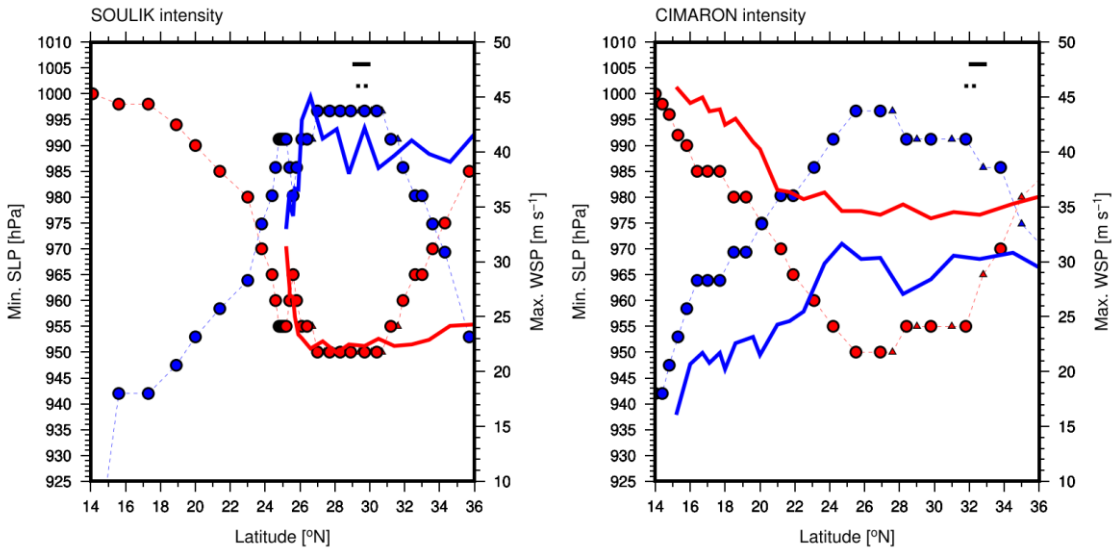

Figure 6.3

Minimum SLP [hPa] (red, left axis) and maximum WSP [m s^{-1}] (blue, right axis) of SOULIK (left) and CIMARON (right) as a function of latitudinal position. Solid lines indicate simulation results (from the Hi-Hi experiment), and dashed lines with dots (6-h intervals) and triangles (3-h intervals) represent best track data. The solid and dashed bars at the top of each panel indicate the Kuroshio region in simulations and observations, respectively.

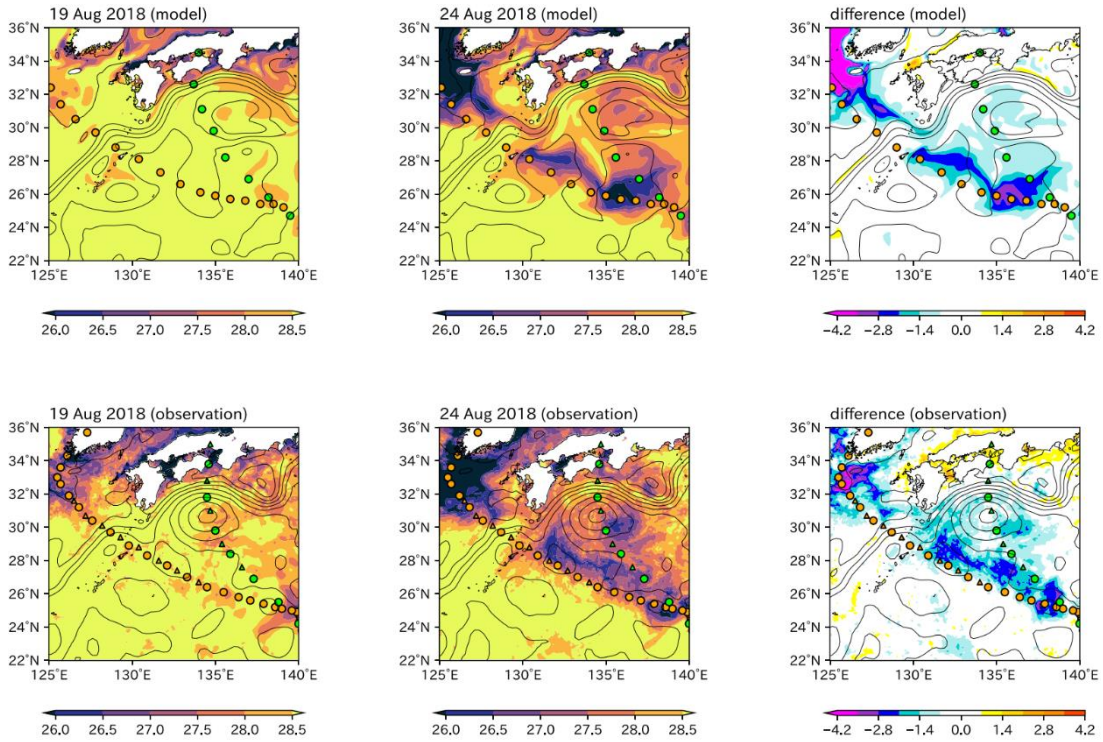

Figure 6.4

Simulated (from the Hi-Hi experiment, top row) and observed (bottom row) SST [℃] on 19 and 24 August of 2018, and their difference [℃] (the latter minus the former). Contours denote simulated and observed SSH [cm] at intervals of 20 cm. Orange and green dots indicate the simulated and observed tracks of SOULIK and CIMARON, respectively, at 6-h intervals. In the observations, the tracks of SOULIK and CIMARON are also shown at 3-h intervals (triangles).

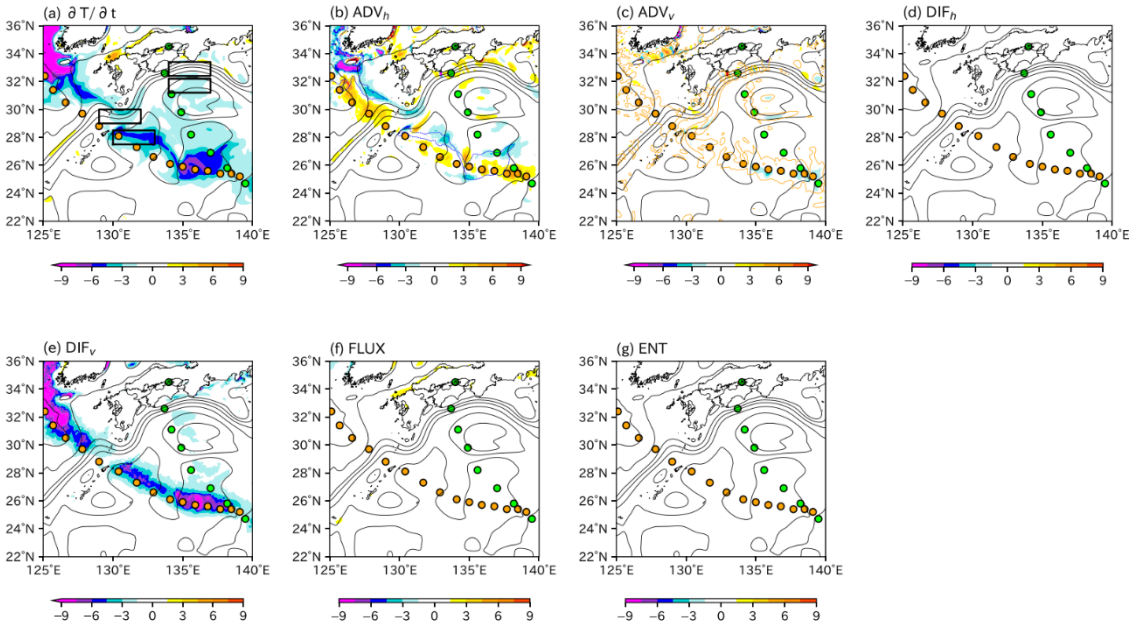

Figure 6.5

Horizontal distribution of each term [10^{-6} °C s^{-1}] in the mixed layer heat budget equation from the Hi-Hi experiment averaged over 19–24 August 2018. Color shading shows the (a) MLT tendency term, (b) horizontal advection term, (c) vertical advection term, (d) horizontal diffusion term, (e) vertical diffusion term, (f) surface heat flux term, and (g) entrainment term. Contours denote SSH [cm] at intervals of 20 cm. The thin blue contour in (b) indicates a MLT tendency term of -4.5×10^{-6} °C s^{-1}, and the thin orange contour in (c) represents an upward velocity of 20×10^{-6} m s^{-1}. Orange and green dots indicate the simulated tracks of SOULIK and CIMARON, respectively, at 6-h intervals. Rectangles in (a) indicate the S1 (Kuroshio, 29–30ºN, 129–132ºE), S2 (southeast of the Kuroshio, 27.5–28.5ºN, 130–133ºE), C1 (Kuroshio, 32.4–33.4ºN, 134–137ºE), and C2 regions (south of the Kuroshio, 31.2–32.2ºN, 134–137ºE) along the tracks of SOULIK (S1 and S2) and CIMARON (C1 and C2).

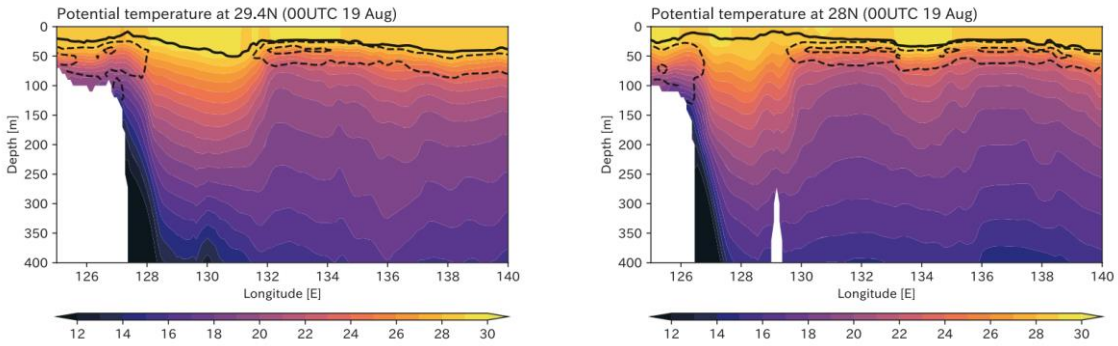

Figure 6.6

Simulated zonal–vertical cross section of potential temperature [°C] along 29.4ºN (left) and 28ºN (right) from the Hi-Hi experiment at 00 UTC on 19 August (initial time). The thick line indicates the mixed layer depth [m]. Dashed contours denote vertical potential temperature gradient [°C m^{-1}] and drawn for values of –0.2 °C m^{-1} and –0.1 °C m^{-1}.

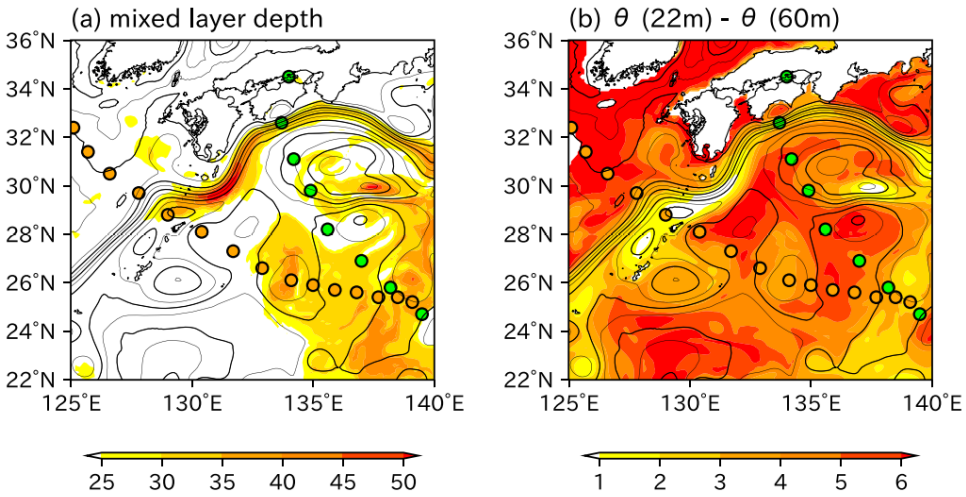

Figure 6.7

Horizontal distribution of the (a) mixed layer depth [m] and (b) vertical potential temperature difference [°C] between depths of 22 m and 60 m from the Hi-Hi experiment at 00 UTC on 19 August (initial time). Contours denotes SSH [cm] at 20-cm (thick lines) and 10-cm intervals (thin lines). Orange and green dots indicate the simulated tracks of SOULIK and CIMARON, respectively, at 6-h intervals.

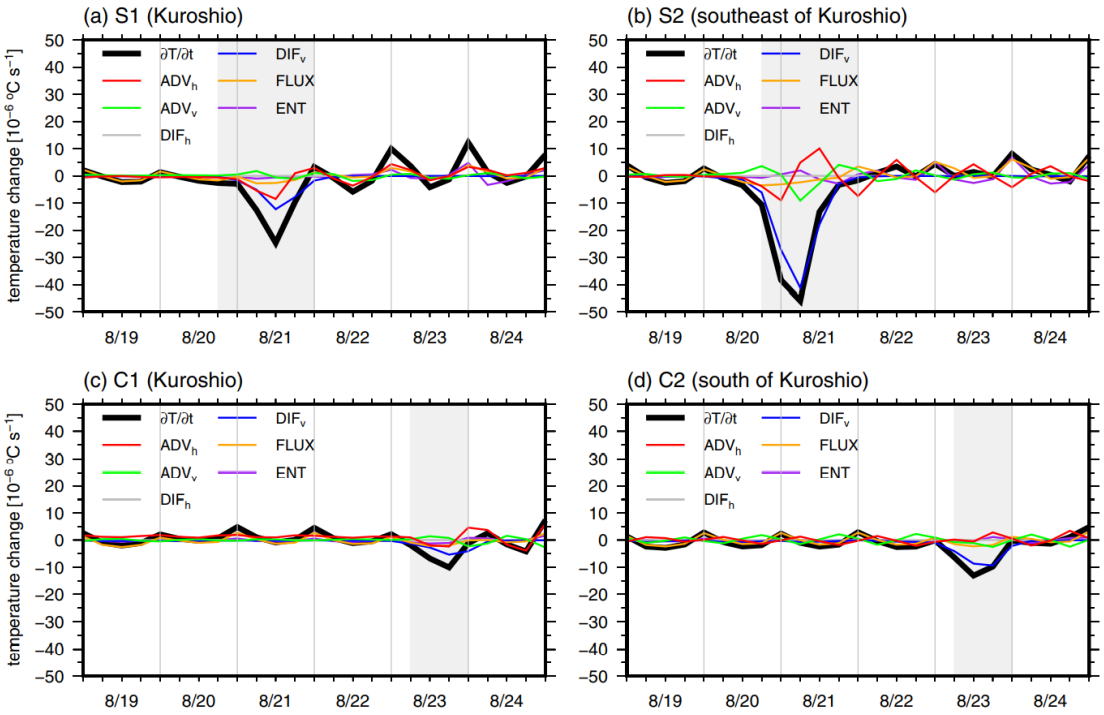

Figure 6.8

Time series of each term [10^{-6} °C s^{-1}] in the mixed layer heat budget equation from the Hi-Hi experiment averaged every 6-h in regions (a) S1 (29–30ºN, 129–132ºE), (b) S2 (27.5–28.5ºN, 130–133ºE), (c) C1 (32.4–33.4ºN, 134–137ºE), and (d) C2 (31.2–32.2ºN, 134–137ºE) (see Figure 6.5a for the locations of the regions). Times are UTC (Japanese standard time – 9-h). Light gray shading in (a) and (b) shows when SOULIK moved from 26.5ºN, 133 ºE to 30.5ºN, 127ºE, and that in (c) and (d) shows when CIMARON moved from 29.5ºN, 134.5ºE to 34.5ºN, 134ºE.

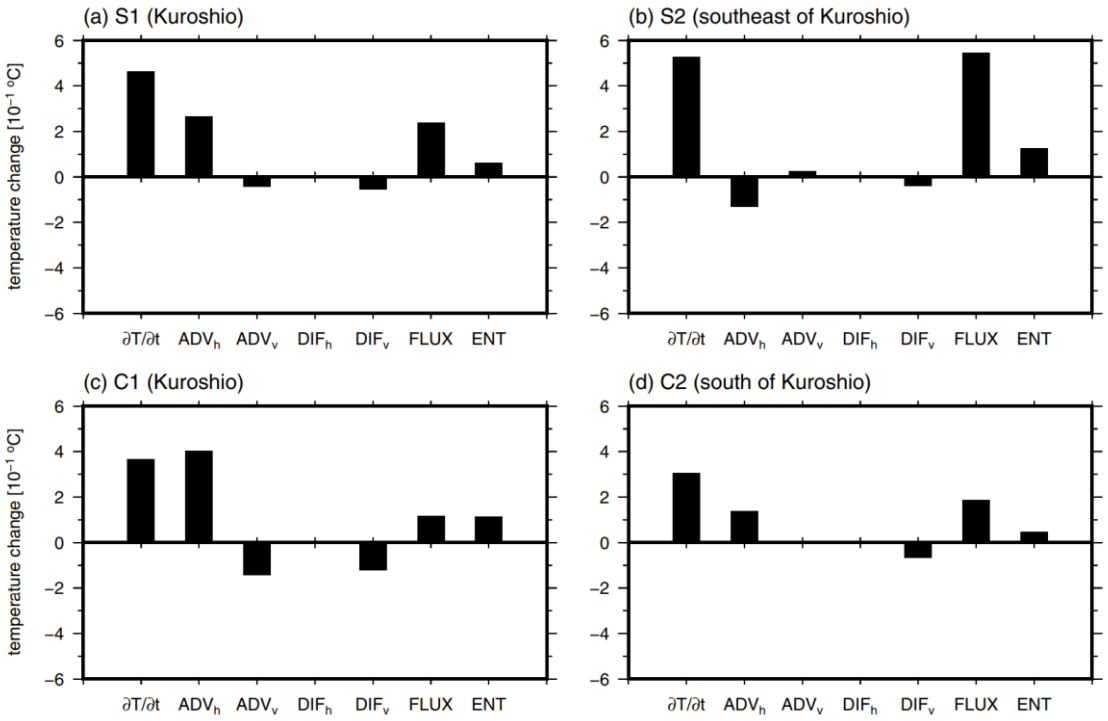

Figure 6.9

Integrated values of each term [10^{-1} °C] in the mixed layer heat budget equation from the Hi-Hi experiment in regions (a) S1 and (b) S2 during 22–24 August, and in regions (c) C1 and (d) C2 during 24–26 August.

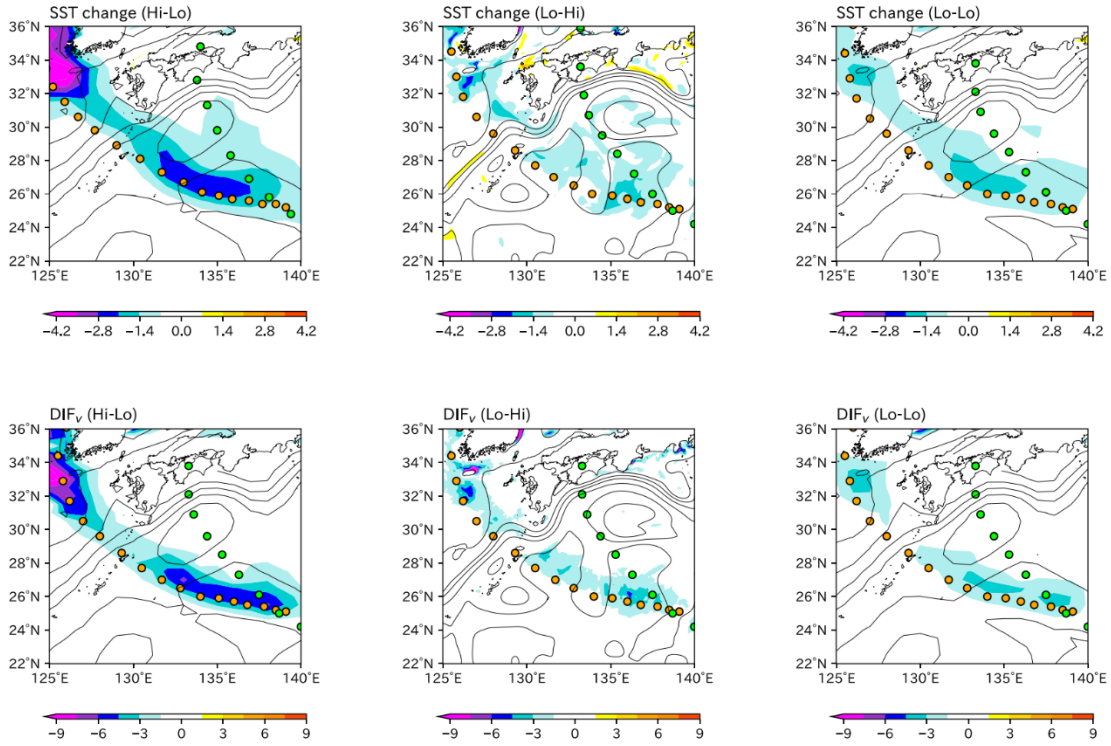

Figure 6.10

(top) Differences in simulated SST [°C] (color scale) between 19 and 24 August in the Hi-Lo, Lo-Hi, and Lo-Lo experiment results. Contours show SSH [cm] at 20-cm intervals. Orange and green dots represent the simulated tracks of SOULIK and CIMARON, respectively, at 6-h intervals. (bottom) Same as panel (e) in Figure 6.5 but for Hi-Lo, Lo-Hi, and Lo-Lo experiment.

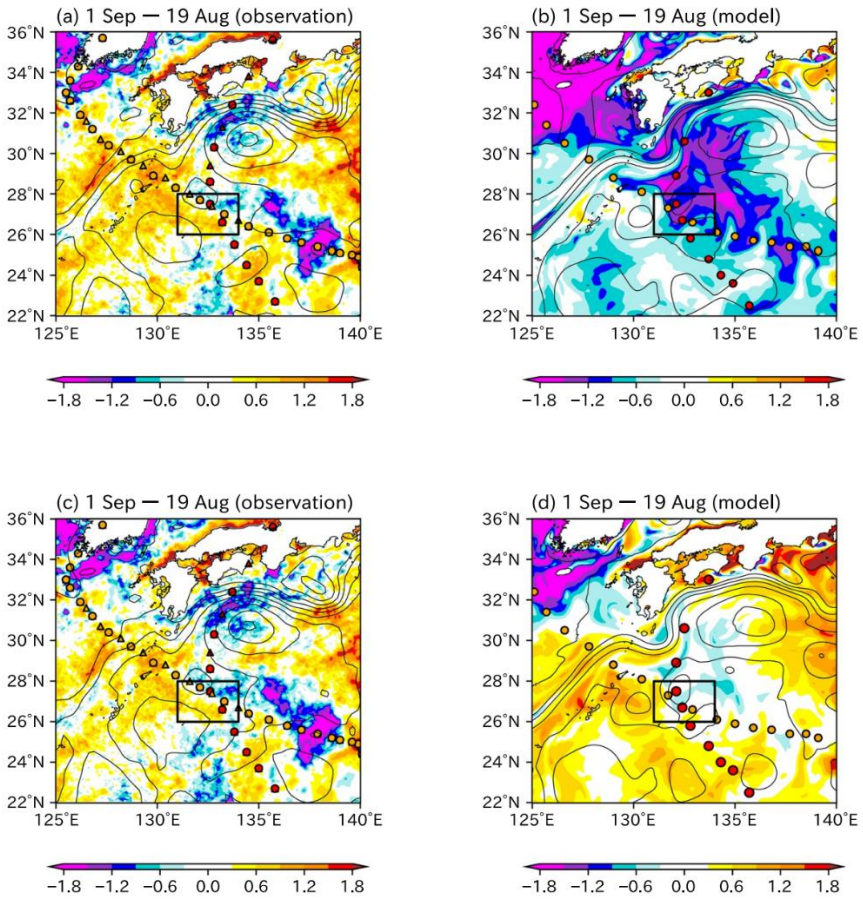

Figure 6.11

(a) Observed SST changes [°C] from 19 August to 1 September. Note that color-scales differ from those in similar figures (Figures 6.4, 6.10, and 6.12). Contours denote observed SSH [cm] at an interval of 20 cm. Red (orange) dots and triangles indicate the track of JEBI (SOULIK) at 6-h and 3-h intervals from best track data. (b) Simulated SST changes [°C] from 19 August to 1 September. Daily-mean SST on 19 August (1 September) given by the simulation initialized at 00 UTC on 19 August (1 September) is used. Red dots indicate the simulated track of JEBI at 6-h intervals. Orange dots indicate SOULIK track from the simulation with an initial time of 00 UTC on 19 August. The black rectangle indicates a region of 26–28ºN, 131–134ºE. (c) and (d) are same as (a) and (b), but for the deviation from the area average value within 26–28ºN, 131–134ºE (black rectangle).

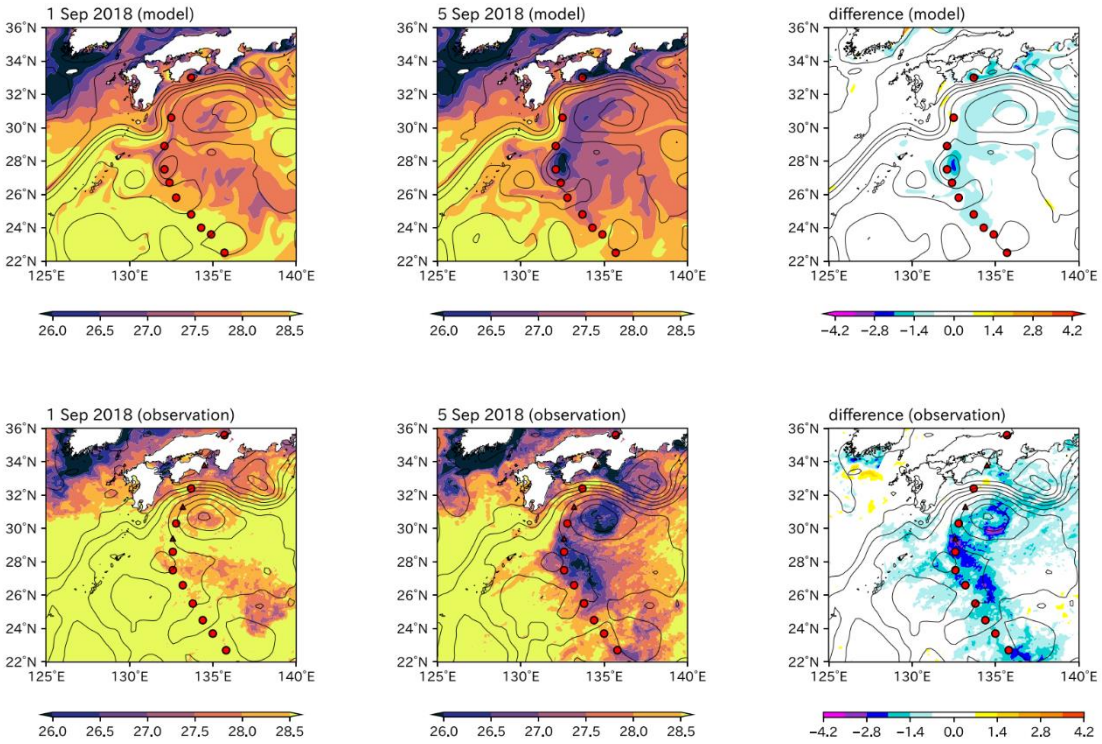

Figure 6.12

Simulated (from the Hi-Hi experiment, top row) and observed (bottom row) SST [°C] on 1 and 5 September 2018 and their difference [°C] (the latter minus the former). Contours denote simulated and observed SSH [cm] at intervals of 20 cm. Red dots and triangles indicate the track of JEBI in the (top row) simulation and (bottom row) best track data. The northernmost red dot (at 33.0ºN, 133.7ºE) in the top panels represents the simulated position of JEBI at 06 UTC on 4 September.

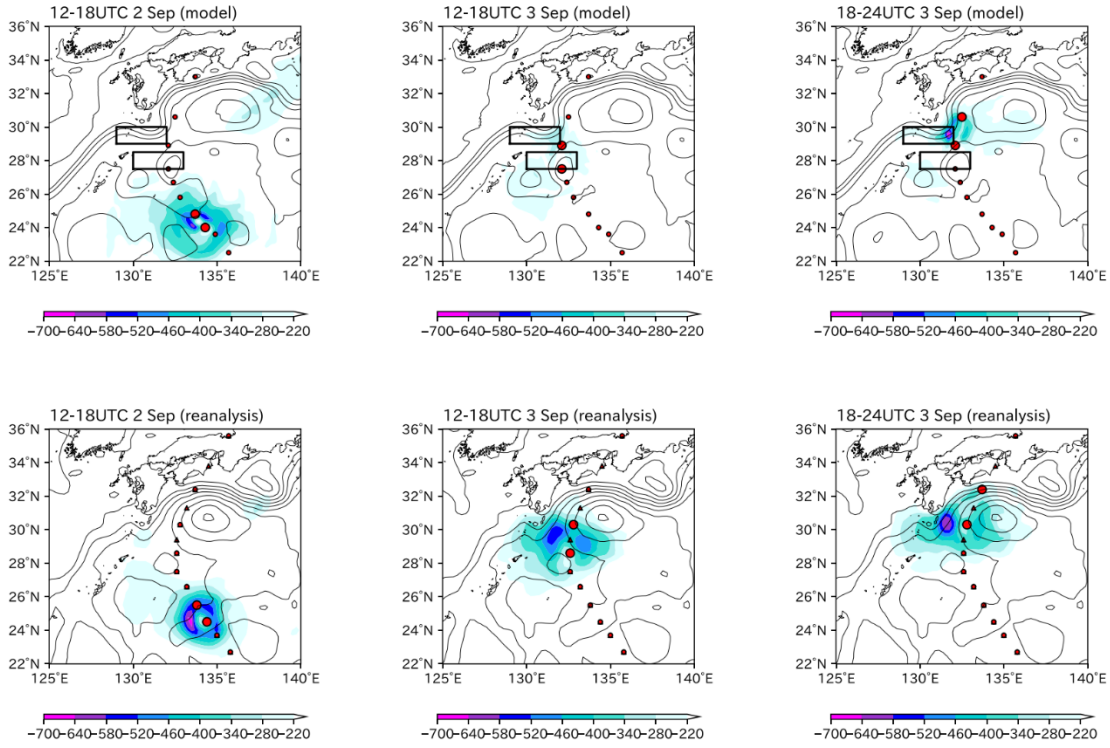

Figure 6.13

Simulated (from the Hi-Hi experiment, top row) and observed (reanalysis data, bottom row) mean THF [W m^{-2}] (color scales) at 12–18 UTC on 2 September, 12–18 UTC on 3 September, and 18–24 UTC on 3 September 2018. Contours denote simulated and observed SSH [cm] at intervals of 20 cm. Negative THF means heat release from the ocean. Red dots indicate the simulated and observed JEBI track at 6-h intervals. The large red dots in each panel represent the position of JEBI at 12–18 UTC on 2 September, 12–18 UTC on 3 September, and 18–24 UTC on 3 September. Rectangles indicate regions S1 and S2. In the observations (bottom row), triangles indicate the track of JEBI at 3-h intervals.

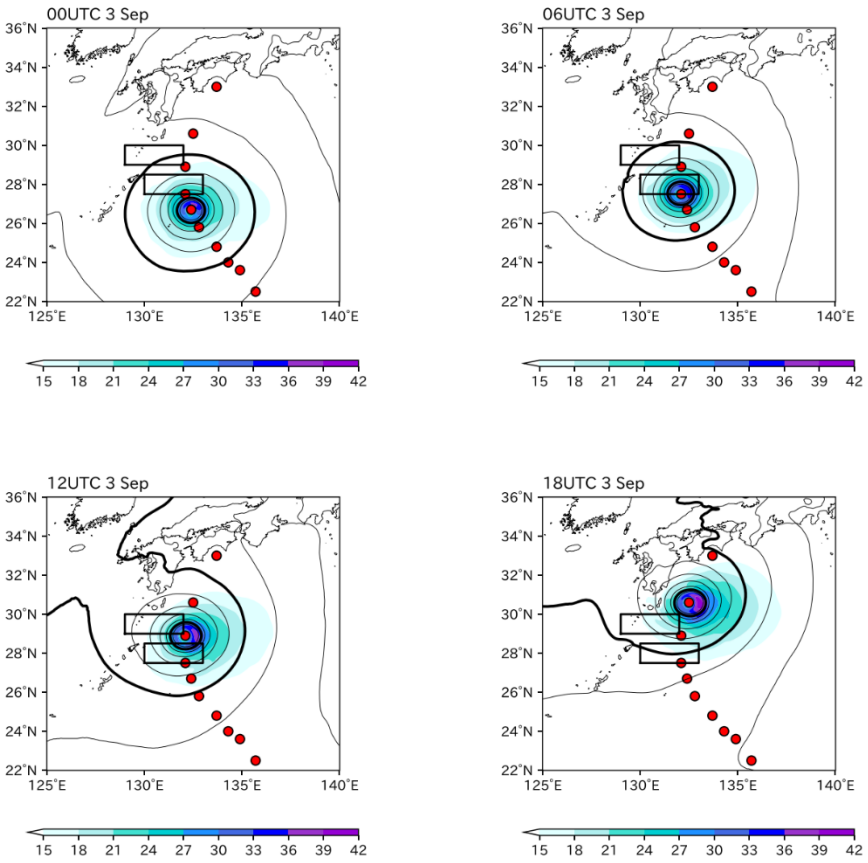

Figure 6.14

Simulated SLP [hPa] (contours, interval 4 hPa) and WSP [m s^{-1}] (color scale) from the Hi-Hi experiment at 00UTC, 06UTC, 12UTC, and 18 UTC on 3 September 2018. The thick contours denote 980 and 1000 hPa. Red dots indicate the simulated JEBI track at 6-h time intervals. Rectangles indicate regions S1 and S2.

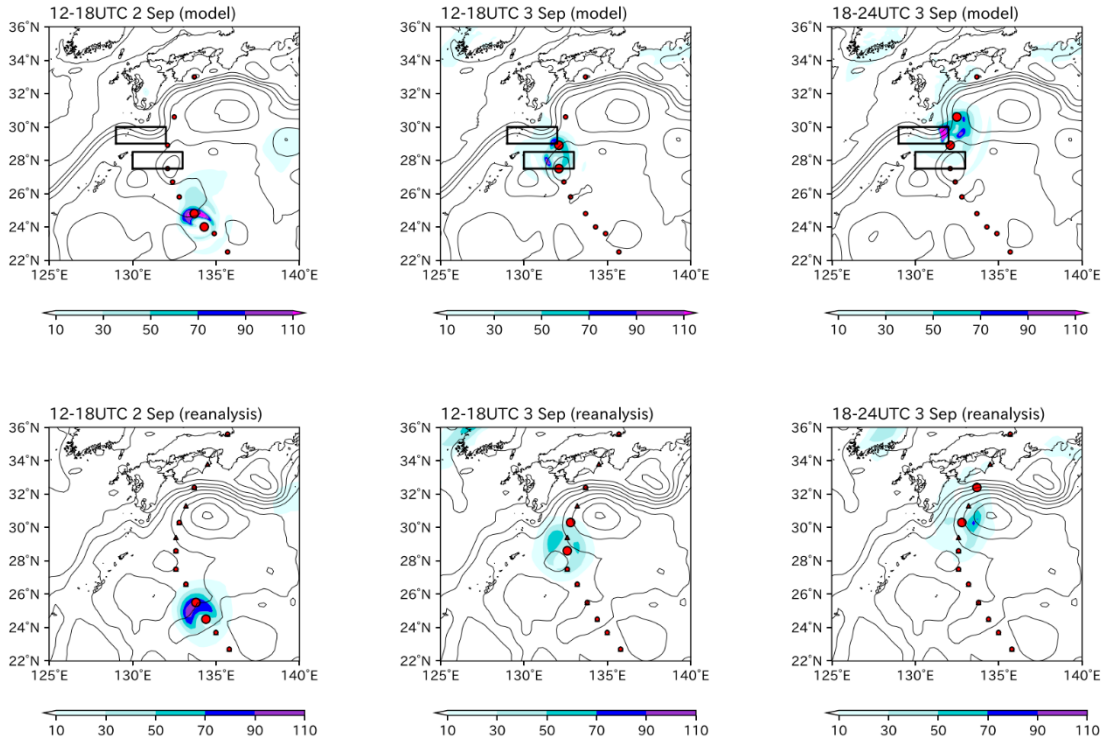

Figure 6.15

Same as Figure 6.13, but for mean precipitation [mm $(6\text{-h})^{-1}$] (color scale).

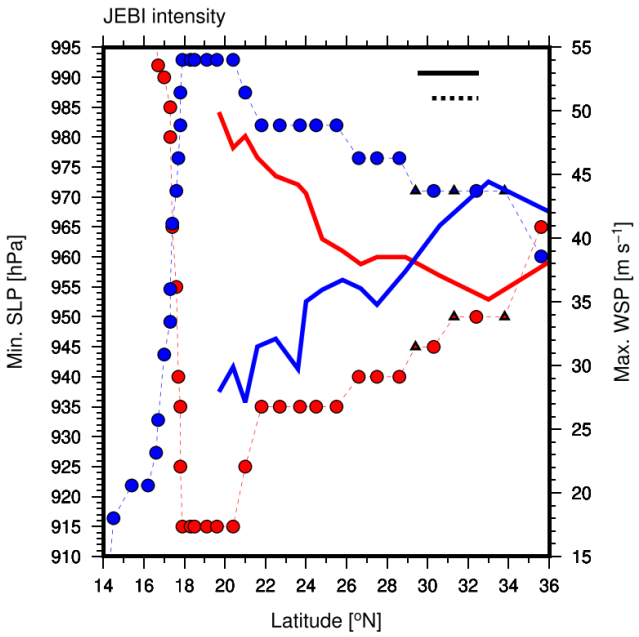

Figure 6.16

Minimum SLP [hPa] (red, left axis) and maximum WSP [m s^{-1}] (blue, right axis) of JEBI as a function of latitudinal position. Thick lines indicate simulation results (Hi-Hi experiment), and dots (6-h intervals) and triangles (3-h intervals) represent best track data. The solid and dashed bars at the top indicate the Kuroshio region in the simulation and observations, respectively.

Chapter 7
General conclusion

In this dissertation, we explored upper ocean variability in the North Pacific subtropical gyre on various timescales, focusing on the Kuroshio and water masses. Based on observational data, we revealed inter-annual or decadal variations of North Pacific central mode water (CMW) formation, temperature/salinity (*T*/*S*) structure in the salinity maximum layer (i.e., North Pacific tropical water; NPTW) and in the main thermocline/halocline, and net Kuroshio transport south of Japan. In addition, by performing numerical experiments with an eddy-resolving ocean general circulation model, we demonstrated atmospheric forcing in a cold season is responsible for variability of net Kuroshio transport and distribution/temperature of North Pacific subtropical mode water (STMW). On a shorter timescale of daily-to-weekly, we clarified sea surface temperature (SST) responses to typhoons in the Kuroshio region from high-resolution atmosphere-ocean coupled model simulations. In this chapter, we summarize the main results and remark issues remained for future works.

In Chapter 2, we investigated an inter-annual variation of formation of the lighter variety of CMW (L-CMW) for 2003−2013 using Argo float profiles. The L-CMW is formed in a zonal band of deep winter mixed layer extended from 140ºE to 160ºW at around 36ºN. Temporal variations of L-CMW formation and their cause are different among the eastern, central, and western part of the formation region. In the eastern formation region, L-CMW formation is increased in winter of 2003–2005 and 2010 in association with an intense atmospheric cooling due to an intensification of the Aleutian Low (AL). In the western formation region, L-CMW formation is enhanced in winter of 2006–2009 and 2011–2013 because of weakly-stratified anti-cyclonic meso-scale eddies detached from the Kuroshio Extension (KE). On the other hand, in the central formation region, L-CMW is formed stably in every winter. It is revealed that L-CMW formed in the eastern formation region effectively subducts into the ocean interior, whereas L-CMW formed in the western formation region is dissipated and/or entrained into mixed layer in the following winter during its eastward advection and hardly detected in the subsurface.

In Chapter 3, we investigated long-term thermohaline changes and variations in the central part of the North Pacific subtropical gyre for 1996−2018 using repeated hydrographic sections along 165ºE by the Japan Meteorological Agency (JMA). We detected significant warming, salinification, and inter-annual thermohaline variations in NPTW and cooling, freshening, and decadal variations in

the main thermocline/halocline. Potential temperature (θ) and salinity (S) in NPTW are originated from mixed layer temperature (MLT) and salinity (MLS) in the winter isopycnal outcrop region. In the NPTW formation region, MLS determines sea surface density and then the meridional position of the isopycnal outcrop region, resulting in θ-S changes in NPTW: high MLS and its-associated southward migration of the outcrop region induce positive θ-S anomalies in NPTW, and *vice versa* for low MLS. The θ and S in the main thermocline/halocline are related respectively to MLT and MLS in the central North Pacific, where both STMW and CMW are formed. In the central North Pacific, MLT controls sea surface density and the meridional position of the isopycnal outcrop region, causing θ-S anomalies in both STMW and CMW: during high MLT years, the outcrop region migrates northward and then cold-fresh STMW and CMW are formed, and *vice versa* during low MLT years. The θ-S anomalies are passed into the main thermocline/halocline through subduction of STMW and CMW. The mechanism generating θ-S anomalies in the main thermocline/halocline (in NPTW) via migration of the isopycnal outcrop regions suggests that surface warming (salinification) in the North Pacific subtropical gyre in the context of global warming causes both cooling and freshening in the main thermocline/halocline (both warming and salinification in NPTW). However, a length of MLT and MLS timeseries used in this study is too short to support this hypothesis. The long-term thermohaline trends in the North Pacific subtropical gyre should be examined with much longer timeseries in future works.

In Chapter 4, we explored temporal variations of net Kuroshio transport south of Japan. Firstly, based on JMA repeated hydrographic sections along 137ºE, we produced a net Kuroshio transport timeseries for 1972−2018 which is about 10 years longer than that used in most of existing studies. We found that the net Kuroshio transport has two dominant timescales and changes its predominant timescale with time: an inter-annual variation is detected before 1990 and after 2000, and a decadal variation is observed only before 2000. The net Kuroshio transport responds to winter wind stress curl (WSC) in the central North Pacific with a 2-year lag through westward propagation of oceanic Rossby waves. The WSC variations in the central North Pacific reflect meridional movements of the AL and intensity fluctuations of the North Pacific subtropical high (NPSH) on an inter-annual timescale and intensity fluctuations of the AL on a decadal timescale. In addition to the inter-annual and decadal variations, a bi-decadal variation of the net Kuroshio transport and its possible link to AL intensity fluctuations are pointed out, but a length of the timeseries is not sufficient to examine this timescale. Influences of the net Kuroshio transport variation on SST fields and the overlying

atmosphere were investigated. During a period of large net Kuroshio transport, SST in the Kuroshio and KE regions tends to increase, resulting in vigorous upward heat release from the sea surface.

In Chapter 5, we evaluated influences of cold and warm season atmospheric forcings on Kuroshio transport and STMW distribution/temperature to determine the responsible season for upper ocean variability in the North Pacific subtropical gyre. We performed three sets of numerical experiments using an ocean general circulation model with a horizontal resolution of about 10 km (i.e., eddy-resolving) by imposing different atmospheric conditions: (1) CTRL run using 3-hourly atmospheric forcing; (2) COLD run using 3-hourly atmospheric forcing in a cold season (October–March) and 3-hourly climatological forcing in a warm season (April–September); and (3) WARM run using 3-hourly forcing in a warm season and 3-hourly climatological forcing in a cold season. The obtained results revealed that all of net Kuroshio transport and STMW distribution/temperature strongly reflect the atmospheric forcing in a cold season.

In Chapter 6, we performed a case study on ocean-typhoon interactions in the western North Pacific based on an event of three typhoons, SOULIK, CIMARON, and JEBI in summer 2018 using atmosphere-ocean coupled model simulations. Although the first two typhoons, SOULIK and CIMARON, decreased SST along their wakes in most of the western North Pacific, the Kuroshio region remained warm even after the typhoon passages. A mixed layer heat budget analysis clearly revealed that cooling effects of the typhoons through vertical mixing were damped in the Kuroshio region because of relatively deep mixed layer (~50 m) compared with that in the other regions and small vertical temperature gradient around the mixed layer base, which are unfavorable conditions for cooling by vertical mixing. We also showed that heat and moisture fluxes around the last typhoon JEBI became small on the cold wakes that were caused by preceded typhoons SOULIK and CIMARON, but remained large over the Kuroshio, implying influences of the high SST sustained in the Kuroshio region during preceded typhoons on subsequent typhoons. These Kuroshio's response and feedback to successive typhoons have not been previously investigated. Further accumulation of case studies focusing on the Kuroshio region will give us a new insight into ocean-typhoon interactions, and would be useful for an improvement of typhoon forecast and disaster prevention in Japan and east Asia.

This dissertation contributes to understandings on upper ocean variability in the western and central parts of the North Pacific subtropical gyre on daily-to-decadal timescales. In the North Pacific subtropical gyre, much longer timescale variations such as Pacific Decadal Oscillation (PDO; Mantua et al., 1997) are pointed out based on longtime observational data at the sea surface. It is an important

future task to understand these low-frequency variations. However, in the ocean interior, investigation of long-term variations has been still limited due to a lack of observational data. Outputs of climate models participated in phase 6 of coupled model intercomparison project (CMIP6) would be one of powerful tools to address this point. In addition, investigation in the eastern North Pacific remains to be done in future works. In the eastern part of the North Pacific subtropical gyre near the center of the NPSH, North Pacific eastern subtropical mode water (ESTMW; Hautala and Roemmich, 1998) formed in deep winter mixed layer is distributed. ESTMW causes spiciness anomalies in the subsurface layers through its subduction (Katsura, 2018) and is advected to the western part of the North Pacific subtropical gyre along the anti-cyclonic circulation (Sasaki et al., 2008), implying its influence on 3-dimensional *T*/*S* structure over the North Pacific subtropical gyre. Sugimoto and Hanawa (2007) pointed out that the seasonal thermocline over ESTMW is weak compared with that of other mode waters in the North Pacific such as STMW and CMW. Since the NPSH dominates the North Pacific in a warm season, ESTMW may be sensitive to atmospheric variations in a warm season unlike STMW in the western North Pacific. Examination of relationships between ESTMW and atmospheric variations in both cold and warm seasons will give us further understandings of upper ocean variability in the North Pacific subtropical gyre.

References

Adcroft, A., and Campin, J. M. (2004) Rescaled height coordinates for accurate representation of free-surface flows in ocean circulation model. *Ocean Modelling*, 7, 269-284. doi:10.1016/j.ocemod.2003.09.003

Akima, H. (1970) A new method of interpolation and smooth curve fitting based on local procedures. *Journal Association of Computation Mathematics*, 17, 589-602. doi:10.1145/321607.321609

Akitomo, K., Ooi, M., and Awaji, T. (1997) Interannual variability of the Kuroshio transport in response to the wind stress field over the North Pacific: Its relation to the path variation south of Japan. *Journal of Geophysical Research*, 101, 14057-14071. doi:10.1029/96JC01000

Andres, M., Wimbush, M., Park, J. H., Chang, K. I., Lim, B. H., Watts, D. R., Ichikawa, H., and Teague, W. J. (2008) Observations of Kuroshio flow variations in the East China Sea. *Journal of Geophysical Research*. 113, C05013. doi:10.1029/2007JC004200

Antonov, J. I. (2002) Steric sea level variations during 1957–1994: Importance of salinity. *Journal of Geophysical Research*, 107, 8013–8020. doi:10.1029/2001JC000964

Aoki, Y., Suga, T., and Hanawa, K. (2002) Subsurface subtropical fronts of the North Pacific as inherent boundaries in the ventilated thermocline. *Journal of Physical Oceanography*, 32, 2299-2311. doi:10.1175/1520-0485(2002)032<2299:SSFOTN>2.0.CO;2

Bingham, M. F. (1992) Formation and spreading of subtropical mode water in the North Pacific. *Journal of Geophysical Research*, 97, 11177-11189. doi:10.1029/92JC01001

Boyer, T. P., Levitus, S., Antonov, I. J., Locarnini, R. A., and Garcia, H. E. (2005) Linear trends in salinity for the World Ocean, 1955–1998. *Geophysical Research Letters*, 32, L01604. doi:10.1029/2004GL021791

Cannon, G. A. (1966) Tropical waters in the western Pacific Ocean, August-September 1957. *Deep Sea Research*, 13, 1139-1148. doi:10.1016/0011-7471(66)90705-4

Chin, T. M., Vazquez-Cuervo, J., and Armstrong, E. M. (2017) A multi-scale high-resolution analysis of global sea surface temperature. *Remote Sensing of Environment*, 200, 154-169. doi:10.1016/j.rse.2017.07.029

Conkright, M. E., Locarnini, R. A., Garcia, H. E., O'Brien, T. D., Boyer, T. P., Stephens, C., and Antonov, J. I. (2002) World Ocean Atlas 2001: Objective analyses, data statistics and figures. National Oceanographic Data Center, CD-ROM Documentation

Copernicus Climate Change Service (C3S) (2017) ERA5: Fifth generation of ECMWF atmospheric

reanalyses of the global climate. Copernicus Climate Change Service Data Store (CDS).

D'Asaro, E. A., Sanford, T. B., Niiler, P. P., and Terrill, E. J. (2007) Cold wake of Hurricane Frances. *Geophysical Research Letters,* 34, L15609. doi:10.1029/2007GL030160

Deser, C., Alexander, M. A., and Timlin, M. S. (1999) Evidence for a wind-driven intensification of the Kuroshio current extension from the 1970s to the 1980s. *Journal of Climate*, 12, 1697-1706. doi:10.1175/1520-0442(1999)012<1697:EFAWDI>2.0.CO;2

Deser, C., Phillip, A. S., and Alexander, M. A. (2010) Twentieth century tropical sea surface temperature trends revised. *Geophysical Research Letters*, 37, L10701. doi:10.1029/2010GL043321

Durack, P. J., and Wijffels, S. E. (2010) Fifty-year trends in global ocean salinities and their relationship to broad-scale warming. *Journal of Climate*, 23, 4342-4362. doi:10.1175/2010JCLI3377.1

Dvorak, V. F. (1975) Tropical cyclone intensity analysis and forecasting from satellite imagery. *Monthly Weather Review*, 103, 420-430. doi:10.1175/1520-0493(1975)103<0420:TCIAAF>2.0.CO;2

Fujiwara, K., Kawamura, R., and Kawano, T. (2020a) Remote thermodynamic impact of the Kuroshio Current on a developing tropical cyclone over the western North Pacific in boreal fall. *Journal of Geophysical Research: Atmosphere*, 125, e2019JD031356. doi:10.1029/2019JD031356

Fujiwara, K., Kawamura, R., and Kawano, T. (2020b) Suppression of tropical cyclone development in response to a remote increase in the latent heat flux over the Kuroshio: a case study for typhoon Chaba in 2010. *SOLA*, 16, 151-156. doi:10.2151/sola.2020-026

Gentemann, C. L., M. R. Fewings, and M. Garcia-Reyes (2017) Satellite sea surface temperature along the west coast of United States during the 2014–2016 northeast Pacific marine heat waves. *Geophysical Research Letters*, 44, 312-319. doi:10.1002/2016GL071039

Gentry, M. S., and Lackmann, G. M. (2010) Sensitivity of simulated tropical cyclone structure and intensity to horizontal resolution. *Monthly Weather Review*, 138, 688-704. doi:10.1175/2009MWR2976.1

Hanawa, K., and Hoshino, I. (1988) Temperature structure and mixed layer in the Kuroshio Extension over the Izu Ridge. *Journal of Marine Research*, 46, 683-700. doi:10.1357/002224088785113397

Hanawa, K., and Kamada, J. (2001) Variability of core layer temperature (CLT) of the North Pacific subtropical mode water. *Geophysical Research Letters*, 28, 2229-2232.

doi:10.1029/2000GL011716

Hanawa, K., and Talley, L. D. (2001) Mode waters. *Ocean Circulation and Climate*. Siedler, G., Church, J., and Gould, W. J. Eds., Academic Press, 373-386.

Hautala, S. L., and Roemmich D. H. (1998) Subtropical mode water in the Northeast Pacific basin. Journal of Geophysical Research, 103, 13055-13066. doi:10.1029/98JC01015

Hosoda, S., Ohira, T., and Nakamura, T. (2008) A monthly mean dataset of global oceanic temperature and salinity derived from Argo float observations. *JAMSTEC Report Research and Development*, 8, 47-59. doi:10.5918/jamstecr.8.47

Hosoda, S., Suga, T., Shikama, N., and Mizuno, K. (2009) Global surface change detected by Argo and its implication for hydrological cycle intensification. *Journal of Oceanography*, 65, 579–586. doi:10.1007/s10872-009-0049-1

Imawaki, S., Uchida, H., Ichikawa, H., Fukasawa, M., Umatani, S., and the ASUKA Group (2001) Satellite altimeter monitoring the Kuroshio transport south of Japan. *Geophysical Research Letters*, 28, 17-20. doi:10.1029/2000GL011796

Ishii, M., Shouji, A., Sugimoto, S., and Matsumoto, T. (2005) Objective analyses of sea-surface temperature and marine meteorological variables for the 20th century using ICOADS and the KOBE collection. *International Journal of Climate*, 25, 865-879. doi:10.1002/joc.1169

Ito, K. (2021) Bias in near-real time global sea surface temperature analysis of Japan Meteorological Agency associated with tropical cyclone passages in western North Pacific. *Journal of Meteorological Society of Japan*, in press. doi:10.2151/jmsj.2022-016

Iwamaru, H., Kobashi, F., and Iwasaka, N. (2010) Temporal variations of the winter mixed layer south of the Kuroshio Extension. *Journal of Oceanography*, 66, 147-153. doi:10.1007/s10872-010-0012-1

Japan Meteorological Agency (JMA) (2019) Outline of the operational numerical weather prediction at the Japan Meteorological Agency. *Appendix to WMO technical progress report on the global data-processing and forecasting system and numerical weather prediction*, 229 pp., http://www.jma.go.jp/jma/jma-eng/jma-center/nwp/outline2019-nwp/index.htm.

Kako, S. I., and Kubota, M. (2007) Variability of mixed layer depth in Kuroshio/Oyashio Extension region: 2005–2006. *Geophysical Research Letters*, 34, L11612. doi:10.1029/2007GL030362

Karnauskas, K. B., Zhang, L., and Emanuel, K. A. (2021) The feedback of cold wakes of tropical cyclones. *Geophysical Research Letters*, 48, e2020GL091676. doi:10.1029/2020GL091676

Katsura, S. (2018) Properties, formation, and disspation of the North Pacific Eastern Subtropical Mode Water and its impact on interannual spiciness anomalies. *Progress in Oceanography*, 162, 120-131. doi:10.1016/j.pocean.2018.02.023

Katsura, S., Oka, E., Qiu, B., and Schneider, N. (2013) Formation and subduction of North Pacific tropical water and their interannual variability. *Journal of Physical Oceanography*, 43, 2400-2415. doi:10.1175/JPO-D-13-031.1

Kawabe, M. (1995) Variations of current path, velocity and volume transport of the Kuroshio in relation with the large meander. *Journal of Physical Oceanography*, 25, 3103-3117. doi:10.1175/1520-0485(1995)025<3103:VOCPVA>2.0.CO;2

Kiss, A. E., Hoggs, A. M., Hannah, N., Dias, F. B., Brassington, G. B., Chamberlain, M. A., Chapman, C., Dobrohotoff, P., Domingues, C. M., Duran, E. R., England, M. H., Fiedler, R., Griffies, S. M., Heerdegen, A., Heil, P., Holmes, R. M., Klocker, A., Marsland, S. J., Morrison, A. K., Munroe, J., Nikurashin, M., Oke, P. R., Pilo, G. S., Richet, O., Savita, A., Spence, P., Steward, K., Ward, M. L., Wu, F., and Zhang, X. (2020) ACCESS-OM2 v1.0: a global ocean-sea ice model at three resolutions. *Geoscientific Model Development*, 13, 401-442. doi:10.5194/gmd-13-401-2020

Kitamura, T., Nakano, T., and Sugimoto, S. (2016) Decadal variations in mixed layer salinity in the Kuroshio Extension recirculate gyre region: influence of precipitation during the warm season. *Journal of Oceanography*, 72, 167-175. doi:10.1007/s10872-015-0317-1

Kobashi, F., Mitsudera, H., and Xie, S. P. (2006) Three subtropical fronts in the North Pacific: observational evidence for mode water-induced subsurface frontogenesis. *Journal of Geophysical Research*, 111, C09033. doi:10.1029/2006JC003479

Kobayashi, S., Ota, Y., Harada, Y., Ebita, A., Moriya, M., Onoda, H., Onogi, K., Kamahori, H., Kobayashi, C., Endo, H., Miyaoka, K., and Takahashi, K. (2015) The JRA-55 Reanalysis: General specifications and basic characteristics. *Journal of Meteorological Society of Japan*, 93, 5-48. doi:10.2151/jmsj.2015-001

Kolodziejczyk, N., and Gaillard, F. (2012) Observation of spiciness interannual variability in the Pacific pycnocline. *Journal of Geophysical Research*, 117, C12018. doi:10.1029/2012JC008365

Kouketsu, S., Tomita, H., Oka, E., Hosoda, S., Kobayashi, T., and Sato, K. (2012) The role of meso-scale eddies in mixed layer deepening and mode water formation in the western North Pacific. *Journal of Oceanography*, 68, 63-77. doi:10.1007/s10872-011-0049-9

Kurihara, Y., Sakurai, T., and Kuragano, T. (2006) Global daily sea surface temperature analysis using data from satellite microwave radiometer, satellite infrared radiometer and in-situ observations (in Japanese). *Weather Bulletin,* 73, s1-s18.

Kuwano-Yoshida, A., and Minobe, S. (2017) Strom-track Response to SST fronts in the Northwestern Pacific region in an AGCM. *Journal of Climate*, 30, 1081-1102. doi:10.1175/JCLI-D-16-0331.1

Ladd, C., and Thompson, L. (2000) Formation mechanisms for North Pacific central and eastern subtropical mode waters. *Journal of Physical Oceanography*, 30, 868-887. doi:10.1175/1520-0485(2000)030<0868:FMFNPC>2.0.CO;2

Large, W. G., and Yeager, S. (2004) Diurnal to decadal global forcing for ocean and sea-ice models: the data sets and flux climatologies. *Technical Note NCAR/TN-460+STR*, CGD Division of the National Center for Atmosphere Research. doi:10.5065/D6KK98Q6

Large, W. G., and Yeager, S. (2009) The global climatology of an interannually varying air-sea flux data set. *Climate Dynamics*, 33, 341-364. doi:10.1007/s00382-008-0441-3

Leipper, D. F. (1967) Observed ocean conditions and hurricane Hilda, 1964. *Journal of the Atmospheric Sciences*, 24, 182-186. doi:10.1175/1520-0469(1967)024<0182:OOCAHH>2.0.CO;2

Levitus, S., Antonov, J., and Boyer, T. (2005) Warming of the world ocean. 1995-2003. *Geophysical Research Letters*, 32, L02604. doi:10.1029/2004GL021592

Levitus, S., Boyer, T. P., Garcia, H. E., Locarnini, R. A., Zweng, M. M., Mishonov, A. V., Reagan, J. R., Antonov, J. I., Baranova, O. K., Biddle, M., Hamilton, M., Johnson, D. R., Paver, C. R., and Seidov, D. (2014) World Ocean Atlas 2013. NOAA National Centers for Environmental information. doi:10.7289/v5f769gt

Lin, I. I., Liu, W. T., Wu, C. C., Chiang, J. C. H., and Sui, C. H. (2003) Satellite observations of modulation of surface winds by typhoon-induced upper ocean cooling. *Geophysical Research Letters*, 30, 1131-1134. doi:10.1029/2002GL015674

Lin, I. I., Pun, I. F., and Wu, C. C. (2009) Upper-ocean thermal structure and the western North Pacific category 5 typhoons. Part II: Dependence on translation speed. *Monthly Weather Review*, 137, 3744-3757. doi:10.1175/2009MWR2713.1

Lin, I. I., Wu, C. C., Pun, I. F., and Ko, D. S. (2008) Upper-ocean thermal structure and the western North Pacific Category 5 typhoons. Part I: Ocean features and the category 5 typhoon's intensification. *Monthly Weather Review*, 136, 3288-3306. doi:10.1175/2008MWR2277.1

Liu, Z. J., Minobe, S., Sasaki, Y. N., and Terada, M. (2016) Dynamical downscaling of future sea level change in the western North Pacific using ROMS. *Journal of Oceanography*, 72, 905-922. doi:10.1007/s10872-016-0390-0

Liu, X., and Wei, J. (2015) Understanding surface and subsurface temperature changes induced by tropical cyclones in the Kuroshio. *Ocean Dynamics*, 65, 1017-1027. doi:10.1007/s10236-015-0851-9

Lloyd, I. D., and Vecchi, G. A. (2011) Observational evidence for oceanic control on Hurricane Intensity. *Journal of Climate*, 24, 1138-1153. doi:10.1175/2010JCLI3763.1

Lukas, R., and Lindstrom, E. (1991) The mixed layer of the western Equatorial Pacific Ocean. *Journal of Geophysical Research*, 96, 3343-3357. doi:10.1029/90JC01951

Mantua, N. J., Hare, S. R., Zhang, Y., Wallace, J. M., and Francis, R. C. (1997) A Pacific interdecadal climate oscillation with impacts on salmon production. *Bulletin of the American Meteorological Society*, 78, 1069-1079. doi:10.1175/1520-0477(1997)078<1069:APICOW>2.0.CO;2

Masuzawa, J. (1969) Subtropical mode water. *Deep Sea Research*, 16, 463-472. doi:10.1016/0011-7471(69)90034-5

Mecking, S., and Warner, M. J. (2001) On the subsurface CFC maxima in the subtropical North Pacific thermocline and their relation to mode waters and oxygen maxima. *Journal of Geophysical Research*, 106, 22179-22198. doi:10.1029/2001JC000846

Minobe, S. (1997) A 50-70 year climatic oscillation over the North Pacific and North America. *Geophysical Research Letters*, 24, 683-686. doi:10.1029/97GL00504

Miyama, T., Nonaka, M., Nakamura, H., and Kuwano-Yoshida, A. (2012) A striking early-summer event of a convective rainband persistent along the warm Kuroshio in the East China sea. *Tellus A: Dynamical meteorology and oceanography*, doi:10.3402/tellusa.v64i0.18962

Miyamoto, K. (2006). Introduction of the reduced Gaussian grid into the operational global NWP model at JMA. *CAS/JSC WGNE Research Activities in Atmospheric and Oceanic Modelling*, 36, 6.9-6.10.

Mogensen, K. S., Magnusson, L., and Bidlot J. R., (2017) Tropical cyclone sensitivity to ocean coupling in the ECMWF. *Journal of Geophysical Research: Oceans*, 122, 4392-4412. doi:10.1002/2017JC012753

Mrvaljevic, R. K., Black, P. G., Centurioni, L. R., Chang, Y. T., D'Asaro, E. A., Jayne, S. R., Lee, C. M., Lien, R. C., Lin, I. I., Morzel, J., Niiler, P. P., Rainveille, L., and Sanford, T. B. (2013)

Observations of the cold wake of Typhoon Fanapi (2010). *Geophysical Research Letters*, 40, 316-321. doi:10.1029/2012GL054282

Murray, R. J. (1996) Explicit generation of orthogonal grids for ocean models. *Journal of Computational Physics*, 126, 251-273. doi:10.1006/jcph.1996.0136

Nakamura, H. (1996) A pycnostad on the bottom of the ventilated portion in the central subtropical North Pacific: its distribution and formation. *Journal of Oceanography*, 52, 171-188. doi:10.1007/BF02235668

Nakamura, H., Nishina, A., and Minobe, S. (2012) Response of storm track to bimodal Kuroshio path sates south of Japan. *Journal of Climate*, 25, 7772-7779. doi:10.1175/JCLI-D-12-00326.1

Nakano, H., Matsumura, Y., Tsujino, H., Urakawa, S., Sakamoto, K., Toyoda, T., and Yamanaka, G. (2021) Effects of eddies on the subduction and movement of water masses reaching 137°E section using Lagrangian particles in an eddy-resolving OGCM. *Journal of Oceanography*, 77, 283-305. doi:10.1007/s10872-020-00573-3

Nakano, M., Wada, A., Sawada, M., Yoshimura, H., Onishi, R., Kawahara, S., Sasaki, W., Nasuno, T., Yamaguchi, M., Iriguchi, T., Sugi, M., and Takeuchi, Y. (2017) Global 7km mesh nonhydrostatic Model Intercomparison Project for improving TYphoon forecast (TYMIP-G7): experimental design and preliminary results. *Geoscientific Model Development*, 10, 1363-1381. doi:10.5194/gmd-10-1363-2017

Nakano, T., Kaneko, I., Soga, T., Tsujino, H., Yasuda, T., Ishizaki, H., and Kamachi, M. (2007) Mid-depth freshening in the North Pacific subtropical gyre observed along the JMA repeat and WOCE hydrographic sections. *Geophysical Research Letters*, 34, L23608. doi:10.1029/2007GL031433

Nakano, T., Kitamura, T., Sugimoto, S., Suga, T., and Kamachi, M. (2015) Long-term variations of North Pacific tropical water along the 137°E repeat hydrographic section. *Journal of Oceanography*, 71, 229-238. doi:10.1007/s10872-015-0279-3

Nan, F., Yu, F., Xue, H., Wang, R., and Si, G. (2015) Ocean salinity changes in the northwest Pacific subtropical gyre: The quasi-decadal oscillation and the freshening trend. *Journal of Geophysical Research*, 120, 2179-2192. doi:10.1002/2014JC010536

Nonaka, M., and Sasaki, H. (2007) Formation mechanism for isopycnal temperature-salinity anomalies propagating from the Eastern South Pacific to the equatorial region. *Journal of Climate*, 20, 1305-1315. doi:10.1175/JCLI4065.1

Nonaka, M., and Xie, S. P. (2003) Covariations of sea surface temperature and wind over the Kuroshio

and its extension: evidence for ocean-to-atmosphere feedback. *Journal of Climate*, 16, 1404-1413. doi:10.1175/1520-0442(2003)16<1404:COSSTA>2.0.CO;2

Ohno, Y., Kobayashi, T., Iwasaka, N., and Suga, T. (2004) The mixed layer depth in the North Pacific as detected by the Argo floats. *Geophysical Research Letters*, 31, L11306. doi:10.1029/2004GL019576

Oka, E. (2009) Seasonal and interannual variation of North Pacific subtropical mode water in 2003–2006. *Journal of Oceanography*, 65, 151-164. doi:10.1007/s10872-009-0015-y

Oka, E., Ishii, M., Nakano, T., Suga, T., Kouketsu, S., Miyamoto, M., Nakano, H., Qiu, B., Sugimoto, S., and Takatani, Y. (2018) Fifty years of the 137ºE repeat hydrographic section in the western North Pacific Ocean. *Journal of Oceanography*, 74, 115-145. doi:10.1007/s10872-017-0461-x

Oka, E., Katsura, S., Inoue, H., Kojima, A., Kitamoto, M., Nakano, T., and Suga, T. (2017) Long-term change and variation of salinity in the western North Pacific subtropical gyre revealed by 50-year long observations along 137°E. *Journal of Oceanography*, 73, 479-490. doi:10.1007/s10872-017-0416-2

Oka, E., Kouketsu, S., Toyama, K., Uehara, K., Kobayashi, T., Hosoda, S., and Suga, T. (2011) Formation and subduction of central mode water base on profiling float data, 2003-2008. *Journal of Physical Oceanography*, 41, 113-129. doi:10.1175/2010JPO4419.1

Oka, E., and Qiu, B. (2012) Progress of North Pacific mode water research in the past decade. *Journal of Oceanography*, 68, 5-20. doi:10.1007/s10872-011-0032-5

Oka, E., Qiu, B., Kouketsu, S., Uehara, K., and Suga, T. (2012) Decadal seesaw of the central and subtropical mode water formation associated with the Kuroshio Extension variability. *Journal of Oceanography*, 68, 355-360. doi:10.1007/s10872-011-0098-0

Oka, E., and Suga, T. (2005) Differential formation and circulation of North Pacific central mode water. *Journal of Physical Oceanography*, 35, 1997-2011. doi:10.1175/JPO2811.1

Oka, E., Suga, T., Sukigara, C., Toyama, K., Shimada, K., Yoshida, J. (2011) “Eddy resolving” observation of the North Pacific subtropical mode water. *Journal of Oceanography*, 41, 666-681. doi:10.1175/2011JPO4501.1

Oka, E., Talley, L. D., and Suga, T. (2007) Temporal variability of winter mixed layer in the mid-to-high-latitude North Pacific. *Journal of Oceanography*, 63, 293-307. doi:10.1007/s10872-007-0029-2

Oka, E., Yamada, K., Sasano, D., Enyo, K., Nakano, T., and Ishii, M. (2019) Remotely forced decadal

physical and biogeochemical variability of North Pacific Subtropical Mode Water over the last 40 years. *Geophysical Research Letters*, 46, 1555-1561. doi:10/1029/2018GL081330

Onogi, K., Tsutsui, J., Koide, H., Sakamoto, M., Kobayashi, S., Hatsushika, H., Matsumoto, T., Yamazaki, N., Kamahori, H., Takahashi, K., Kadokura, S., Wada, K., Kato, K., Oyama, R., Ose, T., Mannoji, N., and Taira, R. (2007) The JRA-25 reanalysis. *Journal of Meteorological Society of Japan*, 85, 369-432. doi:10.2151/jmsj.85.369

Park, J. H., Yeo, D. E., Lee, K. J., Lee, H., Lee, S. W., Noh, S., Kim, S., Shin, J. Y., Choi, Y., and Nam, S. H. (2019) Rapid decay of slowly moving typhoon Soulik (2018) due to interactions with strongly stratified northern East China Sea. *Geophysical Research Letters*, 46, 14595-14603. doi:10.1029/2019GL086274

Potter, H., and Rudzin, J. E. (2021) Upper ocean temperature variability in the Gulf of Mexico with implication for hurricane intensity. *Journal of Physical Oceanography*, 51, 3149-3162. doi:10.1175/JPO-D-21-0057.1

Price, J. F. (1981) Upper ocean response to a hurricane. *Journal of Physical Oceanography*, 11, 153-175. doi:10.1175/1520-0485(1981)011<0153:UORTAH>2.0.CO;2

Qiu, B. (1999) Seasonal eddy field modulation of the North Pacific Subtropical Countercurrent: TOPEX/Poseidon observations and theory. *Journal of Physical Oceanography*, 29, 2471-2486. doi:10.1175/1520-0485(1999)029<2471:SEFMOT>2.0CO;2

Qiu, B. (2000) Interannual variability of the Kuroshio extension system and its impact on the wintertime SST field. *Journal of Physical Oceanography*, 30, 1486-1502. doi:10.1175/1520-0485(2000)030<1486:IVOTKE>2.0.CO;2

Qiu, B., and Chen, S. (2005) Variability of the Kuroshio Extension jet, recirculation gyre, and mesoscale eddies on decadal time scales. *Journal of Physical Oceanography*, 35, 2090-2103. doi:10.1175/JPO2807.1

Qiu, B., and Chen, S. (2006) Decadal variability in the formation of the North Pacific mode water: oceanic and atmospheric control. *Journal of Physical Oceanography*, 36, 1365-1380. doi:10.1175/JPO2918.1

Qiu, B., and Chen, S. (2010) Eddy-mean flow interaction in the decadally modulating Kuroshio Extension system. *Deep Sea Research II*, 57, 1098-1110. doi:10.1016/j.dsr2.2008.11.036

Qiu, B., and Chen, S. (2012) Multidecadal sea level and gyre circulation variability in the northwestern tropical Pacific Ocean. *Journal of Physical Oceanography*, 42, 193-206. doi:10.1175/JPO-D-11-

061.1

Qiu, B., and Chen, S. (2013) Concurrent decadal mesoscale eddy modulations in the western North Pacific subtropical gyre. *Journal of Physical Oceanography*, 43, 344-358. doi:10.1175/JPO-D-12-0133.

Qiu, B., Chen, S., Schneider, N., Oka, E., and Sugimoto, S. (2020) On the reset of the wind-forced decadal Kuroshio Extension variability in late 2017. *Journal of Climate*, 33, 10813-10828. doi:10.1175/JCLI-D-20-0237.1

Qiu, B., and Joyce, T. M. (1992) Interannual variability in the mid- and low-latitude western North Pacific. *Journal of Physical Oceanography*, 22, 1062-1079. doi:10.1175/1520-0485(1992)022<1062:IVITMA>2.0.CO;2

Ren, L., and Riser, S.C. (2010) Observations of decadal time scale salinity change in the subtropical thermocline of the North Pacific Ocean. *Deep Sea Research II*, 57, 1161-1170. doi:10.1016/j.dsr2.2009.12.005

Reynolds, R. W., Smith, T. M., Liu, C., Chelton, D. B., Casey, K. S., and Schlax, M. G. (2007) Daily high-resolution-blended analyses for sea surface temperature. *Journal of Climate*, 20, 5473-5496. doi:10.1175/2007JCLI1824.1

Roemmich, D., and McGowan, J. (1995) Climatic warming and the decline of zooplankton in the California Current. *Science*, 267, 1324-1326. doi:10.1126/science.267.5202.1324

Sakaida, F., Kawamura, H., and Toba, Y. (1998) Sea surface cooling caused by typhoons in the Tohoku Area in August 1989. *Journal of Geophysical Research*, 103, 1053-1065. doi:10.1029/97JC01859

Sakamoto, K., Tsujino, H., Nakano, H., Urakawa, S., Toyoda, T., Hirose, N., Usui, N., and Yamanaka, G. (2019) Development of a 2-km resolution ocean model covering the coastal seas around Japan for operational application, *Ocean Dynamics*, 69, 1181-1202. doi:10.1007/s10236-019-01291-1

Sandwell, D. T., and Agreen, R. W. (1984) Seasonal Variation in Wind Speed and Sea State From Global Satellite Measurements. *Journal of Geophysical Research*, 89, 2041-2051. doi:10.1029/JC089iC02p02041

Sasaki, Y. N., Minobe, S., Asai, T., and Inatsu, M. (2012) Influence of the Kuroshio in the East China Sea on the early summer (Baiu) rain. *Journal of Climate*, 25, 6627-6645. doi:10.1175/JCLI-D-11-00727.1

Sasaki, Y., N., Schneider, N., Maximenko, N., and Lebedev, K. (2010) Observational evidence for propagation of decadal spiciness anomalies in the North Pacific. *Geophysical Research Letters*,

37, L07708. doi:10.1029/2010GL042716

Schade, L. R., and Emanuel, K. A. (1999) The ocean's effect on the intensity of tropical cyclones: results from a coupled atmosphere-ocean model. *Journal of the Atmospheric Sciences*, 56, 642-651. doi:10.1175/1520-0469(1999)056<0642:TOSEOT>2.0.CO;2

Schneider, N. (2004) The response of tropical climate to the equatorial emerge of spiciness anomalies. *Journal of Climate*, 17, 1083-1095. doi:10.1175/1520-0442(2004)017<1083:TROTCT>2.0.CO;2

Shi, F., Luo, Y., and Xu, L. (2018) Volume and transport of eddy-trapped mode water south of the Kuroshio Extension. *Journal of Geophysical Research*, 123, 8749-8761. doi:10.1029/2018JC014176

Shuto, K. (1996) Interannual variations of water temperature and salinity along the 137°E meridian. *Journal of Oceanography*, 52, 575-595. doi:10.1007/BF02238322

Stramma, L., Cornillon, P., and Price, J. F. (1986) Satellite observations of sea surface cooling by hurricanes. *Journal of Geophysical Research*, 91, 5031-5035. doi:10.1029/JC091iC04p05031

Suga, T., Aoki, Y., Saito, H., and Hanawa, K. (2008) Ventilation of the North Pacific subtropical pycnocline and mode water formation. *Progress in Oceanography*, 77, 285-297. doi:10.1016/j.pocean.2006.12.005

Suga, T., and Hanawa, K. (1990) The mixed-layer climatology in the northwestern part of the North Pacific subtropical gyre and the formation area of Subtropical Mode Water. *Journal of Marine Research*, 48, 543-566. doi:10.1357/002224090784984669

Suga, T., and Hanawa, K. (1995a) Interannual variations of North Pacific subtropical mode water in the 137°E section. *Journal of Physical Oceanography*, 25, 1012-1017. doi:10.1175/1520-0485(1995)025<1012:IVONPS>2.0.CO;2

Suga, T., and Hanawa, K. (1995b) The subtropical mode water circulation in the North Pacific. *Journal of Physical Oceanography*, 25, 958-970. doi:10.1175/1520-0485(1995)025,0958:TSMWCI.2.0.CO;2.

Suga, T., Kato, A., and Hanawa, K. (2000) North Pacific tropical water: its climatology and temporal changes associated with the climate regime shift in the 1970s. *Progress in Oceanography*, 47, 223-256. doi:10.1016/S0079-6611(00)00037-9

Suga, T., Motoki, K., Aoki, Y., and Macdonald, A. M. (2004) The North Pacific climatology of winter mixed layer and mode waters. *Journal of Physical Oceanography*, 34, 3-22. doi:10.1175/1520-0485(2004)034<0003:TNPCOW>2.0.CO;2

Suga, T., Takei, Y., and Hanawa, K. (1997) Thermostad distribution in the North Pacific subtropical gyre: The central mode water and the subtropical mode water. *Journal of Physical Oceanography*, 27, 140-152. doi:10.1175/1520-0485(1997)027

Sugimoto, S. (2014) Influence of SST anomalies on winter turbulent heat fluxes in the eastern Kuroshio-Oyashio confluence region. *Journal of Climate*, 27, 9349-9358. doi:10.1175/JCLI-D-14-00195.1

Sugimoto, S., Aono K., Fukui S. (2017a) Local atmospheric response to warm mesoscale ocean eddies in the Kuroshio-Oyashio confluence region. *Scientific Reports*, 7, 11871. doi:10.1038/s41598-017-12206-9

Sugimoto, S., and Hanawa, K. (2007) Further Evidence for Non-Reemergence of Winter SST Anomalies in the North Pacific Eastern Subtropical Mode Water Area. *Journal of Oceanography*, 63, 625-635. doi:10.1007/s10872-007-0055-0

Sugimoto, S., and Hanawa, K. (2009) Decadal and interdecadal variations of the Aleutian Low activity and their relation to upper oceanic variations over the North Pacific. *Journal of Meteorological Society of Japan*, 87, 601-614. doi:10.2151/jmsj.87.601

Sugimoto, S., and Hanawa, K. (2010) Impact of Aleutian low activity on the STMW formation in the Kuroshio recirculation gyre region. *Geophysical Research Letters*, 37, L03606. doi:10.1029/2009GL041795

Sugimoto, S., Hanawa, K., Narikiyo, K., Fujimori, M., and Suga, T. (2010) Temporal variations of the net Kuroshio transport and its relation to atmospheric variations. *Journal of Oceanography*, 66, 611-619. doi:10.1007/s10872-010-0050-8

Sugimoto, S., Hanawa, K., Watanabe, T., Suga, T., and Xie, S. P. (2017b) Enhanced warming of the subtropical mode water in the North Pacific and North Atlantic. *Nature Climate Change*, 7, 656-659. doi:10.1038/nclimate3371

Sugimoto, S., Hanawa, K., Yasuda, T., and Yamanaka, G. (2012) Low-frequency variations of Eastern Subtropical Front in the North Pacific in an eddy-resolving ocean general circulation model: roles of central mode water in the formation and maintenance. Journal of Oceanography, 68, 521-531. doi:10.1007/s10872-012-0116-x

Sugimoto, S., and Kako, S. I. (2016) Decadal variation in winter mixed layer depth south of the Kuroshio Extension and its influence on winter mixed layer temperature. *Journal of Climate*, 29, 1237-1252. doi:19.1175/JCLI-D-15-0206.1

Sugimoto, S., Qiu, B., and Kojima, A. (2020) Marked coastal warming off Tokai attributable to Kuroshio large meander. *Journal of Oceanography*, 76, 141-154. doi:10.1007/s10872-019-00531-8

Sugimoto, S., Qiu, B., and Schneider, N. (2021) Local atmospheric response to the Kuroshio large meander path in summer and its remote influence on the climate of Japan. *Journal of Climate*, 34, 3571-3589. doi:10.1175/JCLI-D-20-0387.1

Sugimoto, S., Takahashi, N., and Hanawa, K. (2013) Marked freshening of North Pacific subtropical mode water in 2009 and 2010: Influence of freshwater supply in the 2008 warm season. *Geophysical Research Letters*, 40, 3102-3105. doi:10.1002/grl.506000

Sun, J., Oey, L. Y., Chang, R., Xu, F., and Huang, S. M. (2015) Ocean response to typhoon Nuri (2008) in western Pacific and South China sea. *Ocean Dynamics*, 65, 735-749. doi:10.1007/s10236-015-0823-0

Suzuki, T., and Ishii, M. (2011) Long-term regional sea level changes due to variations in water mass density during the period 1981-2007. *Geophysical Research Letters*, 38, L21604. doi:10.1029/201GL049326

Takahashi, T., Sutherland, S. C., Wanninkhof, R., Sweeney, C., Feely, R. A., Chipman D. W., Hales, B., Friederich, G., Chavez, F., Sabine, C., Watson, A., Bakker, D. C. E., Schuster, U., Metzl, N., Inoue, H. Y., Ishii, M., Midorikawa, T., Nojiri, Y., Kortzinger, A., Steinhoff, T., Hoppema, M., Olafsson, J., Arnarson, T. S., Tilbrook, B., Johannessen, T., Olsen, A., Bellerby, R., Wong, C. S., Delille, B., Bates, N. R., and Baar, H. J. W. (2009) Climatological mean and decadal change in surface ocean pCO2, and net sea-air CO2 flux over the global oceans. *Deep Sea Research II*, 56, 554-577. doi:10.1016/j.dsr2.2008.12.009

Taneda, T., Suga, T., and Hanawa, K. (2000) Subtropical mode water variation in the northwestern part of the North Pacific subtropical gyre. *Journal of Geophysical Research*, 105, 19891-19598. doi:10.1029/2000JC900073

Tanimoto, Y., Kanenari, T., Tokinaga, H., and Xie, S. P. (2011) Sea level pressure minimum along the Kuroshio and its extension. *Journal of Climate*, 24, 4419-4434. doi:10.1175/2011JCLI4062.1

Toyama, K., Iwasaki, A., and Suga, T. (2015) Interannual variation of annual subduction rate in the North Pacific estimated from a gridded Argo product. *Journal of Physical Oceanography*, 45, 2276-2293 doi:10.1175/JPO-D-14-0223.1

Toyama, K., and Suga, T. (2012) Roles of mode waters in the formation and maintenance of central

water in the North Pacific. *Journal of Oceanography*, 68: 79-92. doi:10.1007/s10872-011-0040-5

Toyoda, T., Nakano, H., Aiki, H., Ogata, T., Fukutomi, Y., Kanno, Y., Urakawa, L. S., Sakamoto, K., Yamanaka, G., and Nagura, M. (2021) Energy flow diagnosis of ENSO from an ocean reanalysis. *Journal of Climate*, 34, 4023-4042. doi:10.1175/JCLI-D-20-0704.1

Trenberth, K. E., and Hurrell, J. W. (1994) Decadal atmosphere-ocean variations in the Pacific. *Climate Dynamics*, 9, 303-319. doi:10.1007/BF00204745

Tsujino, H., Nakano, H., Sakamoto, K., Urakawa, S., Hirabara, M., Ishizaki, H., and Yamanaka, G. (2017) Reference manual for the Meteorological Research Institute Community Ocean Model version 4. *Technical Report of Meteorological Research Institute*, 80.

Tsujino, H., Urakawa, L. S., Griffies, S. M., Danabasoglu, G., Adcroft, A. J., Amaral, A. E., Arsouze, T., Bentsen, M., Bernardello, R., Boning, C., Bozec, A., Chassignet, E. P., Danilov, S., Dussin, R., Exarchou, E., Fogli, P. G., Kemper, F. B., Guo C., Ilicak, M., Iovino, D., Kim, W. M., Koldunov, N., Lapin, V., Li ,Y., Li, P., Lindsay, K., Liu, H., Long, M. C., Komuro, Y., Marsland, S. J., Masina, S., Nummelin, A., Rieck, J. K., Robert, Y. R., Scheinert, M., Sicardi, V., Sidorenko, D., Suzuki, T., Tatebe, H., Wang, Q., Yeager, S. G., and Yu, Z. (2020) Evaluation of global ocean-sea-ice model simulations based on the experimental protocols of the Ocean Model Intercomparison Project phase 2 (OMIP-2). *Geoscientific Model Development*, 13, 3643-3708. doi:10.5194/gmd-13-3643-2020

Tsujino, H., Urakawa, S., Nakano, H., Small, R. J., Kim, W. M., Yeager, S. G., Danabasoglu, G., Suzuki, T., Bamber, J. L., Bentsen, M., Boning, C. W., Bozec, A., Chassignet, E. P., Curchitser, E., Dias, F. B., Durack, P. J., Griffies, S. M., Harada, Y., Ilicak, M., Josey, S. A., Kobayashi, C., Kobayashi, S., Komuro, Y., Large, W. G., Sommer, J. L., Marsland, S. J., Masina, S., Scheinert, M., Tomita, H., Valdivieso, M., and Yamazaki, D. (2018) JRA-55 based surface dataset for driving ocean-sea-ice models (JRA55-do). *Ocean Modelling*, 130, 79-139. doi:10.1016/j.ocemod.2018.07.002

Tsujino, H., and Yasuda, T. (2004) Formation and circulation of mode waters of the North Pacific in a high-resolution GCM. *Journal of Physical Oceanography*, 34, 399-415. doi:10.1175/1520-0485(2004)034<0399:FACOMW>2.0.CO;2

Uehara, H., Suga, T., Hanawa, K., and Shikama, N. (2003) A role of eddies in formation and transport of North Pacific Subtropical Mode Water. *Geophysical Research Letters*, 30, 1705. doi:10.1029/2003GL017542

Urakawa, L. S., Tsujino, H., Nakano, H., Sakamoto, K., Yamanaka, G., and Toyoda, T. (2020) The sensitivity of a depth-coordinate model to diapycnal mixing induced by practical implementations of the isopycnal tracer diffusion scheme. *Ocean Modelling*, 154, 101693. doi:10.1016/j.ocemod.2020.101693

Vazquez-Cuervo, J., Dewitte, B., Chin, T. M., Armstrong, E. M., Purca, S., and Alburqueque, E. (2013) An analysis of SST gradients of the Peruvian Coast: the impact of going to higher resolution. *Remote Sensing of Environment*, 131, 76-84. doi:10.1016/j.rse.2012.12.010

Vincent, E. M., Lengaigne, M., Vialard, J., Madec, G., Jourdain, N. C., and Masson, S. (2012) Assessing the oceanic control on the amplitude of sea surface cooling induced by tropical cyclones. *Journal of Geophysical Research*, 117, C05023. doi:10.1029/2011JC007705

Wada, A. (2015) Unusually rapid intensification of Typhoon Man-yi in 2013 under preexisting warm-water conditions near the Kuroshio front south of Japan. *Journal of Oceanography*, 71, 597-622. doi:10.1007/s10872-015-0273-9

Wada, A., Usui, N., and Kunii, M. (2013) Interactions between Typhoon Choi-wan (2009) and the Kuroshio Extension System. *Advances in Meteorology*, 2013, 859810. doi:10.1155/2013/859810

Wei, J., Liu, X., and Wang, D. X. (2014) Dynamical and thermal response of the Kuroshio to typhoon Megi (2014). *Geophysical Research Letters*, 41, 8495-8502. doi:10.1002/2014GL061706

Weller, R. A., Plueddemann, A. J. (1996) Observations of the vertical structure of the oceanic boundary layer. *Journal of Geophysical Research*, 101, 8789-8806. doi:10.1029/96JC00206

Wu, C. R., Chang, Y. L., Oey, L. Y., Chang, C. W. J., and Hsin, Y. C. (2008) Air-sea interaction between tropical cyclone Nari and Kuroshio. *Geophysical Research Letters*, 3, L12605. doi:10.1029/2008GL033942

Wu, L., Cai, W., Zhang, L., Nakamura, H., Timmermann, A., Joice, T., McPhaden, M. J., Alexander, M., Qiu, B., Visbeck, M., Chang, P., and Giese, B. (2012) Enhanced warming over the global subtropical western boundary currents. *Nature Climate Change*, 2, 161-166. doi:10.1038/nclimate1353

Yablonsky, R. M., and Ginis, I. (2009) Limitation of one-dimensional ocean models for coupling hurricane-ocean model forecasts. *Monthly Weather Review*, 137, 4410-4419. doi:10.1175/2009MWR2863.1

Yamanaka, G., Nakano, H., Sakamoto, K., Toyoda, T., Urakawa, L. S., Nishikawa, S., Wakamatsu, T., Tsujino, H., and Ishikawa, Y. (2021) Projected climate change in the western North Pacific at the

end of the 21st century from ensemble simulations with a high-resolution regional ocean model. *Journal of Oceanography*, 77, 539-560. doi:10.1007/s10872-021-00593-7

Yasuda, T., and Hanawa, K. (1997) Decadal changes in the mode water in the midlatitude North Pacific. *Journal of Physical Oceanography*, 27, 858–870. doi:10.1175/1520-0485(1997)027<0858:DCITMW>2.0.CO;2

Yasuda, T., and Hanawa, K. (1999) Composite analysis of North Pacific subtropical mode water properties with respect to the strength of the wintertime east Asian Monsoon. *Journal of Oceanography*, 55, 531-541. doi:10.1023/A:1007843525069

Yasuda, T., and Kitamura, Y. (2003) Long-term variability of North Pacific subtropical mode water in response to spin-up of the subtropical gyre. *Journal of Oceanography*, 58, 279-290. doi:10.1023/A:1025507725222

Yonehara, H., Sekiguchi, R., Kanehama, T., Saitou, K., Kinami, T., Shimokobe, A., Hotta, D., Nagasawa, R., Sato, H., Ujiie, M., Kadowaki, T., Yabu, S., Yamada, K., Nakagawa, M., and Tokuhiro, T. (2018) Upgrade of JMA's operational global NWP system. *CAS/JSC WGNE Research Activities in Atmospheric and Oceanic Modelling*, 48, 4.17-4.18

Yoshimura, H. (2012) Development of a nonhydrostatic global spectral atmospheric model using double Fourier series. *CAS/JSC WGNE Research Activities in Atmospheric and Ocean Modelling*, 42, 3.05-3.06.

Yoshimura, H. (2021) Improved double Fourier series on a sphere and its application to a semi-implicit semi-Lagrangian shallow water model. *Geoscientific Model Development*, in press. doi: 10.5194/gmd-2021-168.

Yoshimura, H., and Matsumura, T. (2005) A two-time-level vertically conservative semi-Lagrangian semi-implicit double Fourier series AGCM. *CAS/JSC WGNE Research Activities in Atmospheric and Ocean Modelling*, 35, 3.25-3.26.

Yoshimura, H., and Yukimoto, S. (2008) Development of a simple coupler (Scup) for Earth System Modeling. *Papers in Meteorology and Geophysics*, 59, 19-29.

Zhang, Z., Wang, W., and Qiu, B. (2014) Oceanic mass transport by mesoscale eddies. *Science*, 345, 322-324. doi:10.1126/science.124977

Zheng, Z. W., Ho, C. R., Zheng, Q., Kuo, N. J., and Lo, Y. T. (2010) Satellite observation and model simulation of upper ocean biophysical response to Super Typhoon Nari. *Continental Shelf Research*, 30, 1450-1457. doi:10.1016/j.csr.2010.05.005